

2012

Tetrakis(2,6-diisopropylphenyl)diphosphine and related compounds : an electrochemical and EPR spectroscopic study of radical cations

Taghavikish, Mona

Lethbridge, Alta. : University of Lethbridge, Dept. of Chemistry and Biochemistry, c2012

<http://hdl.handle.net/10133/3310>

Downloaded from University of Lethbridge Research Repository, OPUS

**TETRAKIS(2,6-DIISOPROPYLPHENYL)DIPHOSPHINE AND RELATED
COMPOUNDS: AN ELECTROCHEMICAL AND EPR SPECTROSCOPIC
STUDY OF RADICAL CATIONS**

MONA TAGHAVIKISH
B.Sc., Azad University, Science & Research Branch, 2007

A Thesis
Submitted to the School of Graduate Studies
of the University of Lethbridge
in Partial Fulfillment of the
Requirements for the Degree

MASTER OF SCIENCE

Department of Chemistry and Biochemistry
University of Lethbridge
LETHBRIDGE, ALBERTA, CANADA

© Mona Taghavikish, 2012

For my mom Pari Sedigh Ebrahimnia, whose strength,
encouragement and absolute love made my life colorful.

Abstract

In this thesis the synthesis and full characterization of a new bulky diphosphine, tetrakis-(2,6-diisopropylphenyl)diphosphine, are described. This compound displays facile oxidation and a thorough investigation of its redox properties has been studied by combining solution electrochemical techniques such as cyclic voltammetry (CV) and rotating disk electrode (RDE) voltammetry, with spectroscopic methods such as electron paramagnetic resonance (EPR) and Simultaneous Electrochemical Electron Paramagnetic Resonance (SEEPR) spectroscopy over a wide temperature range. Density functional theory (DFT) calculations were carried out to aid in structural characterization of the radical cation that is produced and to provide computed hyperfine splitting (HFS) constants for comparison with experimental results. For comparison to this species with bulky aromatic substituents, similar studies were conducted that have identified the previously unreported radical cation of tetrakis-*tert*-butyldiphosphine with a bulky aliphatic substituent that provides even higher steric pressure than the 2,6-diisopropylphenyl group. DFT calculations are reported, as is full characterization with fluid and frozen-solution EPR spectroscopy.

Further CV and EPR (SEEPR) studies are reported that led to the identification of radical cations of tris(2,6-diisopropylphenyl)arsine and *bis*(2,4,6-triisopropylphenyl)(2,6-diisopropylphenyl)phosphine. DFT calculations are reported, as is full characterization with fluid and frozen-solution EPR spectroscopy.

Acknowledgment

I am heartily thankful to my supervisor, Professor René Boéré, whose encouragement, guidance, patience, knowledge and support enabled me to develop an understanding of this project. I will attribute any success in my Masters degree to his encouragement and effort and without him, this thesis would have not been completed or written. His patience in dealing with all my demands as a graduate student will not be forgotten throughout the rest of my life.

I thank Dr. Peter Dibble for his irreplaceable advice and his help in the absence of my supervisor. I also want to thank him for cheering me up when I most needed it with his witty personality. I would also like to thank Dr. Paul Hayes for taking the time to guide me in our meetings with his smart questions and his kind advice.

To all of the members of the Boéré, Dibble, Hayes and Gerken labs, I thank all of you for the assistance and fun in the lab. I spent almost three years in this lab and you have made coming to the lab such an enjoyable experience and helped me forget that I am not in my homeland anymore. Most importantly, I would like to thank Tracey Roemmele for being a wonderful co-worker (co-supervisor), who with her knowledge and experience helped me understand all the concepts behind the major part of my project. I also appreciate all her efforts when we had to travel to Calgary since we did not have our own instrument, and when she had such a difficult days just for me to get some results. Second, I would like to thank Leila Mokhtabad for being a fun friend and lab mate who filled my lonely days.

Many thanks go to Kris Fischer, who was a tremendous asset in making and repairing much of the glassware that was necessary for my project. Thanks also to Susan Hill for helping me with the administrative paperwork and for her friendship.

Last but not the least; I would like to thank my family, friends and my love. My parents deserve special mention for their inseparable support and sacrifice. My angelic mom and my dad, two lovely old retired chemists, they tried their best to send their children abroad in order to get a better opportunity and education. They who accept being alone for us to be successful. Who can forget such a sacrifice in life? Thank you my loves. Special thanks to second half of my family, Azam and Helen, who try to fill my difficult days with their happiness and sharing their warm family environments with me.

The best brother in the world, he supported me in all the situations both emotionally and financially and gave me the most powerful energy in all these three years by being my home while, I am far from it. Dear Sina, thank you for being such a kind and patient brother.

Thank you to my love for not just handling our long distance relationship for three years but also bearing all my grievances when I know it was not easy at all. Words fail me to express my appreciation toward my love Houman whose dedication, love and persistent confidence in me has taken the load off my shoulder.

Thanks to my best friend Sepideh for being like my older sister and my best friend forever who filled my blue days with her hopeful and happy comments and also Farhad, Bahar, Nader.

Table of Contents

Abstract	iv
Acknowledgment	v
Table of Contents	vii
List of Tables	x
List of Figures	xii
List of Schemes	xv
List of Abbreviations	xvii
Chapter 1 Introduction	1
1.1 Introduction to the chemistry of phosphorus-phosphorus bond.....	1
1.2 Further background on the synthesis of tetraorganodiphosphines	5
1.2.1 Reduction with <i>bis</i> -imidazolidenes	5
1.2.2 Reactions of organolithium and Grignard reagents.....	7
1.2.3 Preparation of phosphines <i>via</i> lithiated phosphide anions	9
1.3 Structural properties of diphosphines.....	12
1.4 Electrochemical and spectroelectrochemical properties of diphosphines	14
1.5 Introduction to triarylphosphines	17
1.5.1 Synthetic methods for triarylphosphines.....	17
1.5.2 Structural characterization of triarylphosphines	20
1.5.3 Electrochemical and spectroelectrochemical studies of triarylphosphines.....	22
1.5.4 Applications of triarylphosphines	26
1.6 Triarylarsines.....	27
1.7 Goal of thesis.....	29
References.....	30
Chapter 2 Methodology	34
2.1 Introduction to electroanalytical techniques	34
2.1.1 Voltammetry.....	35
2.1.2 Cyclic voltammetry	36
2.1.3 Cyclic voltammetry experimental equipment	41
2.1.4 Rotated-disk voltammetry (RDE)	43
2.2 Electron paramagnetic resonance spectroscopy (EPR).....	45
2.3 EPR spectroelectrochemistry	49
2.3.1 Simultaneous electrochemical electron paramagnetic resonance (SEEPR)	50
2.4 Density functional theory	52
2.4.1 Introduction	52
2.4.2 The Hohenberg-Kohn theorem.....	53
2.4.3 Exchange-correlation functional	56
2.4.4 LDA exchange functional	56
2.4.5 LDA correlation functional	57
2.4.6 Beyond the LDA - gradient corrected functional.....	57
2.4.7 Hybrid functional	58
2.5 Application of DFT calculation.....	58
References.....	59

Chapter 3 Tetraorganodiphosphines	62
3.1 Introduction	62
3.1.1 Synthesis of Dipp ₄ P ₂	62
3.1.2 Attempts to prepare Tripp ₄ P ₂	68
3.1.3 Synthesis of ^t Bu ₄ P ₂	76
3.2 Crystal structure of Dipp ₄ P ₂	77
3.3 Discussion of NMR studies of tetraorganodiphosphines	81
3.3.1 Results of cyclic voltammetry of Dipp ₄ P ₂	90
3.3.2 Results of cyclic voltammetry of ^t Bu ₄ P ₂	95
3.3.3 Determination of the diffusion coefficients for Dipp ₄ P ₂	96
3.4 EPR spectroscopy.....	99
3.4.1 SEPR investigation of Dipp ₄ P ₂	99
3.4.2 EPR investigation of Dipp ₄ P ₂ with chemical oxidation.....	102
3.4.3 SEPR investigation of ^t Bu ₄ P ₂	106
3.5 In electronic structure of R ₄ P ₂ from DFT calculations	107
3.5.1 Introduction	107
3.5.2 Geometry studies.....	108
3.5.3 Electronic structure include bonding.....	113
3.5.4 HFS constants from experiment and calculation.....	116
3.6 Discussion	117
References.....	121
Chapter 4 Electrochemical investigations of Dipp ₃ As and Tripp ₂ DippP radical cations	124
4.1 Introduction	124
4.2 Cyclic voltammetry results.....	124
4.2.1 Results of cyclic voltammetry of Tripp ₂ DippP	124
4.2.2 Determination of the diffusion coefficients for Tripp ₂ DippP and Dipp ₃ As.....	126
4.2.3 Results of cyclic voltammetry of Dipp ₃ As.....	127
4.2.4 EPR investigation of Dipp ₃ As by chemical oxidation	130
4.2.5 SEPR investigations of Tripp ₂ DippP.....	134
4.2.6 EPR investigation of Tripp ₂ DippP by chemical oxidation	136
4.3 Application of anisotropic hyperfine coupling constant	136
4.4 DFT calculation results in Dipp ₃ As	138
References.....	140
Chapter 5 Future work	141
5.1 Introduction	141
5.1.1 Future work on tetraorganodiphosphines.....	142
5.1.2 Future work on triarylphosphines	144
5.2 Conclusion.....	145
References.....	146
Chapter 6 Experimental	147
6.1 General procedures for synthesis	147
6.1.1 Preparation of tetrakis(2,6-diisopropylphenyl)diphosphine:.....	148
6.1.2 Preparation of 1,1-Di- <i>tert</i> -butyl-2,2-diphenyldiphosphine:	149
6.2 Crystal structure of Dipp ₄ P ₂	150

6.3	Electrochemistry experimental.....	150
6.3.1	Cyclic voltammetry procedure	151
6.3.2	Rotating disk electrode (RDE) voltammetry procedure.....	151
6.3.3	Variable temperature SEEPER investigations.....	152
6.3.4	EPR experiment by chemical oxidation	155
6.3.5	Calculation details	156
	References.....	156
	Appendix.....	159

List of Tables

Table 1.1. Structures involving P–P bond	2
Table 1.2. Some compounds prepared using <i>bis</i> -imidazolidenes	6
Table 1.3. Summary of P–P bond lengths and sums of the –E– (E:P, As) bond angle of some representative tetraorganodiphosphines	13
Table 1.4. Summary of cyclic voltammetry studies of tetraaryldiphosphines.....	15
Table 1.5. EPR data for radical cations of tetraaryldiphosphines. ^{34, 37, 41}	15
Table 1.6. Summary of triarylphosphines characterization studies	20
Table 1.7. Comparative redox potentials for triaryl phosphines ^a	24
Table 1.8. EPR data for Ar ₃ P ⁺⁺ radicals	25
Table 1.9. Average C–Pn bond lengths, C–Pn–C bond angles, and oxidation potentials of the crowded triarylphosphine, -arsine, -stibine.....	28
Table 3.1. Crystal data and structure refinement for Dipp ₂ PClO	66
Table 3.2. Crystal data and structure refinement for Dipp ₄ P ₂	78
Table 3.3. Selected intera-atomic distances (Å) and angles (°) and space group for some R ₄ P ₂ compounds from X-ray diffraction data.....	81
Table 3.4. Summary of chemical shift correlation of isopropyl CH ₃ and CH signals from the COSY proton NMR of Dipp ₄ P ₂	83
Table 3.5. Distances of CH ₃ from perpendicular and coplanar Dipp rings	85
Table 3.6. ¹ H and ¹³ C NMR data for Dipp ₄ P ₂ at room temperature	86
Table 3.7. ¹ H and ¹³ C NMR data for aromatic atoms in Dipp ₄ P ₂	89
Table 3.8. Summary of cyclic voltammetry data obtained for both oxidation process of Dipp ₄ P ₂ at GC electrode and T = 22 °C. ^a	92
Table 3.9. Summary of cyclic voltammetry data obtained for first oxidation process of Dipp ₄ P ₂ at GC electrode and T = 22 °C. ^a	93
Table 3.10. Summary of cyclic voltammetry data obtained for oxidation process of ^t Bu ₄ P ₂ at GC electrode and T = 22 °C. ^a	95
Table 3.11. Limiting current values for solution of Dipp ₄ P ₂ in CH ₂ Cl ₂ in different concentrations	97
Table 3.12. Diffusion coefficient values for solution of Dipp ₄ P ₂ in CH ₂ Cl ₂	98
Table 3.13. Experimental EPR data for the Dipp ₄ P ₂ ⁺⁺	101
Table 3.14. Effect of temperature changes on experimental EPR data for Dipp ₄ P ₂ ⁺⁺	105
Table 3.15. Effect of modulation amplitude on experimental EPR data for the Dipp ₄ P ₂ ⁺⁺	105
Table 3.16. P–P bond distances (Å) and selected angles (°) for Dipp ₄ P ₂ from X-ray diffraction and computation.....	109
Table 3.17. P–P bond distances (Å) and selected angles (°) for ^t Bu ₄ P ₂ from X-ray diffraction and computation.....	110
Table 3.18. Computed geometry results for [H ₄ P ₂] ⁿ⁺ and [Dipp ₄ P ₂] ⁿ⁺ (n = 0, 1, 2)	110
Table 3.19. Calculations optimized at the B3LYP/6-311G++(3df,2p) level.....	112
Table 3.20. Summary of the DFT and EPR data for Dipp ₄ P ₂ and ^t Bu ₄ P ₂	117

Table 4.1. Summary of cyclic voltammetry data obtained for both oxidation process of Tripp ₂ DippP at a GC electrode and T = 22 °C.	125
Table 4.2. Summary of cyclic voltammetry data obtained for both oxidation process of Dipp ₃ As at GC electrode and T = 22 °C.	127
Table 4.3. Summary of redox potential of triarylarsine and phosphine obtained in CH ₂ Cl ₂ solution expressed vs $E^{\circ}_{Fc+/0}$	130
Table 4.4. Experimental EPR data for the Dipp ₃ As ^{+/0} in solution	132
Table 4.5. Experimental EPR data for the Tripp ₂ DippP ^{+/0}	135
Table 4.6. EPR and structural parameters of radical cations of studied compounds	138
Table 4.7. Summary of DFT calculation for Dipp ₃ As ⁺	139

List of Figures

Figure 1.1. Possible conformations of diphosphines	5
Figure 1.2. EPR spectrum oftetrakis(2,4,6-triethylphenyl)diphosphine radical cation.electro generated in butyronitrile 0.1 M in tetra-n-butylammonium hexafluorophosphate at 296 K(Reprinted with permission from (<i>J. Am. Chem. Soc.</i> , 1985, 107 (24), pp 7191–7193).....	16
Figure 1.3. Illustration of the endo and exo substituents in triarylphosphines	22
Figure 1.4. Cyclic voltammetry of Dipp ₃ P (0.20 mM) in CH ₂ Cl ₂ solution containing 0.4 M	23
Figure 1.5. EPR spectra of radical cation of tris(2,4,6-triisopropylphenyl)phosphine at (a) 20° and (b) –196° obtained by oxidation with silver(I) perchlorate in dichloromethane. (Reprinted with permission from <i>Current Organic Chemistry</i> , 2007, 11, 17-31).	26
Figure 2.1. Cyclic voltammogram obtained for a reversible one-electron reduction process at 25 °C using the IUPAC sign convention	38
Figure 2.2. Standard cell design employed for CV studies showing the electrical connectors to the working, auxiliary and reference electrodes.	42
Figure 2.3. Rotated-disk electrode setup.....	44
Figure 2.4. (a) Energy levels of an unpaired electron placed in a magnetic field. (b) Energy levels of an unpaired electron in a magnetic field interacting with a spin –1/2 nucleus	47
Figure 2.5. Small-amplitude field modulation detects the signal as a dispersion signal. It is relation to the absorption curve is that of a first-derivative	49
Figure 2.6. Low-temperature EPR flat cell developed by Boéré and Roemmele.	51
Figure 3.1. Thermal ellipsoids plot (30% probability distribution) of Dipp ₂ P(O)Cl as found in the crystal lattice.	65
Figure 3.2. A thermal ellipsoids plot (30% probability distribution) of Dipp ₄ P ₂ as found in the crystal lattice.....	77
Figure 3.3. (a) A “space filling” diagram and (b) a “ball and stick” representation of Dipp ₄ P ₂	78
Figure 3.5. (a) Illustration of orthogonal aryl groups in Dipp ₄ P ₂ with pink colour(b) illustration of coplanar aryl groups in Dipp ₄ P ₂ with yellow colour	79
Figure 3.4. The arrangement-packing diagram of molecule in the unit cell.....	79
Figure 3.6. Proton NMR spectra of Dipp ₄ P ₂ in C ₆ D ₆ at RT	82
Figure 3.7. COSY NMR spectra of Dipp ₄ P ₂ in C ₆ D ₆	83
Figure 3.8. Centroid calculations for Dipp ₄ P ₂ (pink centroid for coplanar planes and blue centroid for perpendicular planes) for distances to the nearest methyl group C atom.....	84
Figure 3.9. HOMO and C ₂₂ CH interaction with phosphorus.....	88
Figure 3.10. Newman Projections down the P–P bond of SS and RR C ₂ symmetric antiperiplanar rotamers of Dipp ₄ P ₂	90
Figure 3.11. Cyclic voltammetry of Dipp ₄ P ₂ (5 mM) in CH ₂ Cl ₂ solution containing 0.4 M [ⁿ Bu ₄ N][PF ₆] under an atmosphere of dry Ar at v = 0.2 Vs ⁻¹ on a GC electrode at 20 °C.	91

Figure 3.12. Cyclic voltammetry of Dipp ₄ P ₂ (5 mM) in CH ₂ Cl ₂ solution containing 0.4 M [ⁿ Bu ₄ N][PF ₆] under an atmosphere of dry Ar at $v = 0.2 \text{ Vs}^{-1}$ on a GC electrode at 20 °C: (a) through the first oxidation process (pink line); (b) through the first and second oxidation processes (black line)	93
Figure 3.13. Plots of the I_p vs. $v^{1/2}$ obtained for the first Dipp ₄ P ₂ oxidation process in CH ₂ Cl ₂ at GC working electrodes.	94
Figure 3.14. Cyclic voltammetry of ^t Bu ₄ P ₂ (5 mM) in CH ₂ Cl ₂ solution containing 0.4 M [ⁿ Bu ₄ N][PF ₆] under an atmosphere of dry Ar at $v = 0.2 \text{ Vs}^{-1}$ on a GC electrode at 20 °C.....	96
Figure 3.15. Plots of the Levich current vs the square root of the rotational velocity of 5.59 mM solution of Dipp ₄ P ₂ in CH ₂ Cl ₂ (0.1 M [ⁿ Bu ₄ N][PF ₆]).....	97
Figure 3.16. RDE curves at a GC electrode when [Dipp ₄ P ₂] ⁺⁺ is generated from 5.5 mM Dipp ₄ P ₂ in CH ₂ Cl ₂ (0.1 M [ⁿ Bu ₄ N][PF ₆]) at different rotation speeds..	98
Figure 3.17. (a) Experimental EPR spectrum obtained after electrolyses of a 5 mM solution of [Dipp ₄ P ₂] ⁺⁺ at a gold mesh electrode at room temperature in CH ₂ Cl ₂ (0.4 M [ⁿ Bu ₄ N][PF ₆]) and modulation frequency 100 kHz, modulation amplitude = 0.5 mT, and (b) first derivative and (c) third derivative simulations obtained using Bruker Simfonia and the parameters listed in Table 3.13.	100
Figure 3.18. First order and second order splitting of a 1:2:1 triplet arising from two equivalent nuclei each with $I=1/2$	101
Figure 3.19. Summary of EPR powder pattern explanation; the observed spectrum is close to that at the RHS.	103
Figure 3.20. (a) Experimental and (b) simulated solid state EPR spectra of Dipp ₄ P ₂ ⁺⁺	104
Figure 3.21. SEPR spectra collected at 273 K in CH ₂ Cl ₂ /0.4 M ⁿ Bu ₄ NPF ₆ on ^t Bu ₄ P ₂ with electrolysis at a potential of 1.4 V. (a) Experimental rapid sweep over the full signal range; (b) simulation of this experimental spectrum (1:1 Lorentzian and Gaussian lineshape components; LW = 0.53 mT; $2 \times A(^{31}\text{P}) = 10.81 \text{ mT}$; $4 \times A(^{13}\text{C})=2.5 \text{ mT}$). (c) Experimental high field branch collected under slow passage conditions. (d) Simulation of (c) with the same parameters used in (b).	107
Figure 3.22. (a) Dipp ₄ P ₂ ²⁺ geometry calculated at B3LYP/6-31G(d) and (b) H ₄ P ₂ ²⁺ geometry calculated at B3LYP/6-311 G ++(3df,2p) level of theory.....	111
Figure 3.23. Lewis structure of diphosphine for neutral, cation and dication	113
Figure 3.24. Molecular orbital energy diagram of H ₄ P ₂ , H ₄ P ₂ ⁺ and H ₄ P ₂ ²⁺ calculated at the B3LYP/6-311G++(3df,2p) level constrained to C _{2h} symmetry	114
Figure 3.25. MO topologies for HOMO and HOMO-1 in neutral Dipp ₄ P ₂	115
Figure 3.26. MO topology of HOMO, LUMO and HOMO-4 in Dipp ₄ P ₂ ²⁺	116
Figure 3.27. SOMO of Dipp ₄ P ₂ radical cation down to the z-axis.....	117
Figure 4.1. Cyclic voltammetry of Tripp ₂ DippP (5 mM) in CH ₂ Cl ₂ solution containing 0.4 M [ⁿ Bu ₄ N][PF ₆] under an atmosphere of dry Ar at $v = 0.2 \text{ Vs}^{-1}$ on a GC electrode at 20 °C: (a) through the first oxidation process (pink line); (b) through the first and second oxidation processes (black line)	126
Figure 4.2. Cyclic voltammetry of Dipp ₃ As (5 mM) in CH ₂ Cl ₂ solution containing 0.4 M [ⁿ Bu ₄ N][PF ₆] under an atmosphere of dry Ar at $v = 0.2 \text{ Vs}^{-1}$ on a GC electrode at 20 °C.....	128

Figure 4.3. (a) Experimental fluid solution EPR spectrum of Dipp_3As obtained after chemical oxidation. (b) Best simulated spectrum (third-order perturbation theory and line-widths corrected for tumbling). (c) Simulation as in (b) without tumbling correction..... 133

Figure 4.4. (a) Experimental frozen solution EPR spectrum of Dipp_3As obtained by chemical oxidation and (b) simulation obtained using second order perturbation theory..... 133

Figure 4.5. (a) Experimental fluid solution EPR spectrum of $\text{Tripp}_2\text{DippP}$ obtained by SEPR and (b) simulation with third order perturbation theory and corrected for slow tumbling..... 135

Figure 4.6. (a) Experimental frozen solution EPR spectrum of $\text{Tripp}_2\text{DippP}$ obtained by chemical oxidation and (b) simulation using second-order perturbation theory..... 136

Figure 6.1. RDE cell containing $[\text{Dipp}_4\text{P}_2]^{+\bullet}$ (blue solution) and $[\text{Dipp}_3\text{As}]^{+\bullet}$ (red solution) 152

Figure 6.2. SEPR cell containing (a) $[\text{Dipp}_4\text{P}_2]^{+\bullet}$ and (b) $[\text{Tripp}_2\text{DippP}]^{+\bullet}$ 154

Figure 6.3. ‘‘T’’ cell for chemical oxidation EPR experiment containing AgPF_6 and $\text{Tripp}_2\text{DippP}$ 155

List of Schemes

Scheme 1.1. Synthesis of first organo-substituted diphosphine	3
Scheme 1.2. Synthetic route for diphosphines using active metals	3
Scheme 1.3 Reduction of diarylphosphinous chlorides to tetraaryldiphosphines with <i>bis</i> -imidazolidenes.	6
Scheme 1.4. Reaction sequence in the reduction 2,4,6-tri(<i>t</i> -butyl)phenylphosphorous dichloride PArCl ₂	7
Scheme 1.5. Synthesis of tetrakis(2,4,6-triisopropylphenyl)diphosphine with organolithium reagent.	8
Scheme 1.6. Proposed mechanism of reaction of an organometallic reagent with phosphorus trichloride.	8
Scheme 1.7. Synthesis of tetrakis(2,4,6-triisopropylphenyl)diphosphine with a Grignard reagent.	9
Scheme 1.8. Synthesis of symmetrical diphosphines using a phosphide anion.....	9
Scheme 1.9. Synthetic route to unsymmetrical diphosphines.....	9
Scheme 1.10. Proposed mechanism of synthesis of unsymmetrical diphosphine	10
Scheme 1.11. Diphosphine addition to activated alkynes.....	11
Scheme 1.12. Proposed mechanism of diphosphine addition to activated alkynes	11
Scheme 1.13. Platinum and palladium complexes of <i>bis</i> (phosphino)ethenes	12
Scheme 1.14. Trimesitylphosphine.....	17
Scheme 1.15. Reaction of aryl organometallic reagents with halophosphines.....	18
Scheme 1.16. Reaction of mesityllithium or mesityl Grignard reagent with PCl ₃	18
Scheme 1.17. Order of addition in reactions of PCl ₃ with more than two equivalents of mesityllithium or mesityl Grignard	19
Scheme 1.18. Reaction of 2,4,6-triisopropylphenylcopper(I) with phosphorus trichloride	20
Scheme 1.19. Fluorescence of tris(9-anthryl)phosphine and its derivatives.	26
Scheme 1.20. Synthesis of crowded triarylphosphines from arylcopper(I) reagents	27
Scheme 3.1. Possible synthetic route of <i>tris</i> (4-bromo-2,6-diisopropylphenyl)phosphine via 4-bromo-2,6-diisopropylphenylcopper	63
Scheme 3.2. Possible synthetic route to (4-bromo-2,6-diisopropylphenyl) <i>bis</i> (2,6-diisopropylphenyl)phosphine via 4-bromo-2,6-diisopropylphenylcopper	64
Scheme 3.3. Synthesis of Dipp ₄ P ₂ by using excess Mg turnings.....	66
Scheme 3.4. Proposed synthetic route for Tripp ₄ P ₂ via the Grignard reaction.....	70
Scheme 3.5. Possible synthetic route for Tripp ₄ P ₂ by reduction of P–Cl bond by triphenylantimony	71
Scheme 3.6. Synthesis of 1,3,1',3'-tetraethyl- <i>bis</i> (2,2'-imidazolidene)	72
Scheme 3.7. Proposed synthetic route for tetraorganodiphosphines by using <i>bis</i> -imidazolidene.....	73
Scheme 3.8. Proposed synthetic route for Tripp ₄ P ₂ by reducing the mixed halophosphines.....	75
Scheme 3.9. Synthesis of 1,1,2,2-tetra- <i>tert</i> -butyldiphosphane	76
Scheme 5.1. Molecules still needed to complete the series.	141

Scheme 5.2. Suggested synthesis route for Cy_4P_2	143
Scheme 5.3. Suggested method for synthesis of $\text{TrippDipp}_2\text{P}$	144

List of Abbreviations

A	area
Å	angstrom
AC	alternating current
A_i	hyperfine coupling constant
a_i	hyperfine splitting constant
B	magnetic field
B3LYP	Becke's Three Parameter Hybrid Functional Using the Lee, Yang, and Parr Correlation Functional
${}^n\text{Bu}$	n-butyl
${}^t\text{Bu}$	<i>tert</i> -butyl
C, conc	concentration
Cc	cobaltocene
CV	cyclic voltammetry
Cy	cyclohexyl
COSY	homonuclear correlated spectroscopy
D	diffusion coefficient
DC	direct current
DPPH	1,1-diphenyl-2-picryl-hydrazyl
DFT	density functional theory
Dipp	2,6-diisopropylphenyl group
eV	electron Volt
E	potential
$E_{1/2}$	half-wave potential
E°_f	formal electrode potential
endo	within
E_p^a	anodic peak potential
E_p^c	cathodic peak potential
EPR	electron paramagnetic resonance
eqn	equation
exo	outside; external
ex	situ external
F	faraday constant
Fc	ferrocene
g	Landé splitting energy
GC	glassy carbon
g	gram
h	Planck constant
\hat{H}_s	spin Hamiltonian
HFS	hyperfine splitting
HOMO	highest occupied molecular orbital
Hz	Hertz
I	spin
i.e.	that is

in situ	in the original position
I_L	Levich current
I_p	peak current
ⁱ Pr	isopropyl
IUPAC	International Union of Pure and Applied Chemistry
kJ	kilojoule
LT	low temperature
LUMO	lowest unoccupied molecular orbital
LW	line width
LCAO	linear combination of atomic orbital
Me	methyl
Mes	2,4,6-tri-methylphenyl
mL	milliliters
mmol	millimole
MO	molecular orbital
M	moles per liter
MO	molecular orbital
mT	millitesla
mV	millivolt
NMR	nuclear magnetic resonance
n	number of electrons
ORTEP	Oakridge thermal ellipsoid plot
Ph	phenyl
Q	charge
R (or variations of, i.e. R')	alkyl or aryl substituent
<i>R</i>	molar gas constant
RDE	rotating disk electrode
rms	root mean square
RPM	rotations per minute
RT	room temperature
Ru	solution resistance
s	second
SEEP	simultaneous electrochemical electron paramagnetic resonance
SOMO	singly occupied molecular orbital
SCF	self-consistent field
STO	Slater-type orbital
THF	tetrahydrofuran
Tripp	2,4,6-triisopropylphenyl
T	temperature
t	time
V	volt
σ	sigma
v	scan rate
°C	degrees Celsius

α	transfer coefficient
ω	angular frequency of rotation
ν_k	kinematic viscosity
μ_B	Bohr magneton
π	pi

Chapter 1

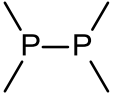
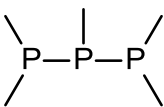
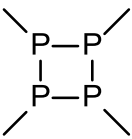
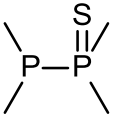
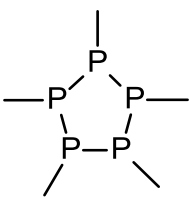
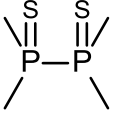
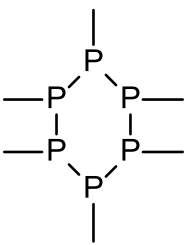
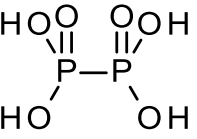
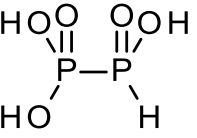
Introduction

1.1 Introduction to the chemistry of the phosphorus-phosphorus bond

The decade of the 1960s was a period of intense interest in compounds involving phosphorus-phosphorus bonds, which were known since the late 1800's. Several reviews which deal with the chemistry of diphosphines were summarized by Huheey, and there are monographs by Maier,¹ Paddock,² and Sasse.³ Major classes of compounds involving phosphorus-phosphorus single bonds are shown in Table 1.1.⁴

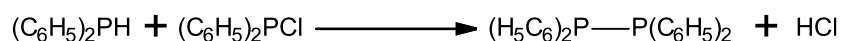
The name “diphosphine” has replaced “biphosphine” for P_2H_4 and its derivatives, which was commonly used from the 1960's until recently. More recently, the International Union of Pure and Applied Chemistry (I.U.P.A.C), which is the governing body for the discipline of chemistry world-wide, has adopted “phosphane” and “diphosphane” for R_3P and R_2PPR_2 , respectively. However, in this thesis use of the older terms “phosphine” and “diphosphine” has been chosen because of the prevalence of usage in the English-speaking world. The study of diphosphines is still of ongoing value because of intrinsic interest in the bonding and the role of non-bonded electrons on adjacent atoms. Furthermore, they can provide useful models for understanding other compounds with element-element bonds. First of all, they only have one such bond, and secondly, the bonding environment can be “tuned” by varying the “R” substituents in R_2PPR_2 . A better understanding of bonding can then be used to make other di- and polyphosphines and contributes to a better understanding of heavier non-metal chemistry.

Table 1.1. Structures involving P–P bonds

	Diphosphines	P_4S_3, P_4S_5, P_4S_7	Phosphorus sulfides
	Triphosphines		Cyclotetraphosphines
	Diphosphine monosulfides		Cyclopentaphosphines
	Diphosphine disulfides		Cyclohexaphosphines
	Hypophosphoric acid	P_x	Elemental phosphorus
	Diphosphorous acid		

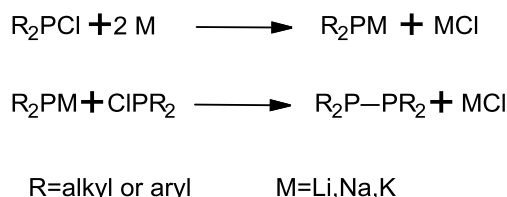
The simplest compound involving a P–P bond, diphosphine (P_2H_4), has been prepared by several methods over the years. The simple reaction of white phosphorus with a strong base and the neutral hydrolysis of various metallic phosphides, like calcium phosphide, are typical preparative methods.⁵ However, unlike hydrazine, diphosphine is a very reactive and unpleasant

material that can only be handled under stringent air-free conditions. The most studied organo-substituted diphosphine has been tetraphenyldiphosphine, which has been made by several methods.^{6,7} In 1888, Dorken and coworkers pioneered its preparation by the reaction of diphenylphosphine with diphenylphosphinous chloride (Scheme 1.1).⁸ This method was further developed by Gynane *et al.*⁹ and Burg *et al.*¹⁰ for the synthesis of several tetraalkyldiphosphines as well as some unsymmetrical diphosphines.



Scheme 1.1. Synthesis of the first organo-substituted diphosphine

One of most common methods for the preparation of diphosphines is the use of active metals such as lithium,¹¹ sodium,^{12,13,14,15,16} potassium,^{13,14} and magnesium^{13,17} reacting with phosphinous chlorides (Scheme 1.2) by reductive cleavage of the P–Cl bonds. In this type of reaction, the problem of competitive cleavage of the newly formed P–P bond can be minimized by using a metal that is less reactive and by keeping the reaction temperature as low as possible.¹⁸ There are several reports on making diphosphines using other methods such as: desulfurization of diphosphine disulfide,¹⁴ metal organophosphide, metal-halogen exchange,⁶ breakdown of more complex structures that involve several P–P bonds such as the preparation of P₂H₄ by OH[−] cleavage of the P₄ molecule,¹⁹ etc.



Scheme 1.2. Synthetic route for diphosphines using active metals

In the case of diphosphine, the two phosphorus atoms are bonded by a σ -bond and a lone pair of electrons remains on each atom. The thermal stability of diphosphine itself is very low, whereas substitution by alkyl, perfluoroalkyl, or aryl groups increases the thermal stability to above 200 °C.⁵ There are some reports on the thermal stability of some diphosphines up to 300 °C.²⁰ On the other hand, the homolytic cleavage of the P–P bond can be considered as a useful source of reactive monophosphorus compounds. For instance, a series of alkali metal organophosphides has been produced by alkali metal cleavage of diphosphines.^{7,11,21,22} As expected, the ease of cleavage change with the type of substituent. For example, the electron-withdrawing effect of the aryl groups and the stabilization of the unpaired electron in R_2P by delocalization onto the benzene rings makes the P–P bond weaker for Ar_2PPAr_2 than in the case of alkyl substituents. A common reaction for this class of compounds are reductive cleavage of the P–P bond with organometallic reagents such as LiC_6H_6 , LiC_2H_5 , $Mg(C_2H_5)_2$, etc. Very efficient oxidative cleavage with equimolar quantities of the halogens at room temperature occurs for both symmetrical^{12,23,24} and unsymmetrical diphosphines, leading to the corresponding halophosphines.^{25,26} In principle, substituted diphosphines do not react with water at room temperature but under more harsh conditions, hydrolytic cleavage of the P–P bond is possible. Cleavage of the P–P bond of a diphosphine can also be achieved by hydrogenation in the presence of a Raney nickel²⁷ or active copper catalyst.

There are six limiting rotational conformations for symmetrical diphosphines with chemical formula P_2X_4 in which X = hydrogen, halogen, alkyl, perfluoroalkyl, or aryl substituent (Figure 1.1). As illustrated, *syn* (eclipsed) (**a**) or semi-eclipsed (**b**), and (**c**) are expected to be rotationally-unstable maxima because of steric repulsion between the substituents. Hence, the remaining conformations *anti* (staggered) (**d**) or *gauche* (**e**) and (**f**) seem more reasonable choices

for the most stable conformers of diphosphines. In practice, presumably due to remote steric interactions of the substituents, several bulky diphosphines adopt conformations that are remarkably close to semi-eclipsed (see Section 1.3).

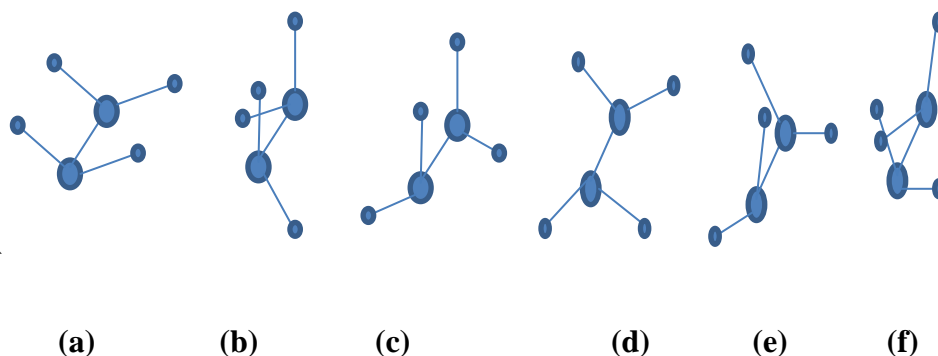


Figure 1.1. Possible conformations of diphosphines

1.2 Further background on the synthesis of tetraorganodiphosphines

Various synthetic routes have been employed to make tetraorganodiphosphines, including the early methods discussed above, as well as more complicated approaches that seem to be necessary for more bulky substituents. Here the three most common methods which have been recently used will be summarized.

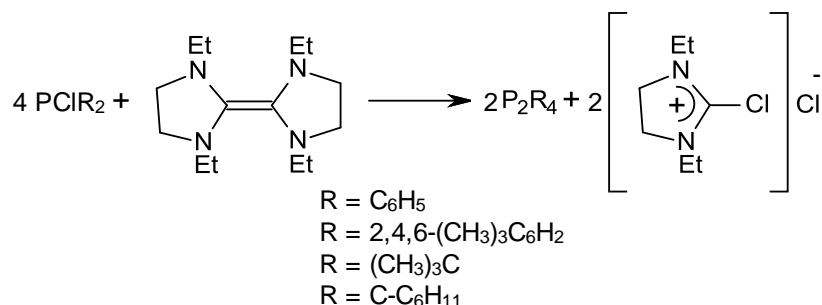
1.2.1 Reduction with *bis*-imidazolidenes

In 1986, two research groups introduced 1,3,1',3'-tetraethyl-*bis*(2,2'-imidazolidene), (Scheme 1.3), as a reagent for the reduction of P–Cl bonds in phosphonous ($\text{P(O)R}_2\text{Cl}$) or phosphinous chlorides (PR_2Cl) to produce compounds with phosphorus-phosphorus single bonds. These workers preferred this unusual reducing agent because its reactions are rapid at room temperature when initiated photochemically, in contrast to the use of metals, which tend to have sluggish reactions needing high temperatures and long reaction times. High yields of

tetraorganodiphosphines (R_4P_2) were produced by this method as is tabulated in Table 1.2.⁵ The reaction shown in Scheme 1.3 was successful for the synthesis of a series of R_4P_2 even in the absence of photochemical initiation.

Table 1.2. Some compounds prepared using *bis*-imidazolidenes

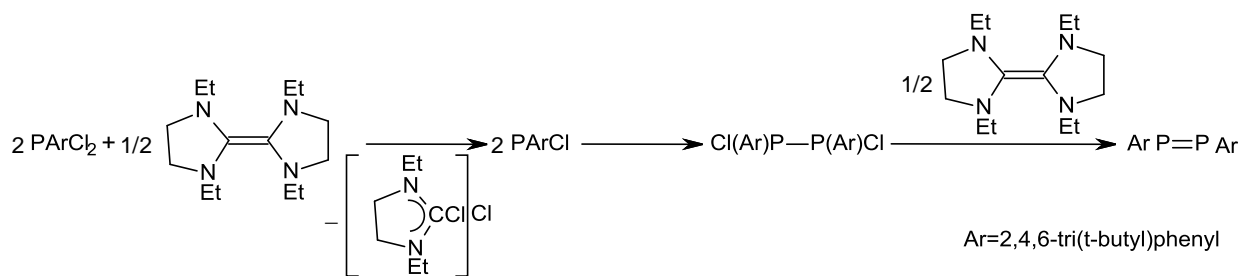
R group in R_4P_2	Yield (%)
C_6H_5	88
2,4,6- $(CH_3)_3C_6H_2$	73
$(CH_3)_3C$	57
<i>cyclo</i> - C_6H_{11}	50



Scheme 1.3. Reduction of diarylphosphinous chlorides to tetraaryldiphosphines with *bis*-imidazolidenes

The imidazolidene reaction is thought to proceed via formation of a phosphinyl radical ($\dot{P}R_2$), which is in equilibrium with dimeric tetraorganodiphosphines (R_4P_2), and a carbonium salt byproduct which is precipitated during the reaction. In contrast to heterogeneous reduction of phosphinous halides (PR_2X) to tetraorganodiphosphines (P_2R_4) with active metals, which need high temperatures and long reaction times, the imidazolidene is a homogeneous reagent which reacts at room temperature, especially when photochemically initiated.^{9, 11} This method has also been used for the preparation of diphosphenes (with $P=P$ double bonds) by reduction of phosphonous dichlorides ($ArPCl_2$) instead of R_2PCl . Scheme 1.4 demonstrates how this reaction

was used to prepare *bis*(2,4,6-*tert*-butylphenyl)diphosphene using two equivalents of a *bis*-imidazolidine reagent.



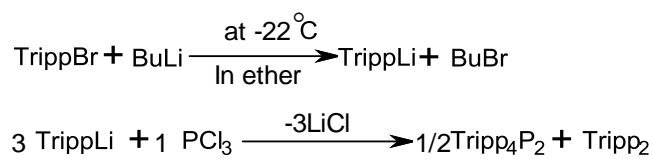
Scheme 1.4. Reaction sequence in the reduction 2,4,6-tri(*t*-butyl)phenylphosphorus dichloride PArCl_2

1.2.2 Reactions of organolithium and Grignard reagents

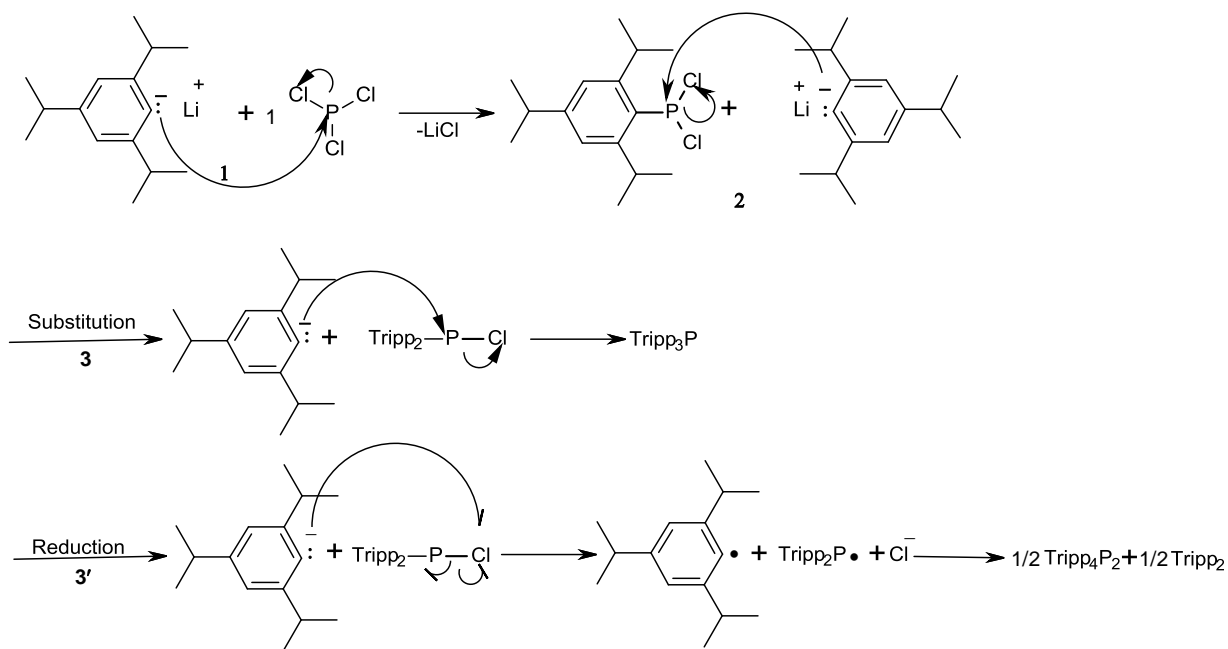
It has long been known that organolithium and Grignard compounds reacting with phosphorus(III) halides sometimes lead to the preparation of compounds with P–P bonds rather than the naively expected substitution products.²⁸

Quite recently, Brady *et al.* reported the accidental synthesis and characterization of the novel very congested tetrakis(2,4,6-triisopropylphenyl)diphosphine (Tripp_4P_2) from the reaction of PCl_3 with an excess of 2,4,6-triisopropylphenyllithium, Scheme 1.5 (or the equivalent Grignard reagent, Scheme 1.7), in 70% yield.²⁹ This is just such an example in which the lithium reagents do not lead to the expected triarylphosphine, probably as a consequence of steric bulk of the Tripp lithium reagent. Interestingly, incomplete substitution coupled with reduction of this kind is better known for Grignard than for aryllithium reagents. Presumably, these reactions proceed in three steps as shown in Scheme 1.6, with the two first steps involving nucleophilic substitution by the organometallic nucleophiles, whereas the last step can follow either the path of reduction ($\mathbf{3}'$) or substitution of the final P–Cl bond. The radical formed in $\mathbf{3}'$ is then presumed

to dimerize to a diphosphine. Generally, the reason that sometimes the reduction reaction is more favored than substitution depends on different parameters like the nature of the leaving group, the degree of steric congestion (especially in close proximity to the phosphorus nucleus), the relative reducing power of the organometallic reagent (itself linked to the place of the metal on the metal-activity scale) and likely the specific conditions of the reaction such as solvent(s) and temperature.



Scheme 1.5. Synthesis of tetrakis(2,4,6-triisopropylphenyl)diphosphine with organolithium reagent



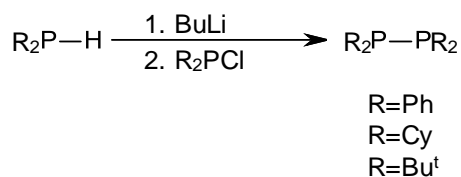
Scheme 1.6. Proposed mechanism of reaction of an organometallic reagent with phosphorus trichloride



Scheme 1.7. Synthesis of tetrakis(2,4,6-triisopropylphenyl)diphosphine with a Grignard reagent

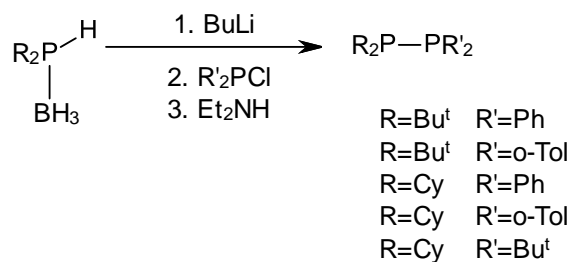
1.2.3 Preparation of phosphines *via* lithiated phosphide anions

One of the most common routes to make symmetrical diphosphines $\text{R}_2\text{P-PR}_2$ (where $\text{R}=\text{Ph}$, Cy , or Bu^t) is by the prior formation of phosphide anions such as R_2PLi from the reaction of R_2PH with a strong base and then reacting the anion with R_2PCl (Scheme 1.8).³⁰



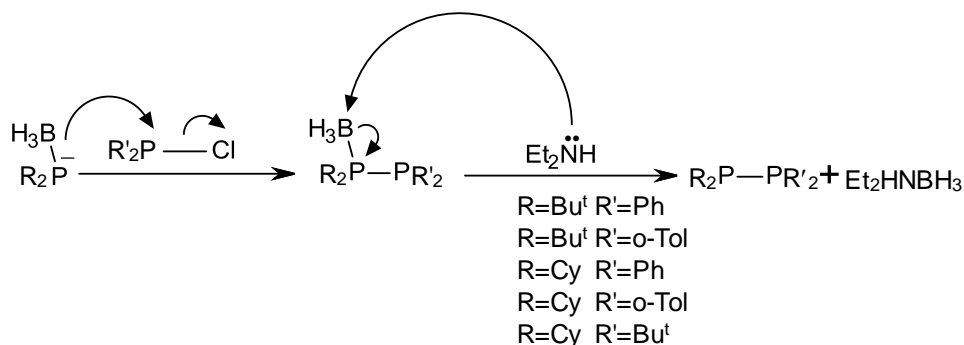
Scheme 1.8. Synthesis of symmetrical diphosphines using a phosphide anion

Unsymmetrical diphosphines can be made by the same method with the desired product made in 40-75% yield (according to ^{31}P NMR) but contaminated with significant amounts of symmetrical diphosphines and other byproducts.²¹ A significant improvement on this general approach and which yields pure unsymmetrical diphosphines could be achieved by using the borane adducts of the secondary phosphines (Scheme 1.9) in place of the phosphines themselves.



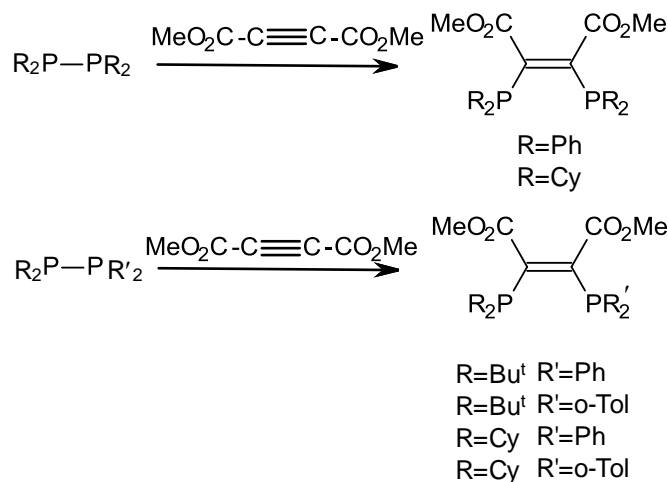
Scheme 1.9. Synthetic route to unsymmetrical diphosphines

The key to this improvement, as is illustrated in Scheme 1.10, is that the phosphorus anionic centre is more crowded by virtue of the BH₃ group, and this represses “scrambling” reactions that lead to symmetrical adducts. One disadvantage of this approach is the need to remove the BH₃ protecting group, which is done by making use of Et₂NH. The net result leads to the synthesis of unsymmetrical diphosphine.

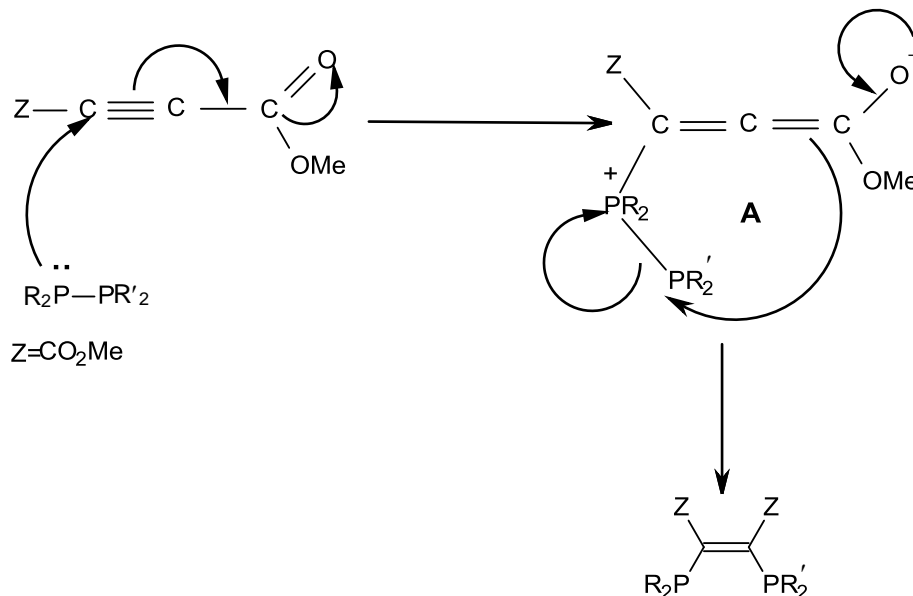


Scheme 1.10. Proposed mechanism of synthesis of unsymmetrical diphosphine

Although diphosphines have been known for over one hundred years, there are few reports on their applications. As part of the investigation just discussed, these symmetrical and unsymmetrical tetraalkyl or tetraaryldiphosphines were used to generate novel, useful chelate ligands. The symmetrical and unsymmetrical diphosphines react with dimethylacetylene dicarboxylate (DMAD), ZC≡CZ (Z=CO₂Me), in toluene at ambient temperature to give R₂PZC=CZPR₂ or R₂PZC=CZPR'₂ (Scheme 1.11). Note that this reaction did not occur when all four R groups on the diphosphine were ^tBu, even at elevated temperatures, but the reactions were successful if one half of the diphosphine is a ^tBu₂P group.³⁰



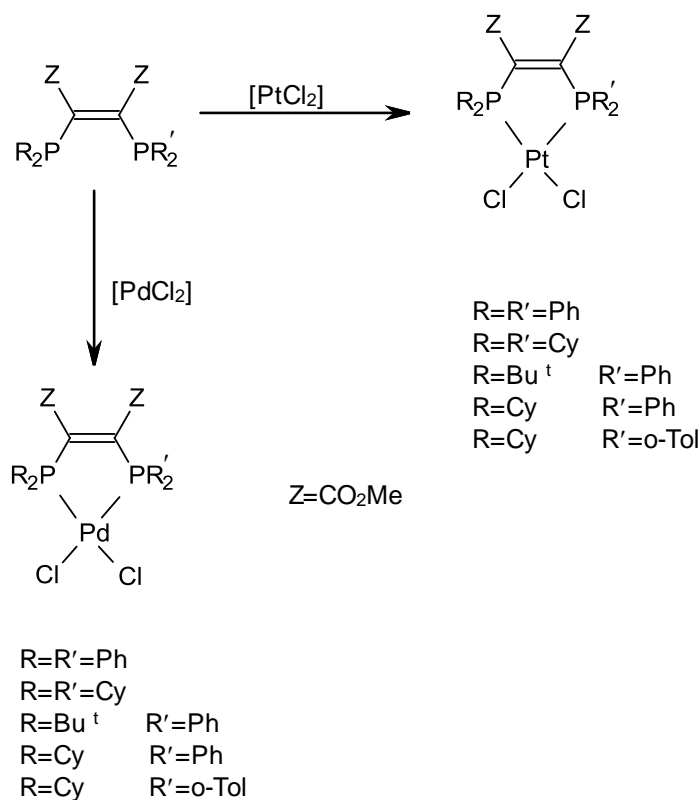
Scheme 1.11. Diphosphine addition to activated alkynes



Scheme 1.12. Proposed mechanism of diphosphine addition to activated alkynes

As shown in Scheme 1.12, the zwitterionic intermediate A can be formed in the nucleophilic attack by the diphosphine on the Michael-addition-activated alkyne in the first step and then in the second step, intermolecular rearrangement gives the *cis*-substituted chelating *bis*(phosphine). The rate of the first step in Scheme 1.12 would depend on the electrophilicity of the alkyne and the nucleophilicity of the diphosphine. The utility of these new

bis(phosphino)alkene ligands has been illustrated by the preparation of several chelate complexes with PtCl₂ and PdCl₂ (Scheme 1.13).¹⁸



Scheme 1.13. Platinum and palladium complexes of *bis*(phosphino)ethenes

1.3 Structural properties of diphosphines

Among the more than thirty reported X-ray crystallographic studies of tetraorganodiphosphines (R₄P₂) listed in the Cambridge Crystallographic Database, the majority crystallize in the antiperiplanar (*anti*) conformation, which seems to be more favorable especially for less congested species (non-bulky substituents) like tetramethyl²³ and tetramesityl diphosphines.²⁵ Surprisingly, a few very bulky alkyl diphosphines seem to prefer a conformation that is very close to semi-eclipsed. In the *anti* conformation of diphosphines, the lone pairs on each phosphorus occupy the maximum spatial separation. The *gauche* conformation does not

allow the same degree of separation as *anti* does, perhaps because the substituents occupy more space than the lone pairs. Table 1.3 presents bond lengths and the sums of the bond angles for some common tetraorganodiphosphines for which structures have been reported.²⁹

Table 1.3. Summary of P–P bond lengths and sums of the –E– (E: P, As) bond angle of some representative tetraorganodiphosphines

R groups in R ₄ P ₂ compounds	P–P bond length(Å)	$\sum\{\angle\text{-E-}\}(\text{°})$	Conformation
CH(SiMe ₃) ₂	2.3103(7)	316.2	Between anti & eclipsed
Tripp	2.2461(16)	319.8	Close to anti
^t Bu ³¹	2.235(1)	330.0	Close to eclipsed
Mes	2.260(1)	311.6	Between anti & eclipsed
CF ₃	2.246(2)	-	Anti (1 site sym.)
Cy	2.215(3)	313.0	Close to eclipsed
Ph	2.211(2)	298.3	Anti
Me	2.212(1)	295.4	Anti

In 1980 Baxter *et al.*²⁵ published a paper comparing the X-ray crystal structure and low-temperature ¹H NMR spectrum of tetramesityldiphosphine (Mes₄P₂). In the crystal, the structure is between *anti* and eclipsed and possesses crystallographic C₂ symmetry. The low-temperature NMR study was consistent with retention of C₂ symmetry in solution. These workers concluded that the conformational behavior of these kinds of compounds do not seem to be affected by conjugation between the phosphorus lone pair and the aryl π system, refuting a common hypothesis previously put forward for this class of molecule.

In 2000, Hinchley *et al.* published a communication,³² later followed by a full paper,³³ reporting a highly unusual diphosphine with four “supersilyl” (CH(SiMe₃)₂) substituents which can behave as an energy storage reservoir. In contrast to other diphosphines with bulky substituents, which protect their P–P bond from cleavage, this molecule results in cleavage of the

P–P bond upon dissolution, melting or evaporation. A comprehensive investigation showed that the monomeric phosphinyl radical, $\cdot\text{P}\{\text{CH}(\text{SiMe}_3)_2\}_2$ relaxes the orientation of the alkyl groups. However, formation of the P–P bond requires a much higher-energy orientation of the alkyl groups which is possible because of the shape and flexibility of the $\text{CH}(\text{SiMe}_3)_2$ groups. Thus, the dimer formed at low temperature acts like an energy storage reservoir similar to a compressed spring, energy that is released upon P–P bond cleavage at higher temperatures. Interestingly, the potential energy of steric repulsion is not reflected in an elongated P–P bond, but is evidenced primarily by the deformation of the ligands.

1.4 Electrochemical and spectroelectrochemical properties of diphosphines

Very few electrochemical studies of tetraorganodiphosphines have been reported. The most comprehensive of these came from Tordo and coworkers who contrast the behavior of this class with tetraalkylhydrazines.³⁴ A very cursory report on a tetraaryldiphosphine bearing remote phenothiazyl substituents provides little additional information.³⁵ In contrast to radical cations of hydrazines, which have planar geometries, the Tordo group provided electron paramagnetic resonance (EPR) spectroscopic evidence for the retention of considerable pyramidal character for the phosphorus centers of tetraaryldiphosphine radical cations.³⁶ Cyclic voltammetry studies on tetraaryldiphosphines and EPR data on the radical cations which are reported until now are listed in Table 1.4 and Table 1.5, respectively.³⁷

The cyclic voltammetry study of tetraaryldiphosphines showed single-electron quasi-reversible oxidation at room temperature. By taking a closer look at the CV data it can be concluded that the half-lives of these cationic species are related to the bulk of the phosphorous ligands. Thus the larger $I_p(c)/I_p(a)$ ratio for the bulkier diethylphenyl species than for the two with two *ortho* dimethylphenyl groups is reflected in longer half-lives for the radical cations.

Furthermore, tetraphenyldiphosphine exhibited a completely irreversible oxidation process in cyclic voltammetry and no EPR signal could be observed for the radical cations.³⁸ In comparison with triarylphosphines bearing the same substituents, the symmetric tetraaryldiphosphine and radical cation species with bulky aryl substituents experience less steric congestion due to the P–P being considerably longer than the bonds to the organic substituents; thus the phosphorus atoms are more pyramidal based on the EPR evidence. In addition, the EPR study demonstrated that the diphosphine radical cations have longer half-lives than similar triarylphosphine radical cations.

Table 1.4. Summary of cyclic voltammetry studies of tetraaryldiphosphines^a

R group in R ₄ P ₂ compounds	$E_p(a)/V^b$	$E_p(c)/V^c$	$I_p(c)/I_p(a)^d$
2,6-dimethylphenyl	0.795	0.715	0.92
2,4,6-trimethylphenyl	0.718	0.599	0.95
2,4,6-triethylphenyl	0.592	0.477	1.00

^aCyclic voltammetry ($v = 100$ mV/s) at a stationary platinum electrode in butyronitrile containing 0.1M tetra-*n*-butylammonium hexafluorophosphate. ^bAnodic peak potential vs. SCE. ^cCathodic peak potential vs. SCE. ^dRatio of peak currents.

Table 1.5. EPR data for radical cations of tetraaryldiphosphines

R group in R ₄ P ₂ ⁺⁺ compounds	a/mT^f	G	a_{\parallel}/mT	a_{\perp}/mT	g_{\parallel}	g_{\perp}	$T/^{\circ}$	Ref
2,6-dimethylphenyl	17.1	2.0060					18	34
	17.3	2.006	27.9	12.0	2.002	2.008	-196	
2,4,6-trimethylphenyl	17.0	2.0063					17	37
	16.9	2.006	26.8	12.0	2.002	2.008	-196	
2,4,6-triethylphenyl	17.5	2.0061					20	41
	17.7	2.006	28.1	12.5	2.002	2.008	-196	

In butyronitrile containing 0.1 M tetra-*n*-butylammonium hexafluorophosphate.^fObtained by using the equation: $g = (g_{\parallel} + 2g_{\perp})/3$; $a = (a_{\parallel} + 2a_{\perp})/3$ in a frozen solution (see Section 4.3)

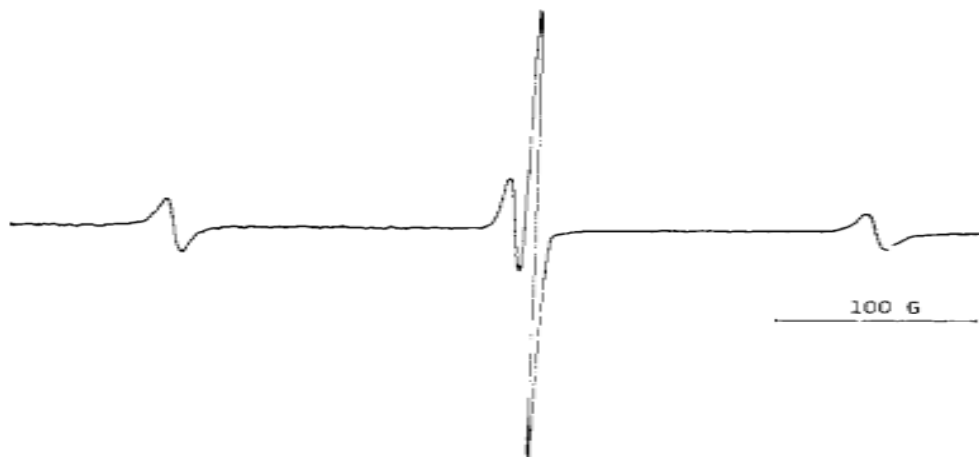
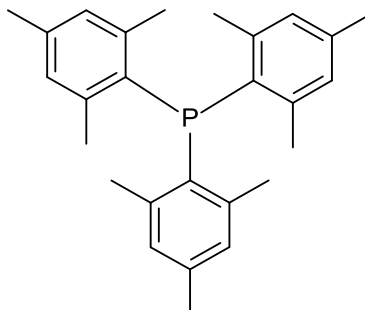


Figure 1.2. EPR spectrum of tetrakis(2,4,6-triethylphenyl)diphosphine radical cation. electro generated in butyronitrile 0.1 M in tetra-n-butylammonium hexafluorophosphate at 296 K. (Reprinted with permission from (*J. Am. Chem. Soc.*, 1985, 107 (24), pp 7193).³⁷

Studies on the structures of R_4N_2 and R_3N have shown that there are drastic changes in the structure of the molecules by losing one electron and forming the $(R_4N_2)^{+\bullet}$ and $R_3N^{+\bullet}$. Evidence from EPR spectroscopy shows that the whole molecule becomes planar in the case of $(R_4N_2)^{+\bullet}$ with maximum overlap between the two 2p orbitals, which is similar with the observation of $R_3N^{+\bullet}$.^{39,40} By contrast, removing one electron from R_3P results in considerable flattening in the radical cation, but the structure remains pyramidal as indicated by the large size of the hyperfine coupling constants. EPR spectra of $(R_4P_2)^{+\bullet}$ compounds are expected to show a 1:2:1 triplet structure due to the coupling of the unpaired electron with two equivalent phosphorus nuclei. However, because of the strength of the electron-phosphorus coupling, the degeneracy of the two transitions that compose the central line of the triplet appears as a doublet and in the liquid phase, four line EPR spectra are observed for $(R_4P_2)^{+\bullet}$ radical cations (Figure 1.2).³⁴ A summary of the EPR data obtained by these workers is reported in Table 1.5.

1.5 Introduction to triarylphosphines

Due to the broad area of catalytic applications of trialkyl and triarylphosphines, these ligands played an important role in organometallic coordination chemistry. The steric bulk in phosphines can be classified by using the concept of Tolman's cone angle. Historically, trimesitylphosphine (Mes_3P , Mes = 2,4,6-trimethylphenyl)^{42, 43} (Scheme 1.14) has been known as the crowded triarylphosphine which, although it is very bulky, is still able to form metal complexes like Mes_3PAuCl .⁴⁴



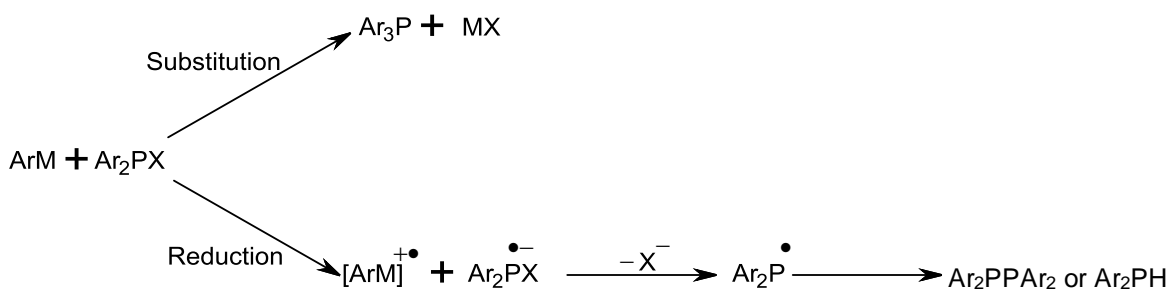
Scheme 1.14. Trimesitylphosphine

Their unique structures, properties, and reactivity have attracted a lot of interest toward triorganophosphines. Three main aspects of their properties have been investigated in recent years. Firstly, in crowded triarylphosphines, changing the substituents can lead to change in crystal structures and in solution dynamic behavior. Secondly, due to adequate steric protection of bulky groups, triarylphosphines are able to generate a stable radical cation. Thirdly, this group of compounds has been applied in transition metal catalysts as supporting ligands.⁴⁵

1.5.1 Synthetic methods for triarylphosphines

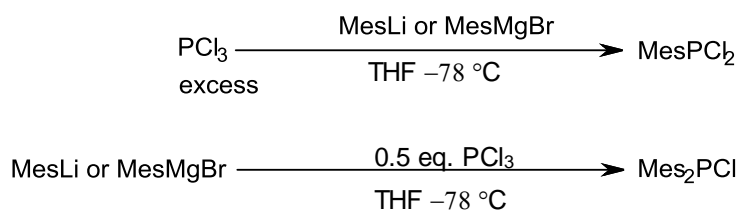
The most common methodology to make triarylphosphines is the coupling of aryl organometallic reagents with phosphorus halides. Reaction of aryl organometallic reagents such

as aryl lithium and Grignard reagents with diarylhalophosphines (mostly diarylchlorophosphines) is commonly used as a method for the synthesis of triarylphosphines (Scheme 1.15).⁴⁵ One of the most common problems in synthesis of the crowded triarylphosphines is finding a way to add the third and last aryl group to form such a crowded molecule. Sasaki and coworkers have done a wide range of synthetic work on this series of compounds. In some cases, bulky aryl groups undergo side reactions, which results in formation of diphosphines (Ar_2PPAr_2) or secondary phosphines (Ar_2PH).



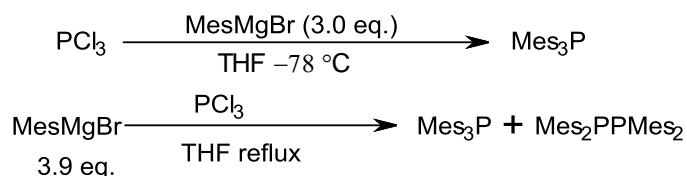
Scheme 1.15. Reaction of aryl organometallic reagents with halophosphines.

Control over stoichiometry, solvent and temperature is essential in the synthesis of arylphosphines. For example, addition of mesityllithium or mesitylgrignard^{46,47} to excess phosphorus trichloride gives dichloromesitylphosphine.^{48,49} Addition of mesitylmagnesium bromide⁵⁰ or mesityllithium to 0.5 equivalents of phosphorus trichloride gives chlorodimesitylphosphine (Scheme 1.16),⁵¹ while addition of phosphorus trichloride to mesityllithium at $-78\text{ }^\circ\text{C}$ in THF mainly affords dichloromesitylphosphine.



Scheme 1.16. Reaction of mesityllithium or mesityl Grignard reagent with PCl_3

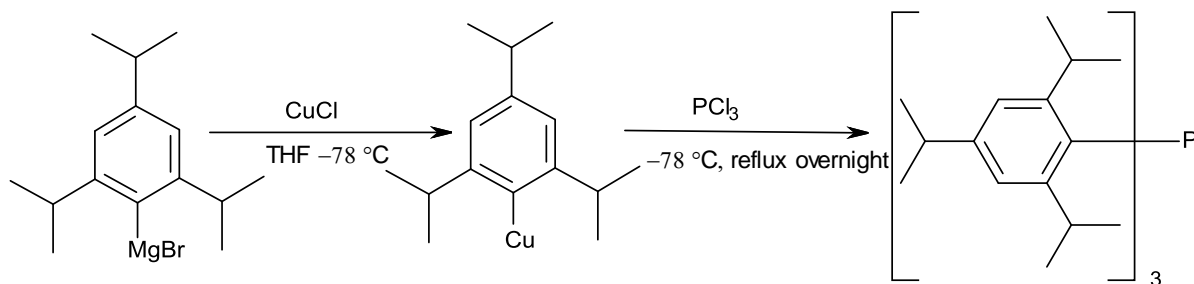
The synthesis of trimesitylphosphine requires the addition of three equivalents of mesitylmagnesium bromide to phosphorus trichloride at $-78\text{ }^{\circ}\text{C}$ in THF (Scheme 1.17). The order of addition is important. Otherwise, introduction of the third mesityl group competes with a redox reaction leading to tetramesityldiphosphine.^{52,53} For example, the addition of phosphorus trichloride to an excess of mesityl Grignard in THF at RT followed by reflux gives trimesitylphosphine in only 24% yield and results in production of a lot of tetramesityldiphosphine.



Scheme 1.17. Order of addition in reactions of PCl_3 with more than two equivalents of mesityllithium or mesityl Grignard

Other experimental work suggested that Grignard reagents are unsuitable for more crowded phosphines such as tris(2-methyl-1-naphthyl)phosphine, tris(2,4,6-triethylphenyl)phosphine and tris(2,4,6-triisopropylphenyl)phosphine. However, arylcopper reagents such as mesitylcopper and 2,4,6-triisopropylphenylcopper can be utilized for synthesis of these compounds. In a system such as tris(2,4,6-triisopropylphenyl)phosphine, ^{31}P NMR spectra recorded during the reaction illustrated that making the corresponding phosphines requires overnight reflux to convert all the dichloro(2,4,6-triisopropylphenyl)phosphine to the product (Scheme 1.18).⁴⁵ In addition, Dipp_3P was prepared previously in our lab by converting the Grignard reagent prepared from DippBr into $(\text{DippCu})_x$, and reacting it in situ with PCl_3 .⁵⁴ Aranyos *et al.* used a biphenylcopper reagent to prepare 2-(di-*tert*-butylphosphino)biphenyl.⁵⁵

Greenfield and Gilbertson used a complex sequence of organozinc followed by lithium cuprate reagents to prepare primary and secondary amino acid derivatives of Ph_2PX .⁵⁶



Scheme 1.18. Reaction of 2,4,6-triisopropylphenylcopper(I) with phosphorus trichloride

Average bond angles, lengths, oxidation potentials, and ³¹P NMR chemical shifts of some tris(2,4,6-trialkylphenyl)phosphines are shown in

Table 1.6. By taking a closer look at the data in Table 1.6, it can be concluded that by increasing the bulkiness of aryl groups, bond angles and lengths become larger but oxidation potentials become lower due to the stability of the radical cation in the presence of more bulky R groups.

Table 1.6. Summary of triarylphosphine characterization studies

Compound Name	Bond angle(°)	Bond length (Å)	$E_{1/2}/V^a$	$\delta^{31}\text{P}/\text{ppm}$
Ph_3P^{45}	103.0(1)	1.821(1)	1.03	-4.7
$\text{Mes}_3\text{P}^{57}$	109.7(5)	1.837(6)	0.41	-35.8
$\text{Dipp}_3\text{P}^{54}$	111.88(5)	1.852(2)	-	-49.7
$\text{Tripp}_3\text{P}^{45}$	111.5(1)	1.845(2)	0.16	-52.4

^a $E_{1/2} / V$ vs. Ag/Ag^+ in dichloromethane with 0.1 M ⁿBu₄NClO₄

1.5.2 Structural characterization of triarylphosphines

Various parameters such as average bond angles, sum of the bond angles, Tolman’s cone angles, and out-of-plane bending angles have been focused on and discussed in most papers in

this category. Crystal structures of bulky triarylphosphines show the pyramidal configuration with the three aromatic rings bound to the phosphorus aligned to form a propeller-shape molecule. High-lying HOMO orbitals resulting in lower oxidation potentials are reasonably expected for crowded triarylphosphines. In the 1970's, Mislow and co-workers found that bulky substituents can lead to substantial distortions in the structure of the pyramidal R_3P group as observed, for example, in the first X-ray diffraction structure determination of Mes_3P .⁵⁷ For instance, PH_3 has small internal angles of 93.6° in comparison with Mes_3P which has internal angles of 109.7° .⁵⁸ The much greater pyramidalization of PH_3 compared to NH_3 is at root a result of a smaller difference in the energy of the s and p valence orbitals in the case of the third-period element. This is related to differences in effective nuclear charge between the 2nd and 3rd period of the Table.

Recently, $Dipp_3P$ and $Tripp_3P$, which are the most sterically congested triaryl phosphines, were reported by our group⁵⁴ and Sasaki, Yoshifuji and coworkers, respectively.⁴⁵ A distinction has been made between steric bulk and steric shielding in triarylphosphines.⁵⁹ Hence, a single set of *ortho* substituents (2-position) can provide considerable steric shielding for the phosphorus lone pair, without any flattening of the phosphorus center. Meanwhile, the presence of substituents in both the 2- and the 6-positions of the aromatic rings induce steric pressure that leads to actual flattening of the phosphorus pyramid (Figure 1.3). For example, in $(2\text{-}^iPrC_6H_4)_3P$, which has all the substituents in the *exo* position, $\sum\{\angle CPC\} = 306.5^\circ$, while in $Dipp_3P$ and $Tripp_3P$, $\sum\{\angle CPC\} = 335.6^\circ$ and 334.4° due to the three bulky *endo* substituents which generate more steric pressure.

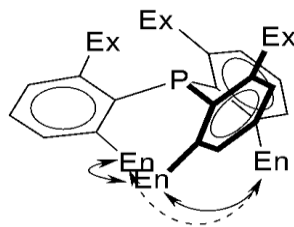


Figure 1.3. Illustration of the *endo* and *exo* substituents in triarylphosphines

Generally, it can be concluded that the flattening caused by the *endo* substituent causes the *exo* substituent to be pushed closer around the phosphorus atom and provides enhanced shielding for the lone pair in these compounds with the same *exo* substituent. Hence, larger substituents with high steric pressure push the orbital hybridization tendency towards flattening.

1.5.3 Electrochemical and spectroelectrochemical studies of triarylphosphines

One of the most attractive features of crowded triarylphosphines is high stability of the corresponding radical cations. In most cases, radical cations of triarylphosphine are highly reactive; for example, triphenylphosphine radical cations have to be formed by photolysis or radiolysis and studied in low-temperature. By contrast, crowded triarylphosphine radical cations can often be produced by either chemical or electrochemical oxidation. According to previous work in our group, Dipp₃P shows one chemically reversible oxidation process (Figure 1.4) on either Pt or GC as working electrodes in both CH₃CN and CH₂Cl₂ solvents.⁵⁴ A larger peak-to-peak separation compared to that of the internal references Cc⁺⁰ and Fc⁺⁰ (see Section 2.1.3), are in accord with the quasi-reversibility of the one-electron process:



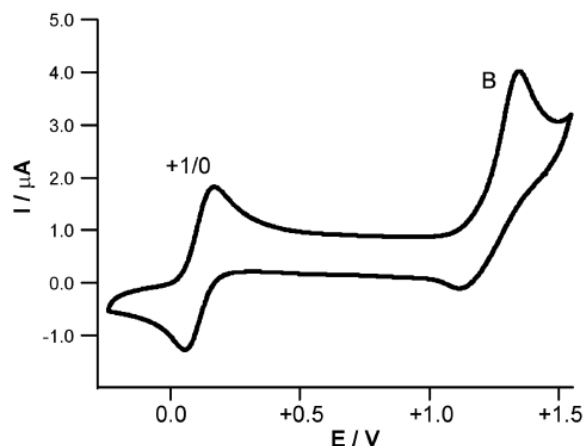


Figure 1.4. Cyclic voltammogram of Dipp₃P (0.20 mM) in CH₂Cl₂ solution containing 0.4 M ⁿBu₄NPF₆ under an atmosphere of dry N₂ recorded at a scan rate of 200 mV s⁻¹ using an Au macro disk electrode at 0 °C. Potentials vs. Fc⁺⁰. (Reprinted with permission from (*New J. Chem.* 2008, 32, 214)

The nature of the second, irreversible, oxidation process (B) in Figure 1.4 was not investigated in detail. The diffusion coefficient (*D*) for Dipp₃P⁺⁰ and Mes₃P⁺⁰ in CH₃CN was obtained by RDE (see Section 2.1.4) at 22 °C: *D* = 1.0 × 10⁻⁵ cm² s⁻¹ and *D* = 1.6 × 10⁻⁵ cm² s⁻¹, respectively. The measured rate of electron transfer was found to be slower in Dipp₃P⁺⁰ compared to Mes₃P⁺⁰. This is due to the fact that the isopropyl groups in Dipp₃P create a limited channel to the phosphorus lone pairs which makes the non-bonded phosphorus electrons less accessible.

Based on Table 1.7,⁵⁴ it can be concluded that the Dipp₃P⁺⁰ couple in CH₂Cl₂ solution is 0.15 V less cathodic than the isosteric Tripp₃P⁺⁰. Since the only difference between Dipp and Tripp is the ⁱPr groups in the *para* position, the difference between oxidation potentials should correspond to the inductive effect of the third ⁱPr. Comparing data from the following table indicates that the share of each ⁱPr group to the inductive effect will be 0.05 V.⁵⁴

Table 1.7. Comparative redox potentials for triaryl phosphines^a in V

Compound	CH ₂ Cl ₂ ^b	CH ₃ CN ^c
Ph ₃ P	0.88	1.04
Xyl ₃ P	0.34	0.04
Mes ₃ P	0.19	0.26
Dipp ₃ P	0.09	0.18
Tripp ₃ P	-0.06	0.04

^a Calculated by cyclic voltammetry from the average of oxidation and reduction peak potentials, scan rate = 0.2 V s⁻¹; ^b In CH₂Cl₂ at a Pt electrode containing 0.4 M ⁿBu₄NPF₆ and 1 mM in analyte, vs. Fc⁺⁰, measured against Cc⁺⁰, expressed vs. Fc⁺⁰ by subtracting 1.35⁶⁰ V. ^c In CH₃CN at a Pt electrode containing 0.1 M ⁿBu₄NPF₆ and 1 mM in analyte, measured against Cc⁺⁰, expressed vs. Fc⁺⁰ by subtracting 1.35.⁶⁰

Studies of the electrochemistry of triarylphosphines have shown that Ph₃P can form Ph₃P=O during electrochemical oxidation while the same thing occurs for Mes₃P in wet or oxygenated solvents. By contrast, in the case of Dipp₃P, the resulting CV or RDE in both extremely degassed and dried solvent and solutions which are prepared without any special care resulted in the same voltammograms. The stability of radical cations for both Dipp₃P and Tripp₃P can be related to the adequate steric shielding of the *exo* ⁱPr groups.

EPR spectra of Tripp₃P recorded as solutions at 22 °C and in a frozen glass at -143 °C (Figure 1.5) show the expected doublet with a hyperfine coupling to ³¹P of 23.9 mT. The peak-to-peak line widths in fluid solution spectra are between 0.5 and 0.6 mT. These relatively wide lines are due to unresolved proton hyperfine coupling. EPR data for other known triarylphosphines are summarized in Table 1.8.⁵⁴

Table 1.8. EPR data for Ar₃P^{•+} radicals

compound	Condition	g_{iso}	a_{iso}/mT
Dipp ₃ P ^{•+}	CH ₃ CN/22 ^{°a}	2.008	23.9
	CH ₂ Cl ₂ /22 ^{°b}	2.008	23.9
	CH ₂ Cl ₂ /-196 °C	2.007	22.7
	CH ₂ Cl ₂ /22 ^{°d}	2.008	23.9
Tripp ₃ P ^{•+}	CH ₂ Cl ₂ /20 ^{°e}	2.007	23.7
Duryl ₃ P ^{•+}	C ₃ H ₇ CN/-196 ^{°f}	2.0052	23.7
Xyl ₃ P ^{•+}	CH ₃ CN/-150 ^{°f}	2.0052	24.4
Mes ₃ P ^{•+}	C ₃ H ₇ CN/-196 ^{°g}	2.0052	24.0
Ph ₃ P ^{•+}	CFCl ₃ /-196 ^{°f}	2.006	29.9

^aSaturated solution (between 1×10^{-4} and 1×10^{-3} M) in CH₃CN containing 0.1 M ⁿBu₄NPF₆ at 22 °C. ^b 7×10^{-4} M in CH₂Cl₂ containing 0.1 M ⁿBu₄NPF₆ at room temperature. ^c Sample as in b but cooled to 130 K; $g = (g_{\parallel} + 2g_{\perp})/3$; $a = (a_{\parallel} + 2a_{\perp})/3$ for frozen solution (bolded) (see Section 4.3). ^d Prepared from a dilute solution of Dipp₃P in CH₂Cl₂ by chemical oxidation with solid AgClO₄. ^e Chemical oxidation with AgClO₄. ^f Prepared by electrolysis. ^g Electrolysis in n-butyronitrile.

EPR studies of such species proved the narrow range of oxidants available for formation of trimesitylphosphine radical cation such as tris(4-bromophenyl)aluminium perchlorate. By contrast, tris(2,4,6-triisopropylphenyl)phosphine can be oxidized by using more oxidants like silver(I) perchlorate, silver(I) tetrafluoroborate or bis(acetonitrile)dichloropalladium(II). Dipp₃P and Tripp₃P are more readily oxidized than the other species listed above, and moreover the resultant radical cations are more stable. For both of these reasons, a wider range of oxidants is suitable for producing radicals. As expected, EPR spectra of radical cations of triarylphosphines show two lines in solution and four or six lines in frozen solution due to the hyperfine coupling to the ³¹P nucleus (Figure 1.5).^{45,61}

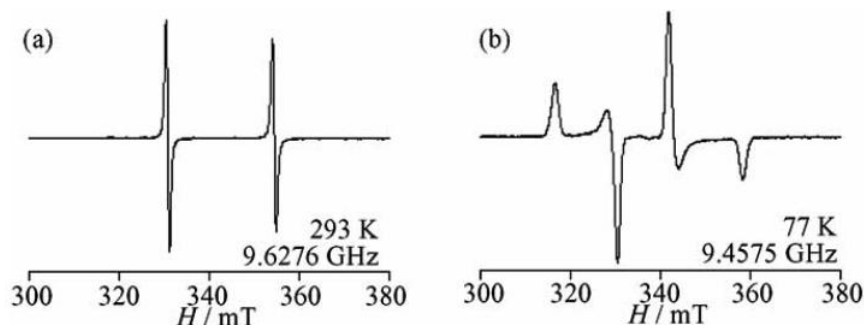
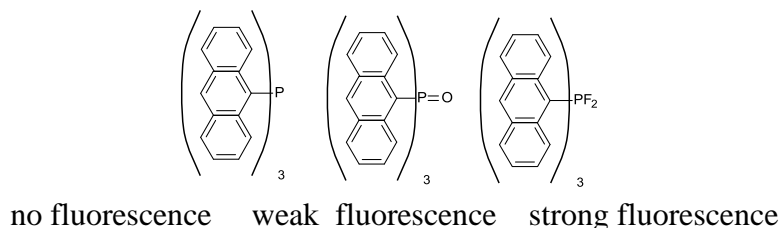


Figure 1.5. EPR spectra of radical cation of tris(2,4,6-triisopropylphenyl)phosphine at (a) 20 °C and (b) –196 °C obtained by oxidation with silver(I) perchlorate in dichloromethane.

(Reprinted with permission from *Current Organic Chemistry*, 2007, 11, 17-31).

1.5.4 Applications of triarylphosphines

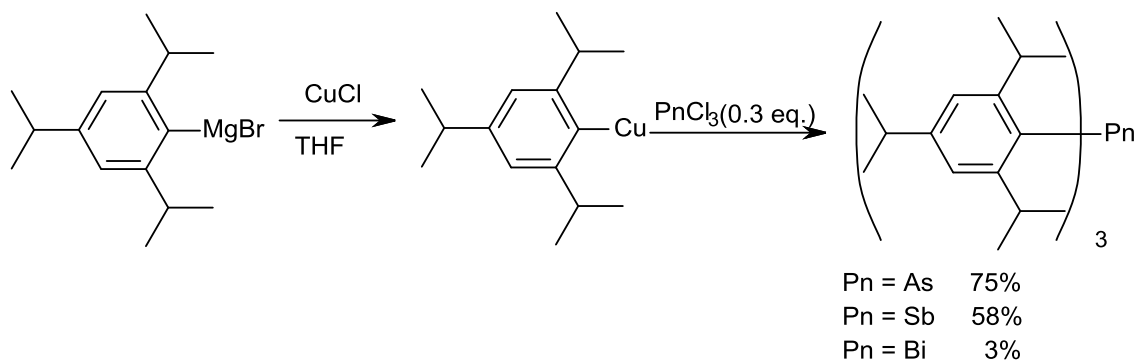
Crowded triarylphosphines played an important role in the chemistry of phosphines, and have attracted broad attention because of their unusual structures and properties. Since one of the most important applications of crowded triarylphosphines is in functional materials, especially those which have functional moieties, many studies have been done to take advantage of this application and to fully understand the properties of crowded triarylphosphines. As an example, some derivatives of tris(9-anthryl)phosphine carrying a functional moiety show fluorescence comparable to anthracene and 4,4'-diphosphinobiphenyl derivatives of biphenylenediamine can be utilized as hole injecting and transporting materials of electro-optic devices (Scheme 1.19).^{62,63, 64}



Scheme 1.19. Fluorescence of tris(9-anthryl)phosphine and its derivatives

1.6 Triarylsines

Other crowded triarylpnictogens such as arsine, stibine and bismuthine derivatives have been investigated alongside triarylphosphines. The same pattern has been observed for these series of crowded triarylpnictogens, which means that they have large bond angles and lengths around the pnictogen atoms and are reversibly oxidized to the stable radical cations at significantly low oxidation potentials due to both structural changes and steric protection by introduction of bulky aryl groups. The most crowded triarylpnictogens have tris(2,4,6-triisopropylphenyl) groups on arsenic, antimony, and bismuth, and were reported by Shigeru Sasaki and coworkers who have the highest list of publication for this series of compounds.⁶⁵ Aryl copper (I) reagents, which are less reactive as reducing agents, have been utilized to prepare these compounds. Tris(2,4,6-triisopropylphenyl)arsine (75%), -stibine (58%), and -bismuthine (3%), were synthesized by this method (Scheme 1.20).



Scheme 1.20. Synthesis of crowded triarylpnictogens from arylcopper(I) reagents

Like the crowded tris(2,4,6-triisopropylphenyl)phosphine, tris(2,4,6-triisopropylphenyl)arsine and tris(2,4,6-triisopropylphenyl)stibine have interlocked propeller shapes and the pnictogen atoms are covered with six *ortho* isopropyl groups. The bond lengths and angles become longer and larger as the *ortho* substituents of the aryl groups become more bulky by

comparison to other triarylpnictogens, and the tris(2,4,6-triisopropylphenyl)pnictogens have the longest bond length and largest bond angle for each element.

Lower oxidation potentials of the triarylpnictogens are associated with the fact that as the molecules become more crowded, the energy level of the lone pair (HOMO) is increased by enhanced planarity of the pnictogen atoms induced by steric congestion. Therefore, the 2,4,6-triisopropylphenyl substitutions have the lowest potentials. Table 1.9 can be helpful to get a better understanding of these investigations. Tris(2,4,6-triisopropylphenyl)arsine can be chemically oxidized by silver perchlorate in dichloromethane solution and electrochemically shows a reversible redox wave with the ratio of anodic and cathodic peaks as unity at a 30 mVs⁻¹ scan-rate at 20 °C.

Table 1.9. Average C–Pn bond lengths, C–Pn–C bond angles, and oxidation potentials of the crowded triarylphosphine, -arsine,-stibine

Triarylpnictogens	Bond length (Å)	Bond angle(°)	$E_{1/2}/V^a$
triphenylphosphine	1.821(1) ^{a,b}	103.0(1) ^b	1.03 ^c
Trimesitylphosphine	1.83 (2) ^d	110.0(7) ^d	0.41
tris(2,4,6-triisopropylphenyl)phosphine	1.845(2) ^e	111.5(1) ^e	0.16
Triphenylarsine	1.949(1) ^f	100.0 (4) ^f	1.18 ^c
Trimesitylarsine	1.976(4) ^g	105.9(3) ^g	0.73
tris(2,4,6-triisopropylphenyl)arsine	1.986(3) ^e	109.2(1) ^e	0.50
Triphenylstibine	2.141(5) ^h	97.3(3) ^h	1.05 ^c
Trimesitylstibine	2.183(8) ⁱ	105.3(1) ⁱ	0.76 ^c
tris(2,4,6-triisopropylphenyl)stibine	2.197(3) ^e	105.6(1) ^e	0.57

^a Reversible unless otherwise stated, V vs. Ag/Ag⁺ in dichloromethane with 0.10 M n-Bu₄NClO₄, scan rate: 30 mVs⁻¹. ^b Ref 66. ^c Irreversible, peak potential. ^d Ref 57. ^e Ref 45. ^f Ref 67. ^g Ref 68. ^{h,i} Ref 69.

1.7 Goal of thesis

The primary goal of this thesis is to gain a better understanding of the redox reactions that occur in tetraorganodiphosphines, and certain other phosphorus and arsenic-containing compounds, using a variety of electrochemical and spectroscopic techniques supplemented, as needed, by DFT calculations. Comparisons to known related compounds to find the best explanation for observed patterns are described.

As the thesis research progressed, some unusual effects for the EPR spectra in both the solid and liquid phases were encountered, which required considerable effort to understand. At this point, using DFT calculations (calculated hyperfine splitting constants) helped to interpret the results from EPR. This thesis will discuss some interesting examples illustrating many of the fundamental concepts involved in solid phase EPR spectra, some of which have never been fully addressed in the literature.

A major achievement of this thesis was the synthesis of a new tetraorganodiphosphine with interesting properties and its full characterization by X-ray crystallography, NMR spectroscopy and electrochemistry. The thesis is rounded out by including electrochemical investigations of non-published compounds completing the series of triarylphosphorus compounds which have been made in recent years in the Boéré lab.

References

1. Maier, L. *Progr. Inorg. Chem.* **1963**, 5, 27.
2. Paddock, N. L., *Lectures, Monographs, Rept., No. 2*. Roy. Inst. Chem: London, 1962.
3. Sasse, K. *Methoden der organischen Chemie.* **1963**, 12, 182.
4. Cowley, A. H. *Chem. Rev.* **1965**, 65, 617.
5. Goldwhite, H.; Kaminski, J.; Millhauser, G.; Ortiz, J.; Vargas, M.; Vertal, L.; Lappert, M. F.; Smith, S. J. *J. Org. Chem.* **1986**, 310, 21.
6. Kuchen, W.; Buchwald, H. *Chem. Ber.* **1959**, 227.
7. Böhm, V. P. W.; Brookhart, M. *Angew. Chem. Int. Ed. Engl.* **2001**, 40, 4694.
8. Dorken, C., *Ber.* **1888**, 21, 1505.
9. Gynane, M. J. S.; Hudson, A.; Lappert, M. F.; Power, P. P.; Goldwhite, H. *J. Chem. Soc., Chem. Commun.* **1976**, 623.
10. Burg, A. B., *J. Am. Chem.* **1961**, 83, 2226.
11. Henderson, W. A.; Epstein, M.; Seichter, F. S. *J. Am. Chem. Soc.* **1963**, 85, 2462.
12. Stepanov, B. I.; Karpova, E. N.; Bokanova, Z. A. *Obshch. Khim.* **1969**, 39, 1544.
13. Niebergall, H.; Langenfeld, B. U. S. Patent 2. 959, 1960.
14. Niebergall, H.; Langenfeld, B. *Chem. Ber.* **1962**, 95, 64.
15. Noth, H.; Vetter, H. J. *Chem. Ber.* **1961**, 94, 1505.
16. Vetter, H. J.; Noth, H. *Chem. Ber.* **1963**, 96, 1816.
17. Issleib, K.; Seidel, W. *Chem. Ber.* **1959**, 92, 2681.
18. Seidel, W.; Issleib, K. *Anorg. Allgem. Chem.* **1963**, 325, 113.
19. Schumann, H.; Kopf, H.; Schmidt, M. *Chem. Ber.* **1964**, 97, 1458.
20. Sandoval, A. A.; Moser, H. C.; Kiser, R. W. *J. Phys. Chem.* **1963**, 67, 124.
21. Issleib, K.; Krech, K. *Chem. Ber.* **1965**, 98, 1093.
22. Carty, A. J.; Johnson, D. K.; Jacobson, S. E. *J. Am. Chem. Soc.* **1979**, 101, 5612.
23. Mundt, O.; Riffel, H.; Becker, G.; Simon, Z. A. *Naturforsch. Teil.* **1988**, 43, 952.

24. Richter, R.; Kaiser, J.; Sieler, J. *Acta Crystallogr. Sect., B*. **1977**, *33*, 1887.
25. Baxter, S. G.; Cowley, A. H.; Davis, R. E.; Riley, P. E. *J. Am. Chem. Soc.* **1981**, *103*, 1699.
26. Seidel, W.; Issleib, K. *Anorg. Allgem. Chem.* **1963**, *325*, 113.
27. Bennett, F. W.; EmelBus, H. J.; Haszeldine, R. N. *J. Chem. Soc.* **195**, 3896.
28. Becke, A. D. *J. Chem. Phys.* **1993**, *98*, 5648.
29. Brady, F. J.; Cardin, C. J.; Cardin, D. J.; Wilcock, D. J. *Inorg. Chim. Acta.* **2000**, *298*, 8.
30. Dodds, D. L.; Haddow, M. F.; Orpen, A. G.; Pringle, P. G.; Woodward, G. *Organometallics.* **2006**, *25*, 5937.
31. Hinchley, S. L.; Robertson, H. E.; Borisenko, K. B.; Turner, A. R.; Johnston, B. F.; Rankin, D. W. H.; Ahmadian, M.; Jones, J. N.; Cowley, A. H. *Dalton Trans.* **2004**, 2469.
32. Hinchley, S. L.; Morrison, C. A.; Rankin, D. W. H.; Macdonald, C. L. B.; Wiacek, R. J.; Cowley, A. H.; Lappert, M. F.; Gundersen, G.; Clyburne, J. A. C.; Power, P. P. *Chem. Commun.* **2000**, *20*, 2045.
33. Hinchley, S. L.; Morrison, C. A.; Rankin, D. W. H.; Macdonald, C. L. B.; Wiacek, R. J.; Voigt, A.; Cowley, A. H.; Lappert, M. F.; Gundersen, G.; Clyburne, J. A. C.; Power, P. P. *J. Am. Chem. Soc.* **2001**, *123*, 9045 - 9053
34. Symons, M. C. R.; Tordo, P.; Wyatt, J. *J. Org. Chem.* **1993**, *443*, C29.
35. Sasaki, S.; Murakami, M.; Murakami, F.; Yoshifuji, M. *Heteroatom Chem.* **2011**, *22* , 506.
36. Ayant, Y.; Kernevez, N.; Thevand, A.; Werbelow, L. G.; Culcasi, M.; Gronchi, G.; Tordo, P. *J. Magn. Reson.* **1986**, *70*, 446.
37. Culcasi, M.; Gronchi, G.; Tordo, P. *J. Am. Chem. Soc.* **1985**, *107*, 7191.
38. Culcasi, M.; Berchadsky, Y.; Gronchi, G.; Tordo, P. *J. Org. Chem. Ing. Tech.* **1991**, *56*, 3537.
39. Nelsen, S. F. *Act. Chem. Res.* **1981**, *14*, 131.
40. Nelsen, S. F.; Blackstock, S. C.; Yumibe, M. P.; Frifo, T. B.; Carpenter, J. E.; Weinhold, F. *J. Am. Chem. Soc.* **1985**, *107*, 143.
41. Culcasi, M.; Berchadsky, Y.; Gronchi, G.; Tordo, P. *J. Org. Chem. Ing. Tech.* **1991**, *56*, 3537.

42. Stockland, R. A.; Kohler, M. C.; Guzei, I. A. ; Kastner, J. M. E.; Bawiec, A. ; Labaree, D. C.; Hochberg, R. B. *Organometallics*. **2006**, *25*, 2475.
43. Zagumennov, V. A.; Nikitin, E.V.; *Russ. J. Electrochem.* **2003**, *39*, 1236.
44. Alyea, E. C.; Ferguson, G.; Gallagher, J. F.; Malito, J. *Acta Crystallogr. Sect. C*. **1993**, *49*, 1473.
45. Sasaki, S.; Yoshifuji, M. *Curr. Org. Chem.* **2007**, *38*, 17.
46. Oshikawa, T.; Yamashita, M. *Chem. Ind.* **1985**, 126.
47. Goldwhite, H.; Kaminski, J.; Millhauser, G.; Ortiz, J.; Vargas, M.; Vertal, L.; Lappert, M. F.; Smith, S. J. *J. Org. Chem.* **1986**, *310*, 21.
48. Davies, W. C. *J. Chem. Soc.* **1935**, 462.
49. Yoshifuji, M.; Shibayama, K.; Inamoto, N.; Matsushita, T.; Nishimoto, K. *J. Am. Chem. Soc.* **1983**, *105*, 2495.
50. Nief, F.; Mathey, F. *Tetrahedron Lett.* **1991**, *47*, 6673.
51. Schmidbaur, H.; Schnatterer, S., *Chem. Ber.* **1983**, *116*, 1947.
52. Sasaki, S.; Murakami, F.; Yoshifuji, M., *Tetrahedron Lett.* **1997**, *38*, 7095.
53. Sasaki, S.; Murakami, F.; Yoshifuji, M. *Organometallics*. **2006**, *25*, 140.
54. Boéré, R. T.; Bond, A. M.; Cronin, S.; Duffy, N. W.; Hazendonk, P.; Masuda, J. D.; Pollard, K.; Roemmele, T. L.; Tran, P.; Zhang, Y. *New J. Chem.* **2008**, *32*, 214.
55. Aranyos, A.; Old, D. W.; Kiyomori, A.; Wolfe, J. P.; Dadighi, J. P.; Buchwald, S. L. *J. Am. Chem. Soc.* **1999**, *121*, 4369.
56. Greenfield.S. J.; Gilbertson.S. R. *Synthesis (Stuttgart)*. **2001**, 2337.
57. Blount, J. F.; Maryanoff, C. A.; Mislou, K. *Tetrahedron Lett.* **1975**, *48*, 913.
58. Greenwood, N. N.; Earnshaw, A. *Chemistry of the Elements, Butterworth-Heinemann*. 2nd ed.; Oxford: 1997; p 493.
59. Boéré, R. T.; Zhang, Y. *J. Organomet. Chem.* **2005**, *690*, 2651.
60. Stojanovic, R. S.; Bond, A. M. *Anal. Chem.* **1993**, *65*, 56.
61. Sasaki, S.; Sutoh, K.; Murakami, F.; Yoshifuji, M. *J. Am. Chem. Soc.* **2002**, *124*, 14830.
62. Wesemann, J.; Jones, P. G.; Schomburg, D.; Heuer, L.; Schmutzler, R., *Chem. Ber.* **1992**, *125*, 2187.

63. Mingos, D. M. P.; Müller, T. E. *J. Organomet. Chem.* **1995**, *500*, 251.
64. Müller, T. E.; Green, J. C.; Mingos, D. M. P.; McPartlin, C. M.; Whittingham, C.; Williams, D. J.; Woodroffe, T. M. *J. Organomet. Chem.* **1998**, *551*, 313.
65. Sasaki, S.; Sutoh, K.; Murakami, F.; Yoshifuji, M. *J. Am. Chem. Soc.* **2002**, *124*, 14830.
66. Daly, J. J. *J. Chem. Soc.* **1964**, 3799.
67. Tayim, H. A.; Ahmed, J.; Horne, W. *J. Crystallogr. Spectrosc.* **1985**, *15*, 561.
68. Sobolev, A. N.; Romm, I. P.; Chernikova, N. Y.; Belsky, V. K.; Guryanova, E. N. *J. Organomet. Chem.* **1981**, *219*, 35.
69. Sobolev, A. N.; Romm, I. P.; Belsky, V. K.; Guryanova, E. N. *J. Organomet. Chem.* **1979**, *179*, 153.

Chapter 2

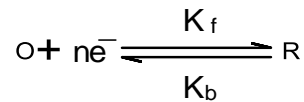
Methodology

2.1 Introduction to electroanalytical techniques

This summary is derived from the treatment presented in Bond, A. M., *Broadening electrochemical horizons: Principles and illustration of voltammetric and related techniques*, Oxford: Oxford University Press, 2002 and also draws on the treatment found in J. Wang, *Analytical electrochemistry*, 3rd edition (New York: Wiley-VCH, 2006). The measurement of electrical quantities such as current, potential, or charge and their relationship to chemical parameters is known, collectively, as electrochemistry. Within electrochemistry, electroanalytical techniques refer to the specific application to identification and measurement of chemical species using electrochemical methods. Since the mid 1980's, the popularity of electroanalytical techniques has increased through applications to environmental monitoring, industrial quality control, and biomedical analysis. A key difference between electrochemical measurements and chemical measurements is that most chemical techniques involve homogeneous bulk solutions while electrochemical studies take place at the electrode-solution interface.¹ In this thesis, main focus amongst all of the electrochemical techniques will be on controlled potential techniques. The advantages of controlled-potential techniques include high sensitivity and selectivity toward electroactive species, a wide linear range, portable and low-cost instrumentation, speciation capability, and a wide range of types of electrodes. The main objective in controlled-potential (potentiostatic) techniques is the study of charge transfer processes at the electrode-solution interface and thus is based on dynamic (non-zero-current) situations. In these methods, the

electrode potential leads to an electron transfer reaction and subsequently the resultant current will be the measured quantity (and hence the dependent variable).

The three most important pieces of information which can be obtained by these techniques are: (1) E° for the (half) cell reaction (which is called the electrode potential), (2) rates of the forward and/or backward reactions, and/or (3) concentration of the target analyte C_O and/or C_R . Such an objective is accomplished by monitoring the transfer of electron(s) during the redox process of the analyte:



Where O and R are the oxidized and reduced forms, respectively, of the redox couple. Such a reaction will occur in a potential region that makes the electron transfer thermodynamically or kinetically favorable. According to the Nernst equation (Eq.1)² (where E° is the standard potential for the redox half-reaction, R is the universal gas constant ($8.314 \text{ J}\cdot\text{K}\cdot\text{mol}^{-1}$), T is the Kelvin temperature, n is the number of electrons transferred in the reaction, and F is the Faraday constant [$96.487 \text{ C}\cdot\text{mol}^{-1}$], useful information about the relation between the potential of the electrode and concentration of the electroactive species at the surface can be obtained.

$$E = E^\circ + \frac{RT}{nF} \ln \frac{C_O(0,t)}{C_R(0,t)} \quad \text{Eq.1}$$

The results are recorded on a current-potential plot, known as a voltammogram, which is a display of current signal [vertical axis] versus the excitation potential [horizontal axis].

2.1.1 Voltammetry

Voltammetry is an interesting technique for electrochemists since it has found a wide range of applications such as quantitative measurements of species of interest, whether in

biological systems (for example, brain electrochemistry is important in neuroscience) or for environmental monitoring, in battery technology, the development of fuel cells and solar energy conversion. The main goal in this project to use voltammetry is to characterize electrochemical redox reactions in desired compounds. Two major classes of voltammetry are transient voltammetry and steady-state voltammetry. Transient voltammetric experiments include DC linear sweep, DC cyclic, square-wave, pulsed, and AC voltammetries and in these techniques, the resulting current response will be obtained as a function of potential. If the DC potential is swept in one direction only, the technique is known as linear sweep and if it is swept in one direction and then reversed back to the origin, the technique is known as cyclic voltammetry. The important parameter is the rate at which the potential is ramped dE/dt , which is known as the scan rate, v .

In contrast to transient methods, steady-state voltammetric experiments are conducted under conditions that are sufficiently close to the true steady-state. The effective time-scale of a near steady-state process can be obtained by the rate at which material reaches the electrode surface. This time-scale may be varied in a number of ways:

- (1) Hydrodynamic techniques which implies altering the convective rate of transport, for example, by changing the rotation frequency of a rotated disk electrode (RDE).
- (2) Increasing the ratio of radial to linear diffusion of material to the electrode surface by significantly decreasing the size of the electrode.

2.1.2 Cyclic voltammetry

Cyclic voltammetry is the technique at which the DC potential at the working electrode is usually swept at a constant scan rate (v) from an initial potential value of E_1 to a second potential E_2 and then the sweep is reversed upon reaching E_2 .³ The scan rate may range from a few millivolts per second to a million volts per second. The value of the lower scan rate is limited by

the effect of natural convection like mechanical vibration. Natural convection causes an unwanted increase in the rate of mass transport to the electrode surface and thus leads the experiment to deviate from the diffusion-only regime. In addition, capacitive charging restricts the upper scan rate limit. In cyclic voltammetric experiments and in the presence of excess electrolyte, ideally, the sole form of mass transport to the electrode surface is diffusion, and in the case of large macrodisc (millimeter dimensions) electrodes, the diffusion of material to the electrode occurs in the single dimension perpendicular to the electrode surface. The ideal cyclic voltammogram shown in Figure 2.1 for a reversible one-electron oxidation process, in theory, encompasses a region starting from where no electrode reactions take place to where one or more reactions take place. The resulting voltammogram is usually displayed in an asymmetrical voltammetric wave shape showing the current dependence as a function of the potential difference applied between the working and reference electrodes. Investigation of the stability of the product formed via heterogeneous redox reactions, as well as detection of any new electroactive products formed because of their decomposition has been studied by repeating the potential sweep cycles multiple times. The most important information gained from CV voltammograms is the magnitude of the cathodic (I_p^c) and anodic (I_p^a) peak currents, and the cathodic (E_p^c) and anodic (E_p^a) peak potentials (Figure 1.1b). The midpoint, E_m , or half-wave potential, $E_{1/2}$, is related to the peak potentials by the following expression (Eq.2):

$$E_m = E_{1/2} = E_p^{oxi} + E_p^{red}/2 \quad \text{Eq.2}$$

The peak currents, I_p^{ox} and I_p^{red} , respectively (note again the *base lines* from which they are measured in Figure 2.1); for a reversible process are given by the Randles–Sevcik equation (Eq.3):

$$I_p^{oxi} = I_p^{red} = 0.4463nF \left(\frac{nF}{RT}\right)^{1/2} AD_A^{1/2} \nu^{1/2} C_A \quad \text{Eq.3}$$

Where C_A or $[A]_{x=0}$ is the concentration of A in the bulk solution (in mol/cm³), n is the number of electrons, A the electrode area (in cm²), D_A the diffusion coefficient of ferrocene (in cm²/s), and ν the potential scan rate (in V/s), so that the magnitude of the ratio $|I_p^{ox}/I_p^{red}|$ is unity.

There are two known distinct sign convention for voltammograms, one in which positive current flows as the potential is swept in the cathodic direction (sometimes referred to as the "American" or polarographic convention), and one in which negative current flows as the potential is swept in the cathodic direction (also called the "European" convention but now more commonly known as the IUPAC convention since the International Union of Pure and Applied Chemistry has officially adopted it). For the purposes of all discussions in this category I have chosen to display all relevant figures using the IUPAC convention.⁴

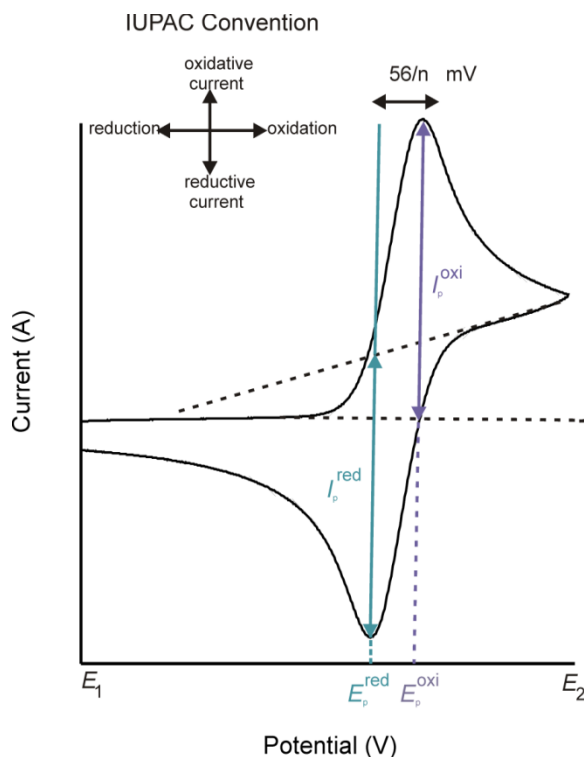
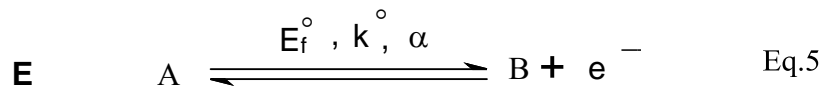


Figure 2.1. Cyclic voltammogram obtained for a reversible one-electron reduction process at 25 °C using the IUPAC sign convention

It is common to observe homogeneous chemical reactions, which accompany the electron-transfer step in CV experiments. This means that an electrochemical reaction mechanism may consist of a combination of heterogeneous electron transfer (E) and homogeneous chemical (C) reaction steps, each with their own individual rate constants. For example, if the product B of Eq.4 undergoes a first-order, solution-phase chemical reaction with a rate constant k_1 :



Then a complete description of the electrode process when the initial charge-transfer step is reversible is given by:

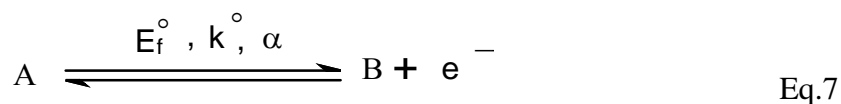


Where E_f° is the formal potential of an electrode (V) and α is the transfer coefficient. This frequently observed reaction scheme is commonly named as an **EC** or $E_{\text{rev}}C_{\text{irrev}}$ mechanism. Hence, it is possible to construct electrode reaction mechanisms with an infinite number of combinations of E and C steps, with different levels of reversibility being associated with both the E and C components.

One of the most important things to deal with in cyclic voltammetry is to distinguish what is meant by the terms reversible, quasi-reversible and irreversible process, which are used quite frequently and often erroneously in the literature as a means of describing voltammetric results. “Reversibility” can be used to describe what is occurring both electrochemically and chemically subsequent to the initiation of a potential sweep on the working electrode. The extent of electrochemical reversibility of a redox process is related to the heterogeneous kinetics of

electron transfer at the electrode surface. A simple electron-transfer reaction under conditions where electron-transfer is truly fast in both directions is usually called "electrochemically reversible".⁴ This means that both the forward and reverse electron-transfer reaction steps are rapid and the Nernst equation applies for the Eq.7. This is due to the fact that the electron-transfer kinetics for the forward and reverse processes is so facile that equilibrium is attained at each potential applied on the time-scale of the particular experiment. However, the criterion for electrochemical reversibility is a practical rather than absolute one, and is dependent upon the time-scale of the electrochemical measurement. This means that a process may be electrochemically reversible under certain conditions (i.e., CV with a slow scan rate), but irreversible under other conditions (i.e., hydrodynamic voltammetry with a fast rotation rate).

The term "chemical reversibility" is associated with the stability of the electroactive species involved in the electron-transfer step. Therefore, if in:



Species B irreversibly reacts to form species C, as in Eq. 6, then the overall process ($A \rightarrow C$) would be described as being chemically irreversible. However, if the chemical step associated with the chemical reaction step of B were sufficiently fast, in both the forward and backward directions, so that equilibrium is effectively maintained on the time-scale of the voltammetric experiment, then the whole process would be termed chemically reversible.

The term "irreversible" is commonly used when the electron-transfer kinetics are slow (rate-determining) relative to mass transport, the electrode process is no longer in equilibrium and therefore does not obey the Nernst equation. In this case, k_b for the backward reaction can be neglected.

Finally, if both reversible and irreversible categories of process may exist, then there must be intermediate cases in which the kinetics of both the forward and reverse electron-transfer processes needs to be considered. Both k_f and k_b (forward and backward electron-transfer rate constants) must be considered in solving the theory and such systems are described as being quasi-reversible and, as would be expected for this category of electrode process, the scan rate can have a considerable effect on the nature of the observed cyclic voltammogram. At sufficiently slow scan rates, quasi-reversible processes appear to be fully reversible. However, as the scan rate is increased, the kinetics of the electron transfer is not fast enough to follow the Nernst equation. It is crucial to use these terms correctly, which are often used inappropriately in the chemical literature, most commonly when authors claim that systems displaying any sort of return wave are "reversible." Reversibility must, in fact, always be quoted with respect to the specific context of the experiments and specify whether chemical or electrochemical reversibility is being ascribed.

2.1.3 Cyclic voltammetry experimental equipment

A typical experimental arrangement used for standard voltammetric experiments contains three electrodes: working, reference and auxiliary are present in close proximity, with the working electrode in the center (Figure 2.2). All three are immersed in a solution containing the analyte and electrolyte. One of the important concerns during voltammetry experiments is to minimize contributions of the IR_U drop ($I =$ current, $R_u =$ uncompensated resistance) to the applied potential. The cell also contains an inlet and outlet for an inert gas to remove electroactive oxygen from the solution. This is especially important in all cases where at least one component of the redox pair is oxygen sensitive, which is by far the most common situation; it is in fact rare that both partners in the couple will be stable to O_2 , especially where one is a free

radical as a result of a one-electron transfer. Typical inert gases include high purity nitrogen and argon. The solution volume is typically in the range of 5–20 mL. The concentration of the electroactive species (analyte) of interest when employing DC voltammetric techniques is typically in the range 0.1-5 mM. A high concentration of supporting electrolyte ($>0.1\text{M}$) is usually added to the solution to minimize the solution resistance and to reduce transport of electroactive ions by migration. The supporting electrolyte should be pure and hard to oxidize and reduce.³

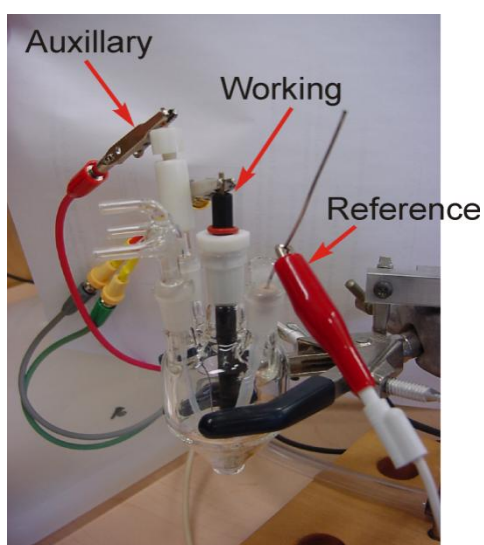


Figure 2.2. Standard cell design employed for CV studies showing the electrical connectors to the working, auxiliary and reference electrodes.³

The working electrode has a potential which is varied linearly with time and will be measured during the course of the experiment, and is the electrode at which the reaction of interest is occurring. Working electrodes are constructed from electrically conducting materials. Common examples include liquid mercury, solid platinum or gold and some forms of carbon (e.g. glassy carbon (GC) or graphite). Typically, the solid electrode materials are sealed into a non-conducting support (e.g. glass or Teflon) to form a disc electrode. Macrodisc electrodes have radii in the mm range, whereas microdisc electrodes have radii in the nm to μm range. The most

common systems contain a large diameter flat electrode surface embedded in an insulating material of significantly larger radius than the conducting material, which helps ensure that the solution behavior approximates to linear diffusion. The reference electrode has a potential that is supposed to remain constant throughout the experiment and Ag or Pt wire are frequently used for experiments. In voltammetric studies in organic solvents, it is now common practice to measure the reversible potential for the oxidation of ferrocene (Fc), to the ferricinium cation (Fc^+), versus the reference electrode and subsequently correct potentials to the Fc/ Fc^+ scale.^{5,6} The counter electrode usually consists of a piece of platinum (wire or gauze) or carbon (disc or rod) of large surface area placed directly into the solution and serves to conduct current from the source through the solution to the working electrode. The potential of the auxiliary electrode is opposite in sign to that of the working electrode, but its current and potential are not measured. The auxiliary electrode often has a surface area much larger than that of the working electrode to ensure that the reactions occurring on the working electrode are not surface-area-limited by the auxiliary electrode. The current measured in a voltammetric experiment flows between the working and counter electrode. Thus, if a reduction reaction is occurred at the working electrode a balancing oxidation process must occur at the counter electrode or vice versa.

2.1.4 Rotated-disk voltammetry (RDE)

When convection is a dominant form of mass transport, techniques are classified under the heading hydrodynamic voltammetry at which electroactive material reaches the electrode via diffusion and convection. This requires, of course, the usual presence of supporting electrolyte in 100-fold excess. One of the major advantages of hydrodynamic voltammetric methods is associated with the current achieving a steady-state during the experiment. Therefore, due to the typically low scan rates and steady-state conditions employed, capacitive charging presents a

relatively small effect in hydrodynamic techniques. The potential profile of hydrodynamic techniques usually takes the form of a linear or staircase sweep over the potential range in which the oxidation or reduction processes of interest occur. There are a number of hydrodynamic techniques in use but in this project only use of rotated-disk voltammetry has been considered. The RDE method is often the most reliable way to determine the value of “ n ” for the reaction (number of electrons transferred) and the value of the diffusion coefficient (D).

The rotated-disk, or RDE, consists of a disc electrode made from a suitable working electrode material (i.e. glassy carbon or platinum), surrounded by a non-conducting region that extends the disc to a larger diameter; the whole is polished to a smooth face. The RDE faces downwards into solution and is rotated around an axis perpendicular to and through the centre of the disk. Under these conditions, a well-defined flow pattern is established. In effect, solution is sucked towards the electrode from below and then flung outwards (Figure 2.3).

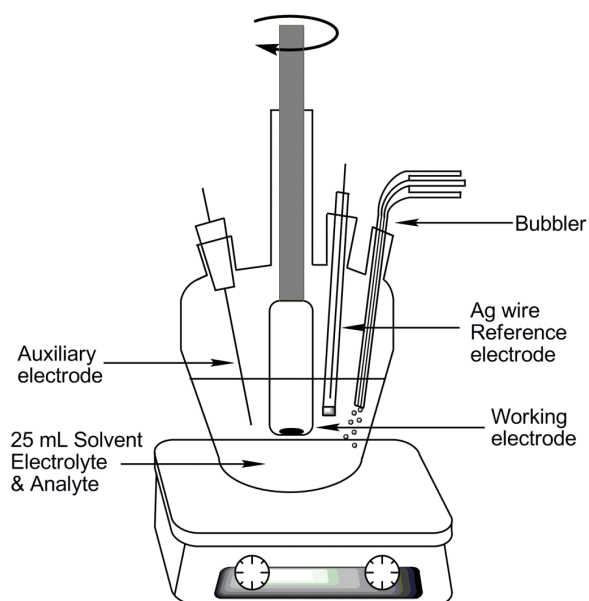


Figure 2.3. Rotated-disk electrode setup

The rotation rate is in the range of 4-65 Hz (200-4000 rpm). The crucial parameter which controls the time-scale over which electrode reactions are examined at a RDE is the electrode angular velocity, ω (rad s⁻¹), which is related to the rotation frequency, f (Hz), by $\omega = 2\pi f$ or by $\omega = 0.1047 \times (\text{rate}_{\text{rpm}})$ for those instruments where the rotor is calibrated in revolutions per minute (rpm).³ In RDE experiments, we measure the limiting current (or mass-transport-limited current) I_{ℓ} , measured at sufficiently positive potentials that the mass-transport process associated with an oxidation process is rendered rate-determining. This means that there is a sufficiently high chemical potential that the rate of the electron transfer reaction will always be fast compared to mass transfer. This current, for a process of the kind $A \rightarrow B + ne^{-}$ for a reversible system, reaches a maximum at a given rate of mass transport, and is thus proportional to the square root of the angular velocity which controls mass transfer via the hydrodynamic process and is described by the Levich equation (Eq.8):²

$$I_{\ell} = 0.620nFA C^{\circ} D^{2/3} \nu^{-1/6} \omega^{1/2} \quad \text{Eq.8}$$

Here, C° = bulk solution concentration, mol cm⁻³; I_{ℓ} = limiting current, A; D is the diffusion coefficient of species A, cm² s⁻¹; ν = kinematic viscosity of the fluid, cm² s⁻¹; ω = angular disk velocity of the disk, rad s⁻¹. Kinematic viscosity is defined as the viscosity of the solution divided by the density in cm² s⁻¹ but in practice, the viscosity of the pure solvent is often used rather than obtaining viscosity measurements on the actual solvent/analyte/electrolyte mixture.

2.2 Electron paramagnetic resonance spectroscopy (EPR)

Electron paramagnetic resonance (EPR) spectroscopy,⁷ also known as electron spin resonance (ESR), electron magnetic resonance (EMR), or simply paramagnetic resonance (PR) spectroscopy was invented by the Russian physicist Zavoisky⁸ in 1945. It is a technique, which detects characteristic signals emanating from compounds containing one or more unpaired

electrons. The electron paramagnetic resonance spectrum of a free radical or coordination complex with one unpaired electron is the simplest of all forms of spectroscopy. The degeneracy of the electron spin states characterized by the quantum number, $M_s = \pm 1/2$, is lifted by the application of a magnetic field, and transitions between the spin levels are induced by radiation of the appropriate frequency. EPR is used to effectively map the distribution of the unpaired electron(s) and hence determine the extent to which it is delocalized over the molecule. This type of spectroscopy occurs in the microwave frequency range due to a larger energy gap than that for nuclear magnetic resonance (NMR) at similar magnetic field strengths. EPR and NMR are similar in the fact that they both involve electromagnetic radiation interacting with a sample of matter contained in a homogenous magnetic field. With NMR, the origin of the signal coming from the sample is magnetic (non-zero spin) atomic nuclei, whereas with EPR it is the unpaired electron. Detection of paramagnetic species can be accomplished with concentrations as low as $10^{-8} \text{ mol L}^{-1}$.

When an electron is placed in a magnetic field the degeneracy of the electron spin energy levels is lifted and is described by the following spin Hamiltonian (Eq.9):

$$\hat{H}_s = g\mu_B B \hat{S}_z \quad \text{Eq.9}$$

Where \hat{H}_s is the spin Hamiltonian, g is the Landé splitting energy or the “ g value,” (or g -factor), ($g_e = 2.00232$ for a free electron), μ_B is the Bohr magneton ($9.274 \times 10^{-28} \text{ J G}^{-1}$), and \hat{S}_z is the z -component of the electron spin angular momentum operator. The magnetic induction parameter \mathbf{B} is the magnetic field strength. The magnetic field is given in Tesla (T) in the S.I. system of units used in this thesis. However, much of the literature to this day uses Gauss (which comes from the old CGS units system). The splitting of the energy levels is also known as the Zeeman effect. Applying a magnetic field to the unpaired electron results in two different spin

orientations along the field's direction, and the electron spin energy levels are found by application of \hat{H}_s to the electron spin eigenfunctions corresponding to the quantum number, $M_S = \pm 1/2$ (Eq.10):

$$E_{\pm} = \pm \left(\frac{1}{2}\right) g\mu_B B \quad \text{Eq.10}$$

The difference in energy between these two levels is given by Eq.11:

$$\Delta E = g\mu_B B = h\nu \quad \text{Eq.11}$$

and corresponds to the energy, $h\nu$ of a photon required to cause a transition from one energy level to the other. The Zeeman splitting is indicated by ΔE , and as indicated is controlled by the quantum number M_S . If the applied magnetic field has the only interaction with the electron then all useful information which could be obtained about the sample, would be limited to one line and the g value (Figure 2.4(a)).⁹

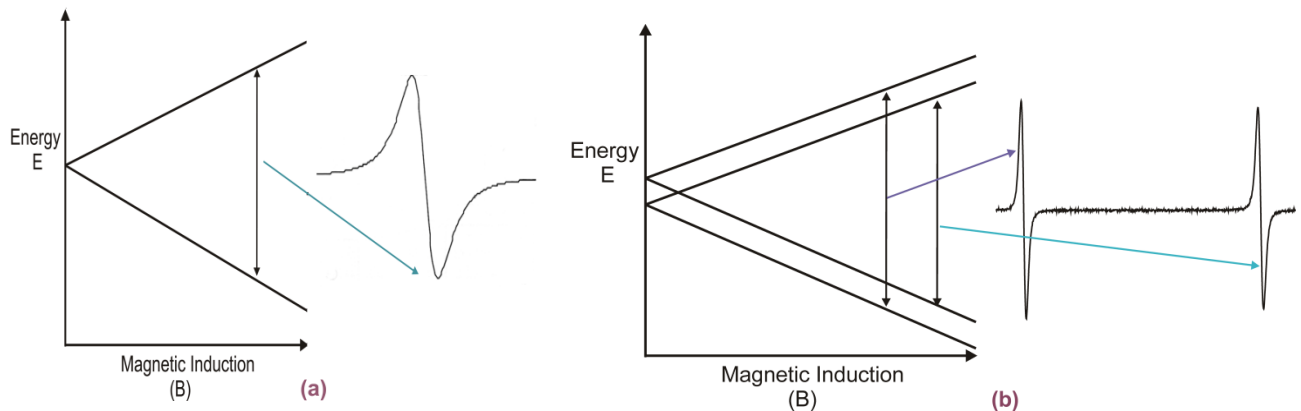


Figure 2.4. (a) Energy levels of an electron placed in a magnetic field. (b) Energy levels of an unpaired electron in a magnetic field interacting with a spin-1/2 nucleus

However, if magnetic nuclei that are in close proximity and that have a spin quantum number $I > 0$ interact with the unpaired electron then there is another perturbation of the electron energy and an additional term appears in the spin Hamiltonian (Eq.12):(Figure 2.4(b))

$$\hat{H}_s = g\mu_B B \hat{S}_z + \sum_i A_i \hat{I}_i \cdot \hat{S}_i \quad \text{Eq.12}$$

where A_i is the hyperfine coupling constant (which is an energy term, but the energies are typically very small and so wave number units $\{\text{cm}^{-1}\}$ are commonly used), where I is the nuclear spin quantum number. Therefore, the spectral information can lead to two types of chemically useful information (Figure 2.4(b)). One is the hyperfine splitting constant (HFS), a_i , which is related to A_i by $a_i = A_i/g\mu_B$ and which has values (in magnetic field units) which are determined by the line separations in the spectra ("i" is the isotope being interrogated). Values for a_i provide information on the number and kinds of magnetic nuclei with which interacts with unpaired electron. The other is the g value, which is found at the center of gravity of the spectrum. The g value for a free electron is 2.0023, and can be used for comparison between the magnetic environments of measured spectra versus that of the free electron (i.e., it is a measure of the influence of the electronic environment on the spin of the free electron, and somewhat analogous to a chemical shift in NMR spectroscopy). In isotropic spectra (where free re-orientational motion is present), the observed parameters are averaged by the rotation of the molecules. In anisotropic spectra (solids), the orientation of the nuclei are fixed (and therefore their dipole moments are also fixed), such that each orientation leads to a different kind of magnetic resonance interaction and the observed parameters will depend on the molecular orientation relative to the magnetic induction, B .

The detected AC signal (lines or bands) is proportional to the change in sample absorption as the field is swept. Spectra are traditionally recorded as the first derivative of the absorption curve (called the dispersion signal) (Figure 2.5).⁷ First-derivative spectra have much better apparent resolution than adsorption spectra and therefore are easier to interpret. Indeed, second-derivative spectra are even better resolved (though the signal-to-noise ratio decreases).

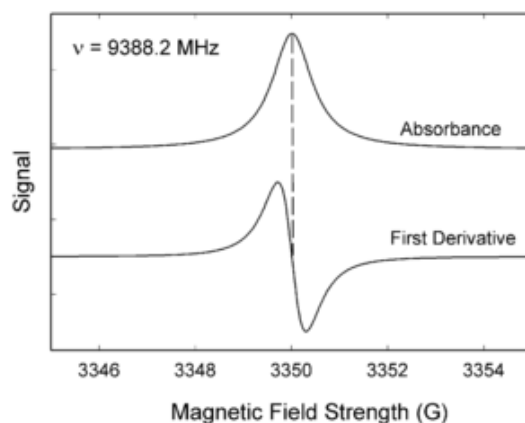


Figure 2.5. Small-amplitude field modulation detects the signal as a dispersion signal. Its relation to the absorption curve is that of a first derivative

From the EPR selection rules, it can be shown that each number N of magnetically equivalent nuclei of spin I splits the electron spin levels into $2NI + 1$. The unpaired electron can interact with any nuclei for which $I > 0$, and spectra resulting from coupling to quadrupolar nuclei are routinely observed, unlike the situation in NMR spectroscopy where observable coupling to quadrupolar nuclei is extremely rare.

2.3 EPR spectroelectrochemistry

The term spectroelectrochemistry¹⁰ applies to the spectroscopic study of electrode surfaces and the electrode-surface interface. The combined application of techniques such as infrared, ultraviolet/visible, and electron paramagnetic resonance spectroscopy with electrochemistry have played key roles in the detection and identification of intermediates or products generated from redox reactions, which are difficult to identify with certainty from an interpretation of the electrochemical response of the system alone. In addition, since the vast majority of electron-transfer reactions involve (sequential) one-electron transfers, techniques that detect free-radicals are especially relevant to spectroelectrochemistry. EPR-electrochemical

experiments can be classified into two broad categories. The first, called "external generation", involves electrolysis outside the EPR cavity, transfer of the radicals to the cavity, and observation of the EPR spectrum. The second classification is called "internal", "in situ", or "intra muros" generation. It involves placement of a working electrode directly inside the EPR cavity and permits recording the EPR signal. This method requires a cell design that covers both the electrochemical and EPR performance of the cell.

2.3.1 Simultaneous electrochemical electron paramagnetic resonance (SEEPR)

Because of the difficulties including a current-resistance (iR) drop along the length of the solution, uncompensated solution resistance, and imprecise control of the potential of the working electrode due to inadequate reference electrode placement, electroanalytical studies are usually performed separately from radical generation studies. However, a few designs have appeared which permit the monitoring of both the electrochemical and EPR response of a free-radical system. This is commonly referred to as simultaneous electrochemical electron paramagnetic resonance, or SEEPR. In one of the earliest in situ EPR electrochemical flat cells designed by Bard,^{11,12} the desired electrochemical response was achieved through the use of a thin flat cell containing two tungsten rods serving as the auxiliary electrode and placed parallel along the edges of the cell. The working electrode is a platinum wire mesh and the reference electrode is a silver wire both coated in Teflon. This design allows for the execution of CV measurements within the EPR cavity simultaneous with the recording of the EPR signal intensity. It also allows for the study of the decomposition of the electrolytically generated radicals. Work in our own lab has focused on a convenient electrode design (Figure 2.6) pioneered by Neudeck and Kress¹³ and further developed by Dr. Tracey Roemmele. This design

makes use of a gold-micromesh working electrode with a large surface area to maximize the EPR signal intensity.

Useful features of the gold micro-mesh (density of 1500 wires/inch) include that it is commercially available and optically transparent to allow for simultaneous EPR or UV-vis spectroelectrochemistry experiments. This electrode material is fragile but by laminating the mesh together with a thin copper wire which extends out of the cell cavity, it can be stabilized and insulated.



Figure 2.6. Low-temperature EPR flat cell developed by Boéré and Roemmele

The reference electrode is a silver wire with a Teflon coating placed in close proximity to the working electrode. This particular design gives high sensitivity and retains good performance for voltammetry which not only allows for the simultaneous recording of undistorted CV measurements, but also allows for the generation of sufficient amounts of radical material such

that single EPR scans result in signals with high signal-to-noise ratios. Several other cell designs currently exist, and a list of references is given for the interested reader.^{14, 15, 16}

2.4 Density functional theory

2.4.1 Introduction

This section is derived from the treatment presented mostly in references 18 and 19 and the Hyperchem¹⁷ users manual section. The quantum mechanical methods which are commonly used as a tool by chemists include semi-empirical, *ab initio*, and density functional theory. The semi-empirical quantum mechanical methods (as well as classical molecular mechanics) have several advantages over *ab initio* and density functional methods. Most importantly, these methods are fast. A disadvantage of these methods is that they must have parameters available before running a calculation. Developing parameters is time-consuming. The *ab initio* or density functional methods may overcome this problem. *Ab initio* quantum mechanical methods have evolved for many decades. The speed and accuracy of *ab initio* calculations have been greatly improved by developing new algorithms and introducing better basis functions. Density functional methods are newer methods that have a lot in common with *ab initio* methods. In principle, DFT may be more accurate than *ab initio* Hartree-Fock calculations.

Density Functional Theory (DFT)¹⁷ is an approach to the electronic structure of atoms and molecules which has enjoyed a dramatic surge of interest since the late 1980s and 1990s.¹⁸ Goal in this section is to introduce the key elements of the theory, which has been used as a tool in my studies without going into further details. The premise behind DFT is that the energy of a molecule can be determined from the electron density instead of a wave function. *Ab initio* and DFT methods use the Linear Combination of Atomic Orbitals Molecular Orbital (LCAO-MO)

approximation for all calculations. If Ψ_i represents a molecular orbital and ϕ_μ an atomic orbital, then the LCAO representation of the molecular orbital is

$$\Psi_i = \sum_{\mu} C_{\mu i} \phi_{\mu} \quad \text{Eq.13}$$

Where $C_{\mu i}$ is the coefficient or “weight” of the μ th atomic orbital in the i th molecular orbital. In *ab initio* and DFT calculations, atomic orbitals are functions of the x, y, and z coordinates of the electron that closely resemble the valence orbitals of the isolated atoms. These atomic orbitals are called Slater Type Orbitals (STOs). The complete set of Slater atomic orbitals is called the basis set. Because the calculation of multi-center integrals that are inevitable for *ab initio* and DFT methods is very difficult and time-consuming in view of the functional form of STOs, Gaussian Type Orbitals (GTO) have been used for DFT and *ab initio* HF calculations. However, since atomic orbitals actually have STO functional forms, linear combinations of many GTOs must be used to construct a good approximation to an atomic orbital. Thus, GTO basis sets require many more primitives to describe the wave function than are needed for STO calculations. While STO basis sets are sometimes used for high-accuracy work, most calculations are now done with GTO basis sets because of greatly improved computational efficiency. Choosing a standard GTO basis set means that the wave function is being described by a finite number of functions. This introduces an approximation into the calculation since an infinite number of GTO functions would be needed to describe the wave function exactly. Differences in results due to the quality of one basis set versus another are referred to as basis set effects.

2.4.2 The Hohenberg-Kohn theorem

The formal rationale for Density Functional Theory begins with a remarkable theorem due to Hohenberg and Kohn. This theorem states that the energy E of a molecular system is a

universal functional of the electron density,

$$E=E[\rho] \tag{Eq.14}$$

and that the exact energy is returned only when ρ is exact; approximate ρ 's lead to higher energies. The term functional means that E depends not on simple variables, but on a complicated function, the density in three-dimensional space. That is, E depends on the density only, but with an unknown functional dependence. The term universal dependence means that this dependence of the energy on the density is the same in methane as it is in fluorobenzene and knowing this dependence, it would help provide solutions for all molecular systems.

The Hohenberg-Kohn theorem is not of immediate practical help in solving for the energy and electron density of molecules. The theorem, however, allows a new formulation for a self-consistent-field (SCF) procedure that can be used to compute molecular charge densities. This new procedure is embodied in the Kohn-Sham equations. The Kohn-Sham equations can, in principal, lead to an exact solution for a molecular system. The equations resemble very closely the equations of Hartree-Fock theory. As in Hartree-Fock theory, there are two versions of the Kohn-Sham equations, one for closed-shell systems, analogous to the “restricted” Roothaan equations, and one for open-shell systems, analogous to the “unrestricted” Pople-Nesbet equations. Eq.15 states the generalized “unrestricted” form that is very close to that of UHF equations. The Pople-Nesbet equations of Hartree-Fock theory involve Fock matrices, F^α and F^β that have the following form,

$$F_{\mu\nu}^\alpha = H_{\mu\nu}^\alpha + \sum_{\lambda\sigma} P_{\lambda\sigma}^T (\mu\nu|\lambda\sigma) - P_{\lambda\sigma}^\alpha (\mu\lambda|\nu\sigma) \tag{Eq.15}$$
$$F_{\mu\nu}^{\beta\alpha} = H_{\mu\nu}^{\beta\alpha} + \sum_{\lambda\sigma} P_{\lambda\sigma}^T (\mu\nu|\lambda\sigma) - P_{\lambda\sigma}^\beta (\mu\lambda|\nu\sigma)$$

The first term in the summations above is the Coulomb energy and the second term is the exchange energy. Coulomb interactions occur between all the electrons, independent of spin,

whereas exchange interactions only occur between electrons of parallel spin. In Hartree Fock theory, the correlation energy, the difference between the energy of the Hartree-Fock single determinant wave function approximation and the exact energy is, by definition, zero.

The Kohn-Sham equations or the fundamental equations of pragmatic Density Functional Theory involve replacing the exchange term above with a new exchange-correlation potential and equivalent matrix. That is,

$$F_{\mu\nu}^{\alpha} = H_{\mu\nu}^{\alpha} + \sum_{\lambda\sigma} P_{\lambda\sigma}^T (\mu\nu|\lambda\sigma) + F_{\mu\nu}^{XC\alpha} \quad \text{Eq.16}$$

$$F_{\mu\nu}^{\alpha\beta} = H_{\mu\nu}^{\beta} + \sum_{\lambda\sigma} P_{\lambda\sigma}^T (\mu\nu|\lambda\sigma) + F_{\mu\nu}^{XC\beta}$$

Where F^{XC} is the exchange-correlation matrix (for either alpha or beta electrons) and these two equations constitute the general (unrestricted) matrix form of the Kohn-Sham equations. These equations can be solved in a self-consistent fashion identical to the Pople-Nesbet equations of Hartree-Fock theory, the only difference is the replacement of the Hartree-Fock exchange term with an unknown, effective one-electron, exchange-correlation potential represented by the matrix F^{XC} . The formulation can potentially give exact results. The problem, of course, is to know the exchange-correlation potential and be able to compute the matrix F^{XC} . The energy that is a solution to the Kohn-Sham equations is given by

$$E = \sum_{\mu\nu} P_{\mu\nu} H_{\mu\nu} + \frac{1}{2} \sum_{\mu\nu\lambda\sigma} P_{\mu\nu} P_{\lambda\sigma} (\mu\nu|\lambda\sigma) + E_{XC} \quad \text{Eq.17}$$

This expression is identical to the Hartree-Fock energy except that the normal exchange term is missing and has been replaced by effective exchange-correlation energy, E_{XC} , that hides all the complexity. In line with the Hohenberg-Kohn theorem, this energy is a functional of the Kohn-Sham density,

$$E_{XC} = E_{XC} [\rho^{\alpha}, \rho^{\beta}]$$

It is normal to describe an exchange-correlation energy density (per unit volume) f , such that

$$E_{xc} = \int f(\rho^\alpha, \rho^\beta) dr \quad \text{Eq.18}$$

The relationship between the exchange-correlation energy, E^{xc} , and the exchange-correlation matrix of the Kohn-Sham equations has been formulated in a convenient form by Johnson, Gill, and Pople.² In its simplest form, the relationship is,

$$F_{\mu\nu}^{xc\alpha} = \int \frac{\partial f}{\partial \rho^\alpha} \phi_\mu \phi_\nu dr \quad \text{Eq.19}$$

2.4.3 Exchange-correlation functional

Perhaps the principal issue in Density Functional Theory is developing accurate functionals that describe either the exchange or the correlation energy. Some functionals describe only the exchange energy and some describe only the correlation energy. To describe the total exchange-correlation energy one can just add an exchange functional to a correlation functional.

2.4.4 LDA exchange functional

A simple model system to try to understand the correct form that a functional could or should take is the uniform electron gas of constant density ρ . This system is simple enough that one can exactly calculate the exchange energy. The result in simple analytical form is just the Slater result and is called the Local Density Approximation (LDA) or Local Spin Density Approximation (LSDA) for exchange. It is called local because one takes the result for the uniform electron gas as describing the exchange energy at a local point r but then integrates this result over all space for the non uniform density of a molecular system.

2.4.5 LDA correlation functional

While the Slater result describes the LDA result for the exchange energy in a simple analytic form, no such simple result is available for the correlation energy of a uniform electron gas. The LDA results for a correlation functional are more complicated (and slightly more variable in practice) than the exchange functional. Most of the LDA functionals for correlation depend upon numerical results obtained by Monte Carlo simulations of the uniform electron gas. These “exact” results are then fit to an analytical functional form to obtain an LDA correlation functional.

2.4.6 Beyond the LDA - gradient corrected functional

The LDA results described above, either for exchange or correlation, or in combination, constitute the simplest approach to Density Functional Theory. A next approximation would be to recognize that electron densities in molecules are not constant but are larger near a nucleus, go to zero at large distances, etc. That is, electron densities have a gradient. Functionals that depend upon the gradient of the density as well as the density are called gradient-corrected functionals. Equivalently, one refers to the Generalized Gradient Approximation (GGA). The gradient of the electron density is usually described via three invariants,

$$\gamma_{\alpha\alpha} = \nabla_{\rho}^{\alpha} \cdot \nabla_{\rho}^{\alpha}$$

$$\gamma_{\beta\beta} = \nabla_{\rho}^{\beta} \cdot \nabla_{\rho}^{\beta}$$

$$\gamma_{\alpha\beta} = \nabla_{\rho}^{\alpha} \cdot \nabla_{\rho}^{\beta}$$

and the generalized gradient approximation has a function that is a generalization of the LDA functional. The Kohn-Sham matrices for GGA functionals have a more complicated form than for LDA functional. A convenient expression is given by Pople et. al.²⁰ as,

$$F_{\mu\nu}^{XC\alpha} = \int \left\{ \frac{\partial f}{\partial \rho^\alpha} \phi_\mu \phi_\nu + \left[2 \frac{\partial f}{\partial \gamma_{\alpha\alpha}} \nabla \rho^\alpha + \frac{\partial f}{\partial \gamma_{\alpha\beta}} \nabla \rho^\beta \right] \cdot \nabla (\phi_\mu \phi_\nu) \right\} dr \quad \text{Eq.20}$$

2.4.7 Hybrid functional

On an empirical basis, it has been determined that rather than completely replacing the Hartree-Fock exchange term by an exchange functional of the kind being described by DFT, better results can often be obtained by retaining a percentage of so-called “exact” exchange, i.e. the Hartree-Fock exchange term. These have been referred to as hybrid functionals as opposed to pure functionals. Thus, for example, the B3-LYP functional discussed below contains a mixture of 20% exact exchange with 80% of a pure exchange functional. Examples of Exchange Functionals: Hartree-Fock, Slater, Becke-88, Perdew-Wang-91, Gill-96, PBE-96, HCTH-98 and Correlation Functionals: VWN#5, Perdew-Zunger-81, Perdew-86, LYP, Perdew-Wang-91, PBE-96, HCTH-98. These functionals do not divide simply into a single exchange functional and a single correlation functional. B3-LYP This functional, defined, by Becke, contains an exchange functional that consists of:

20% - Hartree-Fock Exchange, 8% - Slater Exchange, 72% - Becke-88 Exchange plus a correlation functional that consists of: 19% VWN#5 Correlation and 81% - LYP Correlation. This unusual combination was empirically determined by comparing with the results of very accurate calculations.¹⁹

2.5 Application of DFT calculation

There are broad ranges of chemical information which can be obtained from DFT calculations, including molecular geometry, vibrational frequency, electron density, atomic charge, dipole moment, ionization energy, electron affinity, acid/base stability, hydrogen bond

strength, heat of reaction, UV-Vis spectral peaks, NMR shifts, EPR coupling constants, IR spectral peaks, transition structures, etc.²⁰ In this work, DFT calculations have been used in the following ways. Accurate chemical structures often within a few percent of those which are measured experimentally have been determined. Plots of molecular orbitals and graphs of their energies provided insights into chemical bonding. Calculations on cations and dications provided insights into the electrochemical processes explored by cyclic voltammetry. Molecular properties such as hfc (hyperfine coupling constants) were calculated to assist in interpretation of EPR spectra in both fluid and frozen solution.

References

1. Oldham, K. B.; Myland, J. C. *Fundamentals of electrochemical science* Academic Press: San Diego, 1994.
2. Bard, A. J.; Faulkner, L. R. *Electrochemical Methods: Fundamentals and Applications*. 2nd ed.; Wiley: New York, 2001.
3. Bond, A. M. *Broadening electrochemical horizons: Principles and illustration of voltammetric and related techniques*. Oxford University Press: Oxford, 2002.
4. Eklund, J. C.; Bond, A. M.; Alden, J. A.; Richard, G.; Compton, A. *Phys. Org. Chem.* **1999**, *32*, 1.
5. Gritzner, G.; Kuta, J. *Pure Appl. Chem.* **1984**, *56*, 461.
6. Boéré, R. E.; Boéré, R. T.; Masuda, J.; Wolmershauser, G., *Can. J. Chem.* **2000**, *78*, 1613.
7. Rieger, P.H. *Electron spin resonance: analysis and interpretation*. RSC Publishing: Cambridge, 2007.
8. Zavoisky, I. E. *J. Phys.* **1945**, *9*, 211.
9. Weil, J. A.; Bolton, J. R.; Wertz, J. E. *Electron Paramagnetic Resonance*. John Wiley & Sons: New York, 1994.
10. Wang, J. *Analytical electrochemistry*. 3rd ed.; Wiley-VCH: New York, 2006.
11. Goldberg, I. B.; Bard, A. J. *J. Phys. Chem.* **1971**, *75*, 3281.
12. Goldberg, I. B.; Boyd, D.; Hirasawa, R.; Bard, A. J. *J. Phys. Chem.* **1974**, *78*, 295.
13. Neudeck, A.; Kress, L. *J. Electroanal. Chem.* **1977**, *437*, 141.
14. Richter, R.; Kaiser, J.; Sieler, J.; Hartung, H.; Peter, C. *Acta Crystallogr., Sect B.* **1977**, *33*, 1887.
15. Hinchley, S. L.; Morrison, C. A.; Rankin, D. W. H.; Macdonald, C. L. B.; Wiacek, R. J.; Cowley, A. H.; Lappert, M. F.; Gundersen, G.; Clyburne, J. A. C.; Power, P. P. *Chem. Commun.* **2000**, 2045.
16. Gritzner, G. K. *J. Pure Appl. Chem.* **1984**, *56*, 461.
17. HyperChem 8.0.8; Hypercube, Inc.: Gainesville, FL 32601, 2002.
18. Parr, R. G.; Pearson, R. G. *J. Am. Chem. Soc.* **1983**, *105*, 7512.

19. Bond, A. M., *Broadening Electrochemical Horizons*. Oxford University Press: New York, 2001.
20. Young, D. C., Density Functional Theory. In *Computational Chemistry*, John Wiley & Sons, Inc.: 2002; pp 42.

Chapter 3

Tetraorganodiphosphines

3.1 Introduction

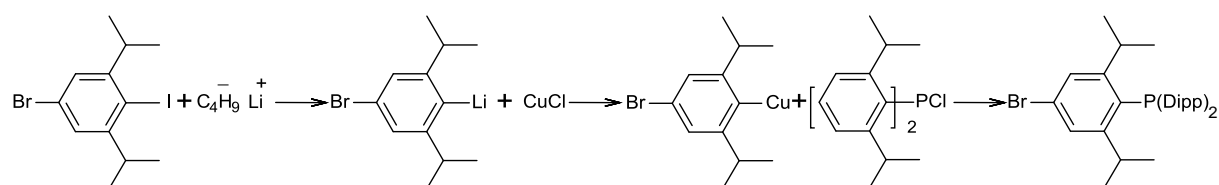
Although a long-known class of compounds, tetraorganodiphosphines retain considerable interest and still contain surprises as evidenced by ongoing interest in this class of compound.^{1, 2, 3, 4} Various reasons for this can be suggested. First, they provide a way to model an important element-element bond, namely the P–P single bond, in a simple environment. Secondly, R_4P_2 can usually be profitably discussed with reference to the very well characterized triorganophosphines R_3P . Thirdly, R_4P_2 have long been known to involve interesting and challenging conformational effects. In addition to all of these properties, these compounds became a source of interest for electrochemists due to the unique behavior of their radical ions. In this chapter, introduction to an interesting new tetraorganodiphosphine and attempts to fully understand its behavior will be described. In doing so, attempts to fill gaps in the knowledge of previously discovered tetraorganodiphosphines are undertaken by using DFT calculations and electrochemical investigations.

3.1.1 Synthesis of $Dipp_4P_2$

The synthesis of tetraorganodiphosphines never followed a single methodology, each chemist innovating their own method, and more than 15 methods are known for the synthesis of this class of compound with various substituents (see Section 1.2). The best explanation for this fluctuation is that the behavior of diphosphines changes with different substituents and one method cannot easily be applied in all cases. The validity of this concept is confirmed by lots of

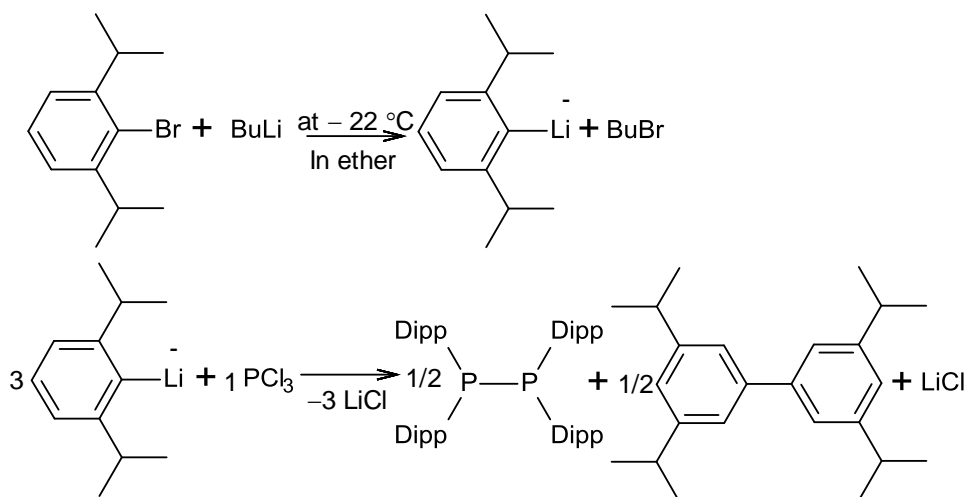
efforts to prepare a variety of R_4P_2 as explained in the first part of this chapter. Here there will be a report on different approaches to make diphosphines with more than one bulky group on the phosphorus atom. As mentioned previously (Section 1.2), three methods have recently been used to make a tetraorganodiphosphine with bulky substituents and these were followed as guides for the preparation of tetrakis(2,6-diisopropylphenyl)diphosphine ($Dipp_4P_2$) and tetrakis(2,4,6-triisopropylphenyl)diphosphine ($Tripp_4P_2$).

The inspiration for attempting to make $Dipp_4P_2$ came from attempts to make (4-bromo-2,6-diisopropylphenyl)*bis*(2,6-diisopropylphenyl)phosphine via the arylcopper reagents as described in Scheme 3.1.⁴ In monitoring this reaction using unlocked ^{31}P NMR spectroscopy, a prominent peak occurred at -38 ppm, which by comparison with other known diphosphines such as $Tripp_4P_2$ ($\delta -42.22$)⁵ suggested that this could correspond to $Dipp_4P_2$. After work up, in addition to ^{31}P NMR, mass spectrometry was carried on to prove the nature of the unknown product. By considering the reaction, the first explanation which comes to my mind in order to explain how $Dipp_4P_2$ formed is that in the second step of the reaction, the $\{4-Br-C_6H_2^iPr_2Cu\}$ reagent acted as a reducing agent instead of a nucleophile. Thereby the P–Cl bond was reduced and dimerization of $Dipp_2P^\bullet$ radicals formed the P–P bond. At this point, I set out to discover the best synthetic route to make $Dipp_4P_2$ on purpose.



Scheme 3.1. Possible synthetic route to (4-bromo-2,6-diisopropylphenyl)*bis*(2,6-diisopropylphenyl)phosphine via 4-bromo-2,6-diisopropylphenylcopper

A search of the literature indicated that Dipp_4P_2 is unknown and the closest analog in the literature is the closely-related tetrakis(2,4,6-triisopropylphenyl)diphosphine (Tripp_4P_2) which was prepared accidentally by Brady and coworkers from Ireland.⁵ They reported synthesis of Tripp_4P_2 by the treatment of PCl_3 with an excess of 2,4,6-triisopropylphenyllithium (or the equivalent Grignard reagent) in 70% yield. While under normal circumstances in this kind of reaction the triarylphosphine would be expected to form, presumably excessive steric bulk prevents this, and the resulting diphosphine is produced by the remaining equivalents of organolithium reagent. Repeating this approach, DippBr was reacted with one equivalent of $n\text{BuLi}$ at $-22\text{ }^\circ\text{C}$ in ether. Complete metallation was confirmed by taking a small aliquot of the Dipp^-Li^+ mixture, quenching it with wet ether in a small vial, removing solvent and obtaining a ^1H NMR spectrum to prove that the parent hydrocarbon had indeed been formed. Then a solution of PCl_3 in ether was added dropwise via cannula to the organolithium reagent in the ratio 1 to 3 at $-22\text{ }^\circ\text{C}$ and stirred until it reached room temperature (Scheme 3.2). After making the DippLi , which is straightforward, there are two substitutions to form Dipp_2PCl , followed by reduction and then dimerization of $\text{Dipp}_2\text{P}^{\cdot-}$.



Scheme 3.2. Possible synthetic route for Dipp_4P_2 via the organolithium reagent reaction

An orange solution with a white precipitate of LiCl was obtained, which was filtered the following morning and the solvent was removed under vacuum. The orange oil obtained thereby was then extracted with hexane, the last trace of LiCl was filtered off and the yellow oil obtained after removing the solvent was dissolved in hot ethanol and cooled to $-30\text{ }^{\circ}\text{C}$, affording needle shape crystals. The crystal structure of this product was determined by X-ray crystallography which showed that it was actually the compound $\text{Dipp}_2\text{P}(\text{O})\text{Cl}$. This species has not been previously reported in the literature (Figure 3.1 and Table 3.1; derived structural parameters are provided in the Appendix). The $^{31}\text{P}\{^1\text{H}\}$ NMR spectrum of these crystals showed a peak at +46.2 ppm, which can be compared to that of $\text{Ph}_2\text{P}(\text{O})\text{Cl}$ which has a phosphorus peak at +44 ppm,⁶ and 86 ppm for starting material. The formation of this product probably stems from oxidation of Dipp_2PCl during the recrystallization step. It suggests that the third step of the reaction, i.e. reduction of Dipp_2PCl , does not occur efficiently. Thus, this method for the synthesis of Dipp_4P_2 was abandoned.

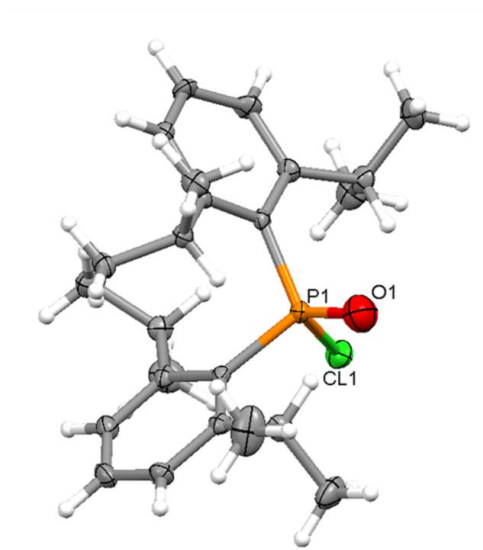
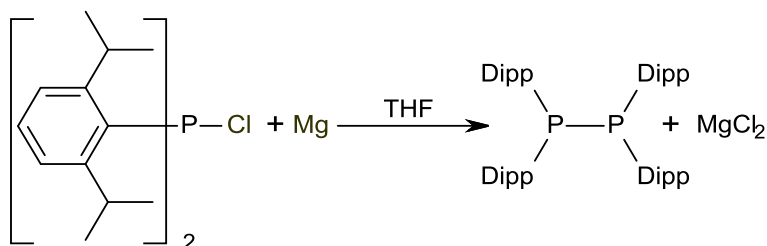


Figure 3.1. A thermal ellipsoids plot (30% probability distribution) of $\text{Dipp}_2\text{P}(\text{O})\text{Cl}$ as found in the crystal lattice.

Table 3.1. Crystal data and structure refinement for Dipp₂P(O)Cl

Space group	P2(1)/c
a/ Å	10.766(3)
b/ Å	14.997(5)
c/ Å	15.032(5)
β	108.765(4)°.
Z	2
Goodness-of-fit on F ²	1.018
Final R indices [I > 2σ(I)]	R1 = 0.0723, wR2 = 0.1647
R indices (all data)	R1 = 0.1659, wR2 = 0.2073

Based on previous reports in the literature, an air stable product was expected for this reaction.⁵ However, the observation of oxidation of Dipp₂PCl to Dipp₂P(O)Cl indicates the importance of pursuing the synthesis of Dipp₄P₂ under the rigorous exclusion of moisture. Reduction of the P–Cl bond, which looks like an easier and more efficient way to make the target diphosphine, was the next approach taken. Dipp₂PCl was synthesized previously in the Boeré lab. There are some reported methods for synthesis of tetraorganodiphosphines like Ph₄P₂ by using the reduction of diarylphosphinous chloride by metals like Na.^{7,8} As a first attempt in using active metals for the synthesis of Dipp₄P₂, the reduction of Dipp₂PCl with excess solid magnesium was undertaken (Scheme 3.3).

**Scheme 3.3. Synthesis of Dipp₄P₂ by using excess Mg turnings**

Magnesium turnings, which were activated under high vacuum at 80 °C, were treated with Dipp₂PCl in freshly distilled THF under an atmosphere of nitrogen. The first trial used excess Mg and in this trial the mixture was refluxed for one night and the resulting yellow solution showed two major peaks in an unlocked ³¹P NMR monitoring spectrum: a singlet at -38 ppm and a doublet at -103.1 ppm (¹J_{PH} = 228.4 Hz) (changes to a singlet in the ³¹P{¹H} spectrum). The -38 ppm peak which was that of Dipp₄P₂ was the major component and the doublet at -103.1 ppm was attributed to Dipp₂PH which was the minor component and was very close to Tripp₂PH which appears at -104.9 ppm (¹J_{PH} = 226.2 Hz).⁹ In future attempts, by monitoring the reaction for different times, the optimal reaction time was obtained which was 2 hours.

Based on experience from the ⁿBuLi reaction, the product was treated as an air sensitive compound and the remaining Mg turnings were filtered off using a filter stick and solvent was removed under vacuum to get a yellow solid. Three different methods were used to separate the Dipp₂PH component from Dipp₄P₂: column chromatography, sublimation and recrystallization. Among all these methods, recrystallization worked. The first solvent which was used for recrystallization was heptanes which works well; however the resulting crystals did not diffract at all. The next solvent tried was ethanol and for this step it would be better to use degassed solvent. Hence, ethanol was degassed by purging N₂ through for a couple of hours. Degassed solvent was warmed up and added dropwise to the mixture which was heated on an oil bath and then left to reach RT and then cooled to -30 °C. Again, the crystals which were obtained from ethanol were too small for crystallography. Finally, good quality crystals were obtained by using freeze-thaw-degassed isopropanol after cooling to -30 °C (76% yield).

3.1.2 Attempts to prepare Tripp₄P₂

In order to obtain a comparison for the electrochemical and EPR study of Dipp₄P₂, synthesis of the previously reported Tripp₄P₂ has been tried.⁵ This compound appears to have been made by accident in this research group (they were after Tripp₃P, which was eventually made by Sasaki and co-workers),⁴ and it has never been followed up. It would be an interesting comparison for a number of properties since Dipp and Tripp have the same steric effect but different electronic effects.

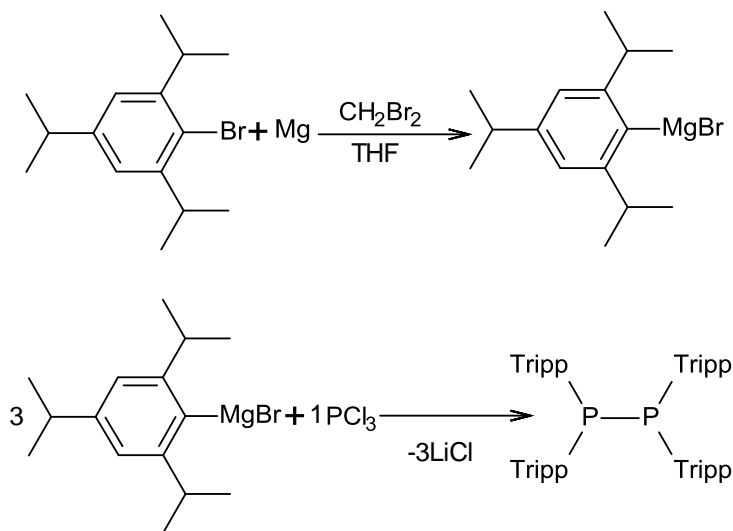
Since the reaction using excess solid magnesium works very well for Dipp₄P₂ and the difference between Dipp and Tripp is in just one isopropyl group in the remote *para* position, the first trial followed the same route which works for Dipp₄P₂. Excess activated magnesium turnings were refluxed with Tripp₂PCl in THF and the first unlocked ³¹P NMR spectrum was run after 2 hours which showed nothing changed in solution and what was in the flask was just one peak at 88 ppm (Tripp₂PCl). Refluxing for one night did not even effect initiation of the reaction. After one night refluxing, dibromoethane was added to try to initiate the reaction which was a good idea since after one hour a reaction started to occur. Unlocked ³¹P{¹H} NMR of yellow solution at this point showed two peaks, one singlet at 88 ppm which was starting materials and the other singlet at -102.6 ppm which turns into a doublet in the ¹H coupled spectrum (¹J_{PH} = 228.4Hz). The experience from Dipp₄P₂ reaction suggested that reduction of P-Cl bond is a competition reaction between making a diphosphine and the phosphine hydride. Therefore -102.6 ppm peaks belongs to Tripp₂PH which seems more favorable in this reaction in comparison with Dipp₄P₂.⁹ Continuing the reaction for one more night for reflux was the best proof for my understanding of this reaction, since all the starting material changed to Tripp₂PH without any sign of formation of the P-P bonded compound. Two more trials convinced me that

reducing the P–Cl bond with Mg would not be a good choice for making Tripp₄P₂. In further trials, sometimes there was a peak at 16.5 ppm in ³¹P{¹H} NMR which was changed into a doublet again in ³¹P-¹H coupled spectrum and was in the same range with Ph₂P(O)H which has a phosphorus peak at 17.6 ppm.¹⁰ Therefore, the product of reducing the P–Cl bond by Mg is Tripp₂PH which can be oxidized to Tripp₂P(O)H if some adventitious oxygen enters the reaction flask.

Following the report by Brady,⁵ TrippBr was reacted with one equivalent of ⁿBuLi at –22 °C in ether. Taking a small aliquot of the Tripp[–]Li⁺ mixture, quenching it with wet ether, removing solvent and running a ¹H NMR shows that still there is some TrippBr left. The first thing to do was refluxing for a couple of hours to help the reaction to run but in this case after 3hrs refluxing nothing changed. The second step was adding one more equivalent ⁿBuLi since proton NMR spectrum integration shows that mostly half of the reaction has been done. What was sought after here was one septet, since completeness of the metallation followed by quenching should result in 1,3,5-triisopropylbenzene, which has three symmetry equivalent isopropyl groups, while if there is a TrippBr in the mixture then there will be two kinds of isopropyl groups and two septets.

By adding the second equivalent of ⁿBuLi and stirring for half an hour, reaction is completed. A solution of PCl₃ in ether was then added to this solution at –22 °C in the ratio of 1 PCl₃ to 3 TrippLi. Stirring the light yellow solution overnight to reach room temperature resulted in a yellow brown solution with a white precipitate of LiCl. After filtering, volatile components were removed under vacuum, leaving a thick yellow oil behind. ³¹P{¹H} and coupled spectra showed a wide mixture of products. The major peak was at 88 ppm (Tripp₂PCl) and minor peak at –37 ppm that was expected for Tripp₄P₂ and one minor peak at –103 ppm, which was

Tripp₂PH.⁹ Since still most components in flask were Tripp₂PCl, I decided to add Li wire to accelerate the reaction toward the end point. One equivalent of Li wire was measured based on the PCl₃ that comes to 0.4 cm of Li, added to the mixture, and refluxed for half an hour. Unlocked ³¹P{¹H} NMR spectrum showed an increase in both Tripp₂PH and Tripp₄P₂ peaks but more time for reflux resulted in mostly Tripp₂PH. This method repeatedly gave the same product. This is consistent with the fact that active metals like Li are known to cleave the P–P bond to Tripp₂P[−]Li⁺. This then reacts with moisture to give Tripp₂PH.

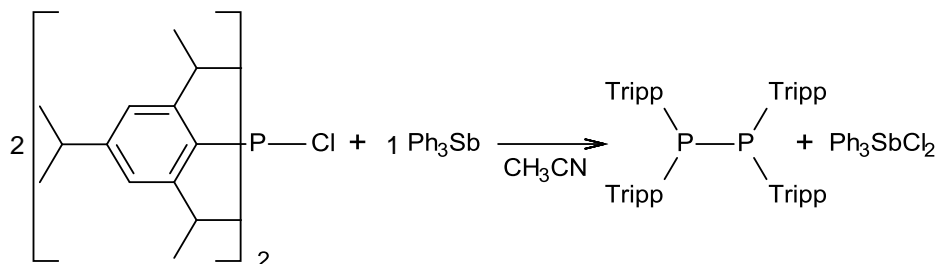


Scheme 3.4. Proposed synthetic route for Tripp₄P₂ via the Grignard reagent.

Since the Li route did not prove to be effective, the next thing to attempt was to make the Grignard reagent, TrippMgBr, from the bromide (Scheme 3.4). In the published work by Brady,⁵ the bromide was combined with Mg turnings, activated on high vacuum at 180 °C (based on our own experience), and refluxed for 30 min in THF with 0.05 mL dibromoethane. The resulting yellow solution was refluxed overnight. To speed up the reaction times, we used the higher boiling ether, THF. After one night most of the magnesium had been consumed, and the reaction was cooled in an ice bath. A separate dry ice bath (< −15 °C) was made to cool a flask containing

three equivalents of TrippMgBr in THF. The one equivalent PCl_3 solution in THF was added via a cannula, and the mixture was allowed to warm to room temperature. A clear yellow solution was obtained in the morning, which unlocked $^{31}\text{P}\{^1\text{H}\}$ NMR spectrum showed one peak at 88 ppm which was Tripp_2PCl . This method twice gave the same results. For reasons that are entirely unclear, the third isopropyl group on the phenyl ring here leads to Tripp_2PCl which was a product of two substitutions of Cl with MgBr and not the expected reduction of the P–Cl bond from the third equivalent of Grignard reagent.

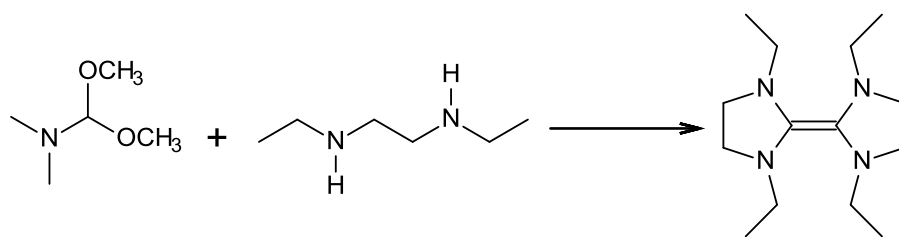
Another alternative for reducing the P–Cl bond, which works well for sulfur halides, is triphenylantimony in a ratio of 2 to 1 in acetonitrile. What was expected was Tripp_4P_2 as a solid and Ph_3SbCl_2 in the solution phase. Refluxing for a couple of hours resulted in a colorless solution which unlocked $^{31}\text{P}\{^1\text{H}\}$ NMR spectrum showed to be starting material. Refluxing for a couple of days did not change the result (Scheme 3.5).¹¹



Scheme 3.5. Possible synthetic route for Tripp_4P_2 by reduction of P–Cl bond by triphenylantimony

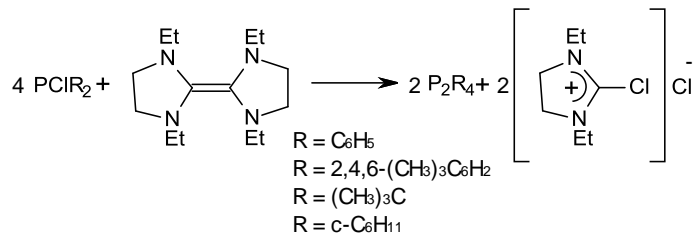
In 1986 an intriguing report was published on using 1,3,1',3'-tetraethyl-*bis*(2,2'-imidazolidene) as a reducing agent for the synthesis of diphosphines.¹² Unsuccessful trials on making Tripp_4P_2 pushed me to try to make this imidazolidine and then try reducing the P–Cl bond with this electron-rich olefin. A mixture of N,N-dimethylformamide dimethylacetal and N,N'-diethylethylenediamine in dry benzene was heated in a distillation vessel under N_2 gas. The

temperature was increased from 10 °C until the first drops were observed at 55 °C (the methanol/benzene azeotrope forms at 58 °C) and the last drops were collected at 78 °C which was close to the boiling point of benzene. Then the distillation vessel was disconnected and the remaining benzene was removed under vacuum. Using a 14/30 jacketed Vigreux column for vacuum distillation and by increasing the temperature each hour by 20 °C, two fractions were collected, one at 62-75 °C and other between 80-90 °C (0.1 mbar) (Figure 3.6). ¹H NMR spectra of the contents of both flasks shows the mixture of *cis* and *trans* isomers of the desired 1,3,1',3'-tetraethyl-2,2'-bis(imidazolidene). In a second attempt, even with cleaning the glassware between collecting the two fractions, the same mixtures were obtained in the two fractions.



Scheme 3.6. Synthesis of 1,3,1',3'-tetraethyl-bis(2,2'-imidazolidene)

Having both isomers in the reaction should not prevent forming the persistent phosphinyl radical which is generally in equilibrium with its dimer. Hence, it was decided to try for the synthesis of Dipp_4P_2 by reducing the P–Cl bond in Dipp_2PCl by this strong reducing agent. Meanwhile, there is a report of the synthesis of R_4P_2 compounds in which R is C_6H_5 , 2,4,6- $(\text{CH}_3)_3\text{C}_6\text{H}_2$, $(\text{CH}_3)_3\text{C}$, $\text{C}-\text{C}_6\text{H}_{11}$ using *bis*-imidazolidene as a reducing agent which works very well (Figure 3.7).¹² Lappert *et al.* in his paper claimed that reductions of diarylphosphinous chlorides to the tetra-aryldiphosphines proceeded much more rapidly and under much milder conditions with the *bis*-imidazolidene than with the metal reducing agents.



Scheme 3.7. Proposed synthetic route for tetraorganodiphosphines by using *bis*-imidazolidene

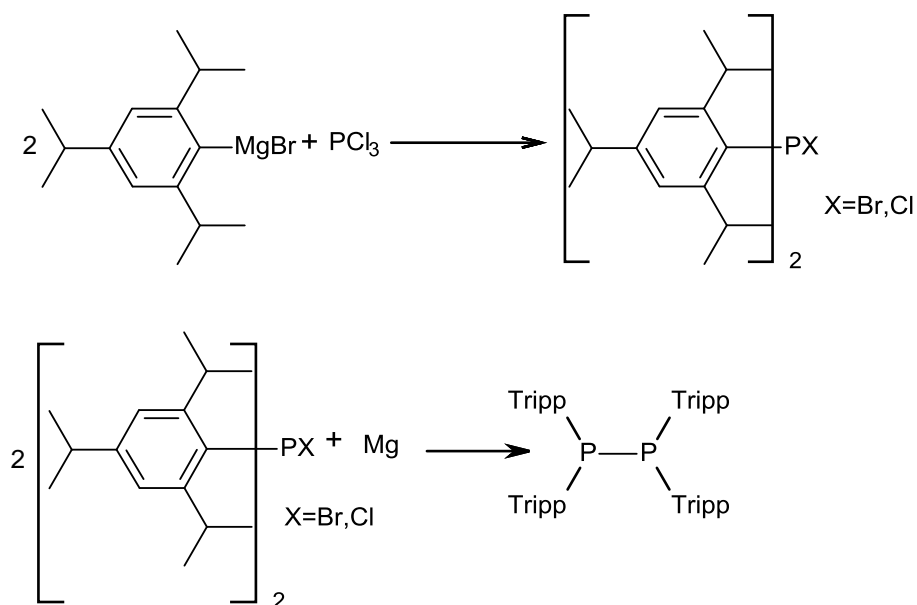
A solution of the *bis*-imidazolidene (20% excess) in toluene was added slowly at 0 °C to a stirred solution of 4 equivalents of Dipp₂PCl in toluene under a nitrogen atmosphere. The mixture was stirred at 0 °C for 2 hours. It was expected that the carbonium salt by-product precipitating out from the toluene solution during the reaction and Dipp₄P₂ should be obtained in the solution phase. The reduction of hindered chloro-*bis*(2,6-diisopropylphenyl)phosphine by *bis*-imidazolidenes led to phosphinyl radicals which dimerize to yield the diphosphines. Nevertheless, what was observed after 3 hours refluxing in unlocked ³¹P{¹H} NMR spectrum was starting material. A second equivalent of *bis*-imidazolidene was then added and stirred for one night. Some solids appeared in the flask but no change was seen in NMR spectra. Refluxing the solution for half an hour helped the reaction and a small peak of Dipp₄P₂ appeared along with Dipp₂PH and still some Dipp₂PCl. One more equivalent of *bis*-imidazolidene was added and the mixture refluxed for one night. In the morning lots of precipitate was observed with a clear yellow solution. The NMR spectrum this time showed mostly Dipp₂PH and a small peak for Dipp₄P₂. Most likely controlling the radical toward the making of dimer by *bis*-imidazolidene is not an easy task. On the other hand, the reaction time was not nearly as fast as Lappert reported in his paper, which in this case may be caused by the difference in substituents, which can directly affect reaction time and energy. In order to determine whether the problem lay with

using the imidazolidene reagent with bulky substituents on R_2PCl , the same reaction carried but this time with Ph_2PCl to make Ph_4P_2 , which had previously been prepared by this route. The same procedure was followed but with more caution since Ph is less congested and has the potential to oxidize easier. Therefore, this time, the toluene was degassed. Again, after stirring for 2 hours nothing changed but this time UV light was used to help to generate radicals. This reaction continued under the beam of two lamps for one day. After one day, mostly starting material and small peak at -15 ppm was detected in the mixture, showing that reaction was proceeding slowly, but little improvement after 4 days convinced us to discontinue this reaction.

The next trial followed the same method but this time for making $Tripp_4P_2$. This time a photochemical reactor was used, which is an intense source of ultraviolet light, approximately 1.65×10^{16} photons/sec/cm³ at 2537 nm. This method worked since the peak at -41 ppm appeared which was expected for $Tripp_4P_2$ ⁹ but the major component was starting material ($Tripp_2PCl$) which by increasing the reaction time slowly changed to $Tripp_4P_2$. After one week the reaction was stopped since it was a waste of energy and time and the rate of the reaction was too slow. Attempts to do work up and get pure product resulted only in a mixture of starting material, $Tripp_4P_2$, $Tripp_2PH$ and $Tripp_2POH$.

The final attempt to synthesize $Tripp_4P_2$ came from a paper by D. J. Brauer *et al.* that was published in 1996.⁹ One of the major methods which worked for them was making the mixed halophosphines R_2PX ($X = Br, Cl$) and then reduction of the halophosphines with Mg powder to make the desired phosphine hydride. The reaction using Grignard reagent from $TrippBr$ followed the procedure described above. The solution of Grignard reagent in THF was added slowly via the cannula to the solution of PCl_3 in the ratio of 2 to 1 at -60 °C and stirred to reach RT. An

unlocked $^{31}\text{P}\{^1\text{H}\}$ NMR spectrum of the resulting yellow solution shows two peaks at 88 ppm (Tripp_2PCl) and 76 ppm (Tripp_2PBr).



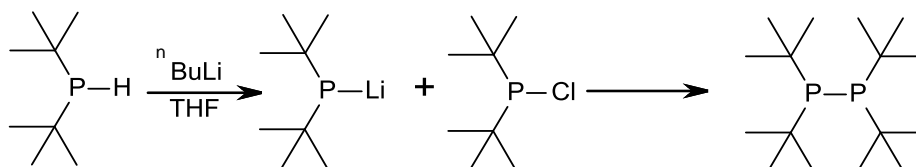
Scheme 3.8. Proposed synthetic route for Tripp_4P_2 by reducing the mixed halophosphines

Solvent was removed under vacuum, leaving thick, yellow oil behind. The residue was dissolved in n-pentene, filtered and dried under the high vacuum. Pale yellow solids were obtained which were taken to the glove box to weight the appropriate amount for the next step that was the reduction with Mg powder. The solution of $\text{Tripp}_2\text{PCl/Br}$ in THF was added to the suspension of Mg powder in THF by syringe and the mixture stirred for one night. The mixture was analyzed by unlocked $^{31}\text{P}\{^1\text{H}\}$ NMR spectrum and not only showed the signal corresponding to Tripp_4P_2 , but a major signal related to Tripp_2PH at -103 ppm ($^1J_{\text{PH}} = 228.4$ Hz) and TrippPH_2 at -158.8 ppm ($^1J_{\text{PH}} = 204.1$ Hz).¹³ In all trials, attempts to get a pure Tripp_4P_2 or even Tripp_2PH crystal were unsuccessful. Recrystallization was tried from different solvents like isopropanol, ethanol, methanol, toluene, benzene, heptene. Although making an exact conclusion is not possible, it can be suggested that whereas the hydride is the bulk of the product in the

Tripp, the dimer is more favorable for Dipp. Moreover, whether this hydrogen comes from solvent, water, or H from the isopropyl group in the *para* position is not obvious.

3.1.3 Synthesis of ${}^t\text{Bu}_4\text{P}_2$

An efficient general route to pure symmetrical diphosphines was found to be via the reaction of lithium diarylphosphinyl anion with its chlorinated derivatives as reported by Deborah L. Dodds and coworkers (Scheme 3.9).¹



Scheme 3.9. Synthesis of 1,1,2,2-tetra-*tert*-butyldiphosphane

Following the exact same procedure, ditertbutylphosphine reacted with one equivalent of ${}^n\text{BuLi}$ at $-78\text{ }^\circ\text{C}$, wherein a slight excess of ${}^n\text{BuLi}$ was added. An unlocked ${}^{31}\text{P}\{^1\text{H}\}$ NMR spectrum of the resulting creamy-white solution after 2 hours showed one singlet at 39 ppm which was proof of forming ${}^t\text{Bu}_2\text{PLi}$. Adding one equivalent of chloroditertbutylphosphine at $-78\text{ }^\circ\text{C}$ and stirring for one night resulted in a clear colorless solution with a large amount of white precipitate. Again, an unlocked ${}^{31}\text{P}\{^1\text{H}\}$ NMR spectrum showed one major peak at 40.1 ppm (${}^t\text{Bu}_4\text{P}_2$). Solvent was removed under high vacuum and followed the literature preparation, the mixture was dissolved in degassed methanol to remove LiCl and the white solid recrystallized from methanol. All efforts to get crystals at this step were unsuccessful because of the presence of remaining LiCl. Modifying the procedure in order to properly purify the material was considered. Therefore, extraction of ${}^t\text{Bu}_4\text{P}_2$ with pentane followed by filtration was added to the procedure. Then recrystallization with very well degassed methanol gave pure crystals. These

reactions demonstrated very high sensitivity to air, which resulted in additional peaks (36 and 94 ppm) which proved to be the monoxide form of tBu_4P_2 .¹⁴ Working under exacting air-free conditions was necessary to obtain pure crystals.

3.2 Crystal structure of Dipp_4P_2

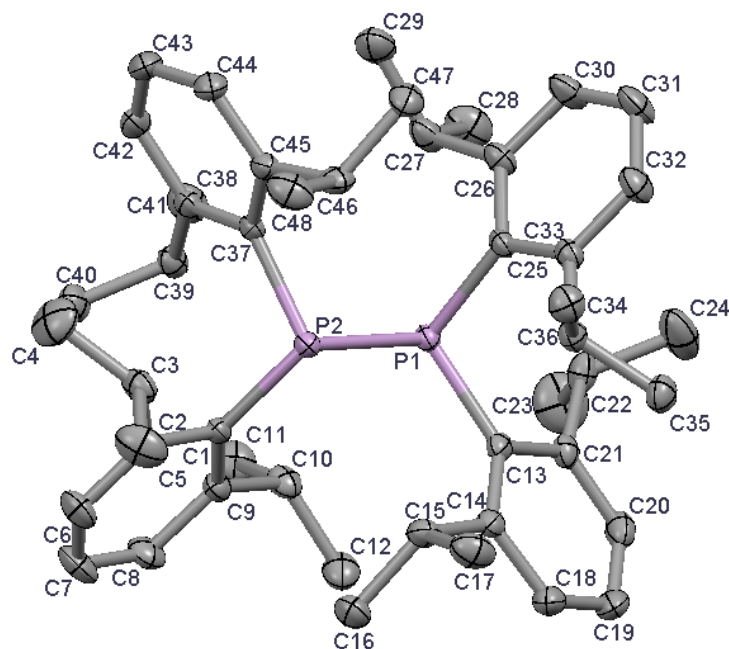


Figure 3.2. A thermal ellipsoids plot (30% probability distribution) of Dipp_4P_2 as found in the crystal lattice.

The molecule crystallized in the monoclinic space group $P2_1/c$, with four molecules per unit cell which is standard for this space group. An ORTEP diagram is shown in Figure 3.2. Crystal data and structure refinement parameters are included in the Appendix and a summary of the crystallographic data can be found in Table 3.2. Figure 3.3 presents alternate representations as spheres with van der Waals` radii or arbitrary radii, and Figure 3.4 is a packing diagram. The P–P bond length is 2.2233(6) which is only slightly longer than that found in Ph_4P_2 (2.217(1) Å)

after considering the esd's.²¹ The sum of angles around phosphorus is only 318.9°, indicative of a relatively pyramidal structure at phosphorus.

Table 3.2. Crystal data and structure refinement for Dipp₄P₂

Space group	P2 ₁ /c
a/ Å	13.3256(13)
b/ Å	18.4854(19)
c/ Å	17.5047(18)
β	99.2750(10)°.
Z	4
Goodness-of-fit on F ²	1.032
Final R indices [I>2σ(I)]	R1 = 0.0494, wR2 = 0.1138
R indices (all data)	R1 = 0.0740, wR2 = 0.1276

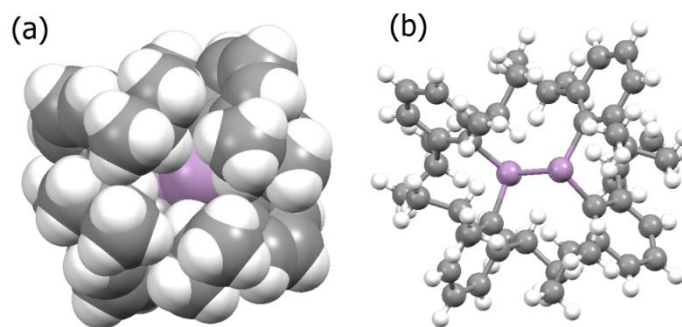


Figure 3.3. (a) A “space filling” diagram and (b) a “ball and stick” representation of Dipp₄P₂

Since the molecule occupies the general equivalent position in the space group, there is no crystal lattice symmetry imposed on the observed geometry. The structure has close to molecular C_2 symmetry, but this is not imposed by the lattice. The molecular structure displays a close to antiperiplanar conformation. Another noticeable feature of the structure is that the two aryl rings which are located on one side of the P–P single bond are orthogonal (perpendicular) to

the phosphorus phosphorus bond (Figure 3.5(a)) while the two other aryl rings are coplanar or close to coplanar geometry with phosphorus (Figure 3.5(b)), though not with each other.

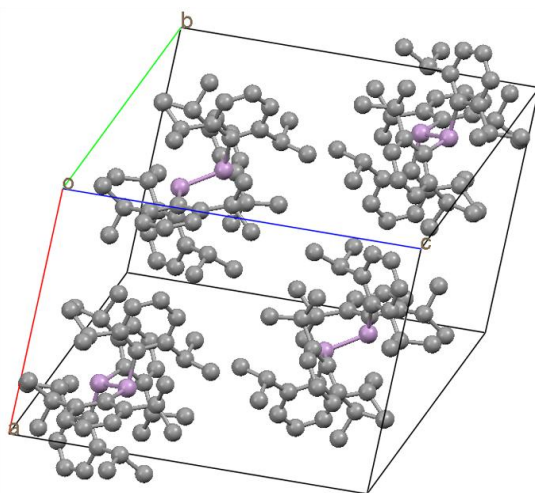


Figure 3.4. Packing diagram of molecules in the unit cell

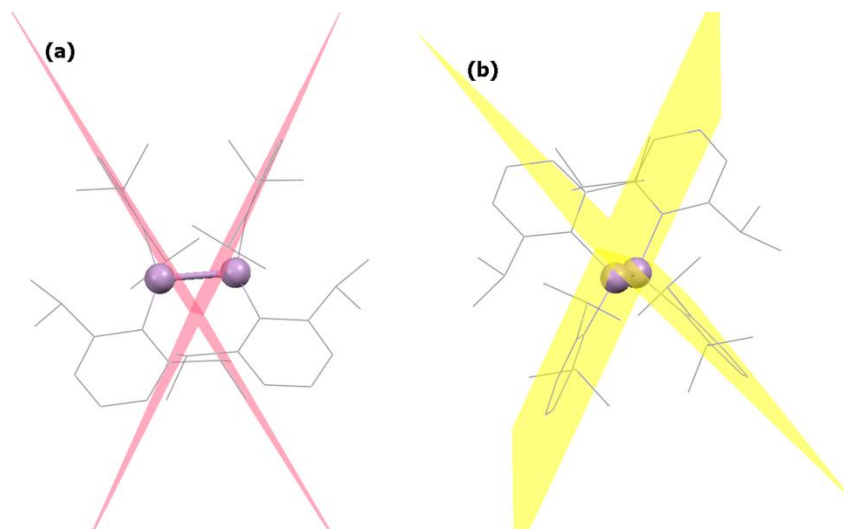


Figure 3.5. (a) Illustration of orthogonal aryl groups in Dipp₄P₂ with pink colour (b) illustration of coplanar aryl groups in Dipp₄P₂ with yellow color

The two ortho ⁱPr groups are oriented in the “Vee-back” conformation that have been observed in all solid-state structures determined for Dipp groups, but they are also quite

symmetrical above and below the ring planes.^{15,16,17} An analysis of the packing diagrams showed no unusual characteristics, and there is no evidence of significant intermolecular contacts beyond normal van der Waals' interactions. Taking a closer look at data obtained from Dipp₄P₂ and some other R₄P₂ compounds showed lot of diversities in P–P bond length, $\sum\{\angle C-P-C\}$ bond angles around phosphorus, preferred conformation and deviation of phosphorus from the plane of the aryl rings. Table 3.3 summarizes the most similar R₄P₂ structures. One of the important features is that in all structures of tetraaryldiphosphines, on each phosphorus, one of the phenyl rings is oriented approximately parallel to the plane of the phosphorus–phosphorus bond, whereas the other ring lies roughly perpendicular to this plane. For tetraphenyldiphosphines without *ortho* substituents, the two coplanar and two orthogonal aryl groups are centro-symmetrically disposed, whereas in most of the structures, rings with the same orientation are located on the same side of the P–P bond (resulting in C₂ symmetry). The P atom on Dipp₄P₂ and Tripp₄P₂ are found to be more out of the aromatic carbon atom plane in comparison with other structures. It was noted that an antiperiplanar staggered conformation of tetramethyl and tetraaryl diphosphines pushes the lone pairs on each phosphorus to the maximum or near to maximum spatial separation.⁵ This pattern is in contrast with bulky alkyl diphosphines, where a gauche conformation is preferred.⁵ Hence, the same degree of separation of the lone pairs could not be attained in the gauche conformation. On the other hand, both Dipp₄P₂ and Tripp₄P₂ prefer the antiperiplanar conformation in their structure, which is in agreement with what is expected for bulky aryl substituents. The P–P bond lengths of Dipp₄P₂ and Tripp₄P₂ are not different within experimental uncertainty at the 99% confidence level, largely due to the low precision of the latter's structure. While the bond length of the lower-steric-demand tetramesityl analogue appears longer than for triisopropylphenyl and diisopropylphenyl derivatives, consideration of the experimental

uncertainties does not make these values different at the 99% confidence level. In conclusion, it is hard to find a reasonable pattern between P–P bond length and bulkiness of substituents. The $\Sigma\{\angle\text{C–P–C}\}$, which is used as a comparison parameter for flattening of the phosphorus pyramid and hence of steric pressure, shows very close similarity for Dipp_4P_2 and Tripp_4P_2 , as expected. The highest value of $\Sigma\{\angle\text{C–P–C}\}$ has been calculated for $t\text{Bu}_4\text{P}_2$ which means that more steric pressure causes more flattening of the phosphorus pyramid in this compound.³ The final investigation for completing this comparison is the symmetry elements. Even though most of them do not have a crystallographically imposed (site) symmetry, most of them have approximate C_2 molecular symmetry (Table 3.3).

Table 3.3. Selected intra-atomic distances (Å) and angles (°) and space group for some R_4P_2 compounds from X-ray diffraction data.

R_4P_2 compounds	P–P bond length(Å)	$\Sigma\{\angle\text{C–P–C}\}(\text{°})$	Space group	Z	Site symmetry	Molecular symmetry
$t\text{Bu}_4\text{P}_2$ ³	2.235(3)	330.0	$\text{P}2_12_12_1$	4	1	2
Tripp_4P_2 ⁵	2.246(16)	320.0	P–1	2	1	2
Dipp_4P_2	2.224(1)	319.6	$\text{P}2_1/\text{c}$	4	1	2
$[(\text{Me}_3\text{Si})_2\text{Me}]_4\text{P}_2$ ¹⁸	2.310(9)	316.2	$\text{P}2_1/\text{c}$	4	1	2
Cy_4P_2 ¹⁹	2.215(2)	313.0	P–1	2	1	2
Mes_4P_2 ²⁰	2.259(6)	311.6	$\text{P}4_12_12$	4	2	2
Ph_4P_2 ²¹	2.217(1)	298.3	$\text{P}2_1/\text{n}$	2	–1	–1
Me_4P_2 ²²	2.212(1)	295.4	C_2/m	2	2/m	2/m

3.3 Discussion of NMR studies of tetraorganodiphosphines

Exhaustive NMR studies of Dipp_4P_2 were undertaken. The obtained results are interpreted with the help of the spectra reported, but not analyzed in depth, for Tripp_4P_2 . The solution–phase

^1H NMR spectrum (Figure 3.6) shows four different CH signals (three septets and a doublet of septets) with equal integration, as well as 8 different CH_3 doublets. The CH signals integrate correctly for 2H each while the methyl doublets fit for 6H each; the doublet of septets at $\delta = 5.24$ is shown to be due to additional coupling to a single ^{31}P nucleus by a $\{^{31}\text{P}\}^1\text{H}$ experiment. For Tripp_4P_2 , 11 peaks have been reported in the CH_3 environments and four septets for CH in isopropyl groups with the lower frequency CH also being a doublet of septets.⁵ In the aromatic region 8 *meta* and 4 *para* signals can be detected. Assigning atoms in this structure was impossible without running 2D proton and 2D proton-carbon NMR. Looking at the correlation spectroscopy (COSY) spectrum helped in obtaining the connection between CH_3 and CH groups which is summarized in Table 3.4 and Figure 3.7.

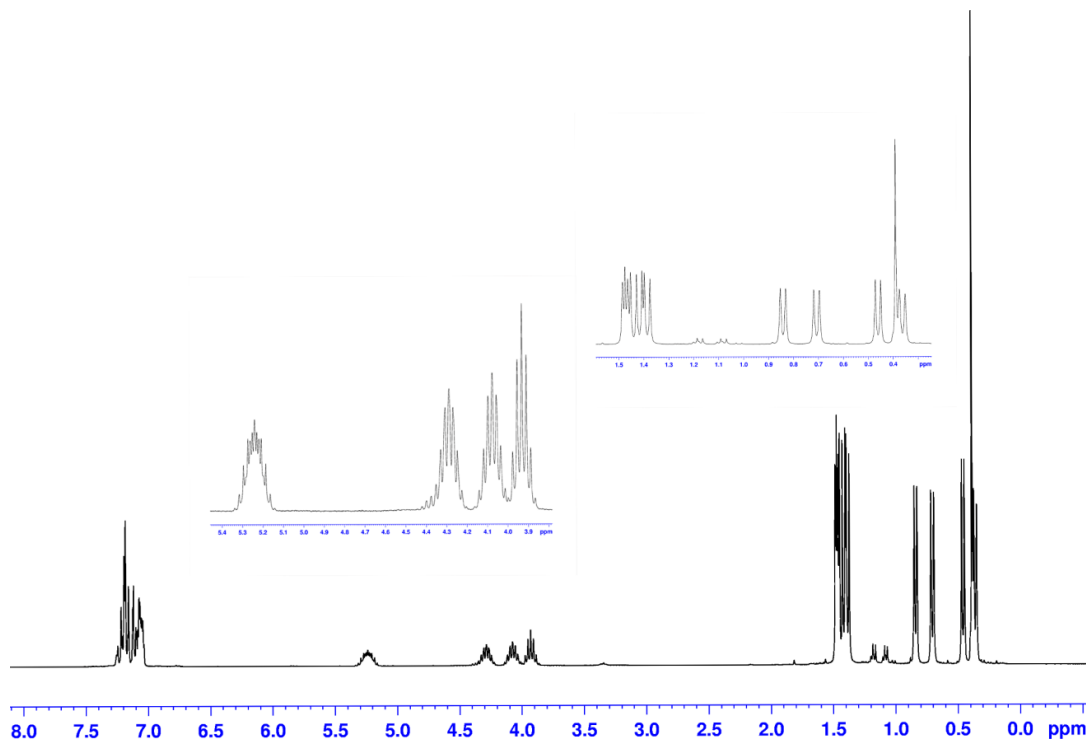


Figure 3.6. Proton NMR spectra of Dipp_4P_2 in C_6D_6 at RT

The next step was looking at the solid-state structure obtained from crystallography to answer whether or not the NMR evidence supported retention of the geometry seen in the solid

structure (*anti* with C₂ symmetry) or whether the geometry switches to the *gauche* conformation that has been claimed for Mes₄P₂ in solution.²³ From a first glance at the NMR spectrum, it is obvious that the molecule has symmetry of order two and displays restricted rotation about the P–C bonds; otherwise, we should see two sets of 4 equivalent Dipp groups instead four sets of two.

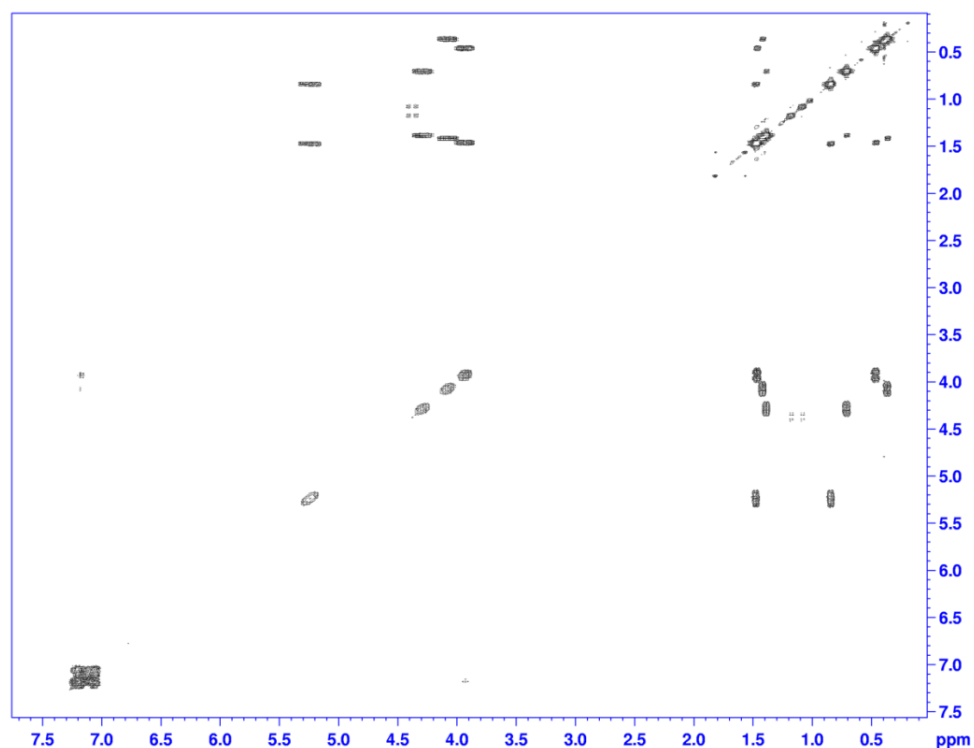


Figure 3.7. COSY NMR spectrum of Dipp₄P₂ in C₆D₆

A striking feature of the ¹H NMR spectra of both Dipp₄P₂ and Tripp₄P₂ is the extremely wide range observed for the chemical shifts of both the methyl and methine signals. The methyl shifts display particularly high-frequencies for some groups. Previous experience has shown that when Dipp groups are closely clustered, anisotropic ring currents from one ring affect the isopropyl signals of neighboring groups. In order to see what effect might be expected for this from the solid geometry, a structural analysis of ring-methyl groups was undertaken as follows.

Centroids were calculated for all four aryl rings using Mercury crystallographic software and distances of the C atoms in all isopropyl CH₃ groups to the centroids of the aryl rings were measured. To facilitate discussion, the aryl rings are divided into two groups: the “perpendicular” rings (blue centroids) and the “coplanar” rings (pink centroids) (Figure 3.8).

Table 3.4. Summary of chemical shift correlation of isopropyl CH₃ and CH signals from the COSY proton NMR spectrum of Dipp₄P₂

CH ₃	CH
0.36	4.07
1.41	
0.46	3.93
1.46	
0.7	4.29
1.38	
0.84	5.24
1.47	

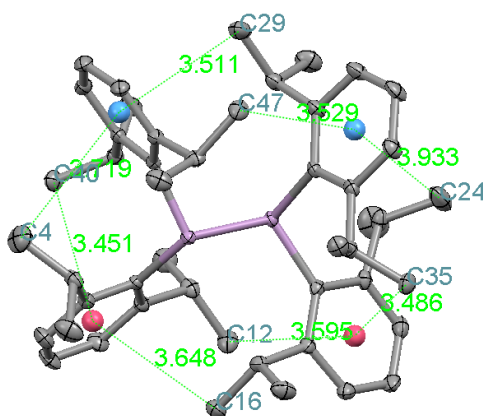


Figure 3.8. Centroid calculations for Dipp₄P₂ (pink centroid for coplanar planes and blue centroid for perpendicular planes) for distances to the nearest methyl group C atom.

Table 3.5 summarizes the results of these measurements. It can be hypothesized that CH₃ groups on perpendicular rings have closer aromatic contacts in comparison with CH₃ groups in coplanar rings and therefore the most shielded peaks at low frequency in the ¹H NMR spectrum are related to those that have closer contacts with aryl rings. The results fit well with the spectra, since eight of the sixteen methyl groups are found to be close to aryl ring centroids, while the remaining eight are far away on the periphery of the molecule. Moreover, the results naturally fall into groups, so that if allowance is made for vibrations, four sets of distances can be distinguished from among the eight measurements (as shown by the dividing lines in Table 3.5).

Table 3.5. Distances of CH₃ from perpendicular and coplanar Dipp rings

Distance of CH ₃ groups from coplanar rings	Assigned CH ₃	Distance of CH ₃ groups from perpendicular rings	Assigned CH ₃
3.59	C ₁₂	3.45	C ₄₀
3.64	C ₁₆	3.48	C ₃₅
3.71	C ₄	3.51	C ₂₉
3.93	C ₂₄	3.52	C ₄₇

From Table 3.4, it is possible to correlate a pair of close methyl groups that are the least affected by ring-shielding, but belong to the two isopropyl groups which show methine coupling to ³¹P (doublet coupling, i.e. each to one phosphorus atom). The coupling effect was proven by comparing to the ³¹P{¹H} NMR spectrum which collapses to a normal septet.

The Heteronuclear Single Quantum Coherence (HSQC) experiment is used to find a connection between the protons and correlates chemical shifts of directly bound carbon. By considering the C₂ symmetry, symmetry related atoms and groups have been assigned. Finally, CH₃ and CH groups in a unique half of the molecule are labeled. For this study, two sets of rings

are considered: those that are perpendicular and those that are parallel to the P–P bond. Also, on each Dipp ring two sets of isopropyl groups are closer to the phosphorus and two further from phosphorus. Moreover, on each isopropyl group, the CH₃ group which is “inner” and hence close to the neighboring rings, and those that are “outer” are distinguished. The averages of P–C distances for the inner CH₃ are calculated by averaging the numbers by the pairwise groupings in Table 3.5 and for CH by averaging the distance between the methine carbon and phosphorus. From all these considerations, a full assignment of all the proton and carbon signals in the spectra of Dipp₄P₂ has been determined as presented in Table 3.6 and Table 3.7.

Table 3.6. ¹H and ¹³C NMR data for Dipp₄P₂ at room temperature

	<i>C</i> ₂ symmetry related carbons	Average of P–C distance	$\delta^1\text{H}$	$\delta^{13}\text{C}$	<i>J</i> _{HH} /Hz	<i>J</i> _{HP} /Hz
Perpendicular ring						
Close ⁱ Pr						
Inner CH ₃	C ₂₉ (C ₄₇)	3.52	0.46	24.69	6.6	
Outer CH ₃	C ₂₈ (C ₄₈)		1.46	24.53	6.6	
CH	C ₂₇ (C ₄₆)	3.11	3.93	33.41	6.9	
Far ⁱ Pr						
Inner CH ₃	C ₃₅ (C ₄₀)	3.46	0.36	23.51	6.9	
Outer CH ₃	C ₃₆ (C ₄₁)		1.41	24.48	6.9	
CH	C ₃₄ (C ₃₉)	3.38	4.07	33.25	6.9	
Parallel ring						
Close ⁱ Pr						
Inner CH ₃	C ₂₄ (C ₄)	3.82	0.84	26.19	6.3	
Outer CH ₃	C ₂₃ (C ₅)		1.47	25.98	6.3	
CH	C ₂₂ (C ₃)	2.97	5.24	32.80	6.3	3.3
Far ⁱ Pr						
Inner CH ₃	C ₁₆ (C ₁₂)	3.62	0.70	23.14	6.6	
Outer CH ₃	C ₁₇ (C ₁₁)		1.38	24.91	6.6	
CH	C ₁₅ (C ₁₀)	3.56	4.29	32.17	6.6	

Although there is no proof for these assignments, a fully self-consistent set of predictions was obtained by using the average distances of the methyl carbons to centroids of the rings, which matched very well with COSY and HSQC spectra. The discussion can be started by looking at the proton chemical shifts of methyl groups which are strongly deshielded versus the 1.2-1.3 ppm chemical shift for isopropyl methyl groups on unperturbed phenyl rings attached to trivalent phosphorus (obtained from the shifts in isopropylbenzene and 1,3,5-triisopropylbenzene). The best explanation for these deshielded chemical shifts is the known phenomenon of “above-plane anisotropic ring effect” (sometimes called the “paraphane effect”). When benzene is placed in a magnetic field, the π electrons in the aromatic ring system are induced to circulate around the ring. This circulation is called a ring current. The moving electrons generate a magnetic field, the magnetic field is large enough to influence the shielding or deshielding of the benzene ring protons.²⁴ Those protons placed on the benzene periphery will be deshielded under the effect of this phenomenon and this is exactly what has happened in case of the protons in CH groups in Dipp_4P_2 .

The most deshielded methine is C_{22} (along with its symmetry partner C_3) which is located in the parallel ring and shows a chemical shift at 5.24 ppm. The observed coupling of the ^1Pr CH for C_{22} (chemical shift = 5.24 ppm, $J(\text{HH}) = 6.3$ Hz, $J(\text{PH}) = 3.3$ Hz) is substantiated by the HOMO which shows an antibonding interaction between this CH and the P electron density and probably mediates the dipolar (through-space) coupling (Figure 3.9).

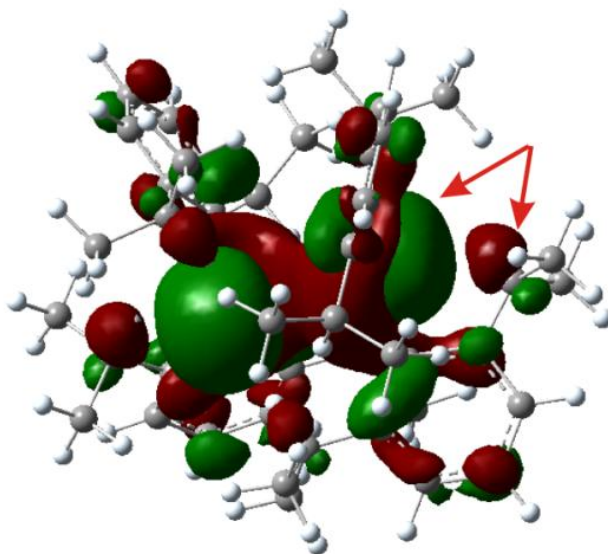


Figure 3.9. HOMO and C₂₂ CH interaction with phosphorus

For the aromatic NMR signals, correlation spectroscopy (COSY), heteronuclear multiple-bond correlation spectroscopy (HMBC) and heteronuclear single-quantum correlation spectroscopy (HSQC) have been used for assigning protons in *meta* and *para* positions and carbons have been assigned based on the larger coupling to ³¹P on the perpendicular ring. For the proton signals, triplets for *para* positions and doublets for *meta* were expected. *Para* protons integrating to 4H are observed with some overlapping in the expected three lines (“tent” shapes) with long range correlation to the proton on methyl groups. The *meta* signals are further split due to coupling to phosphorus and four doublets-of-doublets with integration to 8H are observed. The remaining carbons on the benzene rings are assigned using correlations seen in HMBC spectra.

These spectral results are fully consistent with an antiperiplanar conformation in solution that is closely related to the twisted *anti* conformation observed in the crystal structure. This is not the case for all diphosphines. For example tetramesityldiphosphine has a *gauche* conformation in solution at low temperature while it crystallizes as *anti* in the solid state.²³ DFT calculations give strong evidence that the *gauche* isomer is probably a feasible option for Mes₄P₂

but not for Dipp₄P₂. In the gauche conformation, calculations show the molecule is distorted significantly, with the two “co-planar” Dipp ⁱPr groups strongly bent out of the plane. Thus, the molecule is significantly squeezed. This geometry is 69.9 kJ mol⁻¹ higher in energy than the optimized *anti* isomer which supports the NMR evidence for an *anti* conformation of this molecule in solution.

Table 3.7. ¹H and ¹³C NMR data for aromatic atoms in Dipp₄P₂

	Aromatic carbons	$\delta^1\text{H}$	$\delta^{13}\text{C}$	J_{HH}/Hz	J_{HP}/Hz	J_{CP}/Hz
Perpendicular ring						
Meta CH	C ₃₀ (C ₄₄)	7.11	126.82	6.3	1.5	
	C ₃₂ (C ₄₂)	7.06	124.91	6.9	2.4	4
Para CH	C ₃₁ (C ₄₃)	7.18	130.58	7.1		
Remaining carbons	C ₂₅ (C ₃₇)		135.49			19
	C ₂₆ (C ₄₅)		154.82			17
	C ₃₃ (C ₃₈)		156.22			19
Parallel ring						
Meta CH	C ₁₈ (C ₈)	7.06	124.91	6.9	2.4	3
	C ₂₀ (C ₆)	7.05	127.21	6.9	3.7	
Para CH	C ₁₉ (C ₇)	7.22	129.62	7.2		
Remaining carbons	C ₁₃ (C ₁)		134.72			14
	C ₁₄ (C ₉)		154.82			2
	C ₂₁ (C ₂)		155.36			4

Additionally, it is important to know that in this case due to the molecular C_2 symmetry, each phosphorus is chiral, leading to the RR and SS enantiomers represented in Figure 3.10 as idealized Newman projections down the P–P bond. (For convenience, the Dipp group with its plane approximately parallel (B) to the P–P bond is arbitrarily given lower priority than the other). Interconversion of the enantiomers does not require complete rotation of the Dipp groups, which would restore effective C_{2h} symmetry for the molecule. Instead, it could be achieved by a

“turnstile” correlated librational motion of all four Dipp groups. In this process, the two types of ring interchange their environments. Just such a mechanism has been postulated from an analysis of the ^1H NMR spectra of Mes_4P_2 ,²³ a molecule which lacks the stereochemically sensitive isopropyl marker groups. Thus, McFarlane’s conclusions are derived from measuring *three* rather than two different rate constants from the slow-exchange limit spectra for this molecule. It is evident, however, that at RT Dipp_4P_2 is already in the slow-exchange limit because the “turnstile” mechanism proposed for Mes_4P_2 would reduce the number of different methyl groups from eight kinds to four. Hence, it can be concluded that Dipp_4P_2 exists as a racemic mixture of non-interconverting enantiomers in solution. Both enantiomers are of course present in the crystal structure by virtue of the inversion symmetry within the unit cells of $P2_1/n$.

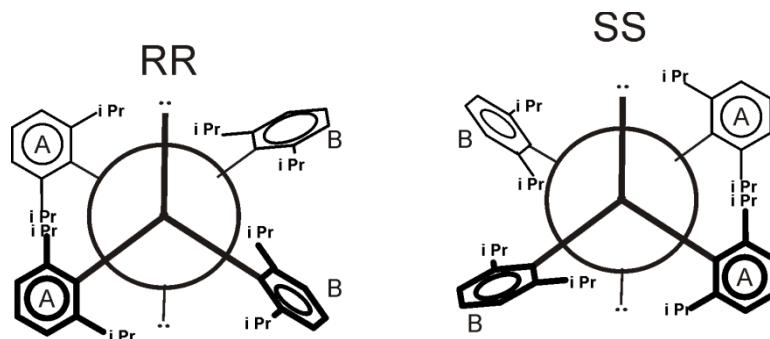


Figure 3.10. Newman Projections down the P–P bond of SS and RR C_2 symmetric antiperiplanar rotamers of Dipp_4P_2

3.3.1 Results of cyclic voltammetry of Dipp_4P_2

A voltammogram of Dipp_4P_2 on a GC electrode in CH_2Cl_2 solvent with 0.4 M $[\text{nBu}_4\text{N}][\text{PF}_6]$ as the supporting electrolyte shows two oxidation processes over scan rates of 0.05–0.8 Vs^{-1} and temperatures of 21 ± 2 $^\circ\text{C}$, with the first oxidation expressing close to Nernstian behaviour over all scan rates. The cobaltocene ($\text{Cc}^{+/0}$) redox couple has been used as a reference potential while quoting data with respect to $E_{\text{Fc}^{+}/0}^\circ$, the formal potential for the Fc/Fc^+

as recommended by IUPAC.²⁵ A representative voltammogram is shown in Figure 3.11 for a scan rate of 0.2 mVs^{-1} and data for both oxidation processes at all experimental scan rates are summarized in Table 3.8.

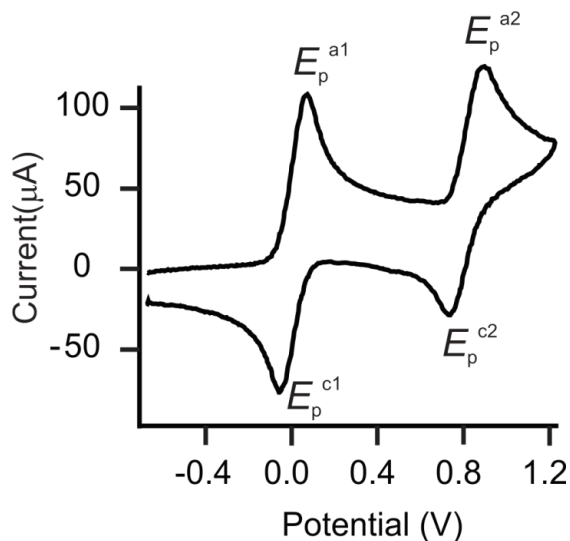


Figure 3.11. Cyclic voltammetry of Dipp₄P₂ (5 mM) in CH₂Cl₂ solution containing 0.4 M [n-Bu₄N][PF₆] under an atmosphere of dry Ar at $v=0.2 \text{ Vs}^{-1}$ on a GC electrode at 20 °C.

Potentials, E_f° , for the one electron transfers occurring over the potential range $\sim -0.4\text{V}$ to ~ 1.2 vs $E_{\text{Fc}^+/0}^\circ$ were obtained by averaging the corresponding cathodic and anodic peak potentials, E_p^{a1} and E_p^{c1} , to obtain the "midpoint" potential, E_m , which is assumed to be a good approximation of the standard potential, E_f° . Considering characteristics of the voltammogram over all the experimental scan rates implies that a quasi-reversible one-electron process is the best definition for the first oxidation process under conditions of cyclic voltammetry. Counting behaviors such as the separation of the forward and reverse peaks (ΔE_p) is larger than the value of $56/n \text{ mV}$ associated with a reversible process at 25 °C, ΔE_p increases with increasing scan rate and also the magnitude of ratio of the peak currents $|I_{\text{pox}}/I_{\text{pred}}|$ remains equal to unity, together support the hypothesis of for a quasi-reversible system.

Table 3.8. Summary of cyclic voltammetry data obtained for both oxidation process of**Dipp₄P₂ at GC electrode and T = 22 °C.^a**

v(mVS ⁻¹)	E_p^{a1} (V)	E_p^{c1} (V)	${}^bE_{m1} \cong E_{f1}^o$ (V)	${}^c\Delta E_{p1}$ (mV)	E_p^{a2} (V)	E_p^{c2} (V)	$E_{m2} \cong E_{f2}^o$	ΔE_{p2} (mV)
50	0.034	-0.061	-0.013	95	0.853	–	–	–
100	0.039	-0.062	-0.011	102	0.876	0.750	0.813	126
200	0.050	-0.073	-0.011	123	0.885	0.708	0.796	177
400	0.068	-0.087	-0.009	155	0.928	0.682	0.805	246
800	0.094	-0.095	-0.0005	190	0.972	0.677	0.825	295

Obtained in CH₂Cl₂ solution containing 0.4 M [ⁿBu₄N][PF₆] measured against Cc⁺⁰ and ^a expressed vs $E_{Fc+/0}^o$. ${}^bE_m = [E_p^{a1} + E_p^{c1}]/2 \cong E_f^o$. ${}^c\Delta E_p = E_p^{a1} - E_p^{c1}$. E_p^{a1} = first oxidative peak potential. E_p^{c1} = first reductive peak. E_p^{a2} = second oxidative peak potential. E_p^{c2} = second reductive peak.

The second oxidation displayed at potentials that are more positive, showed no return waves over scan rates of 50–100 mVs⁻¹ and is therefore fully irreversible in this range but quasi-reversible at higher scan rates. Meanwhile, it is obvious that reversibility of the second oxidation is less than first oxidation, which is very close to a reversible process. In the chemical sense, it can be claimed that the first oxidation is chemically reversible. One of the most important points in this study was that by going to the second oxidation, the peak currents of the first oxidation are not affected significantly, which shows the stability of the dication which is likely to be chemically reversible but electrochemically irreversible by this evidence. This enhanced stability of the radical cation is linked to the superior steric shielding afforded by the large enveloping Dipp groups that provide adequate steric shielding for the phosphorus lone pair. On the other hand, it can be concluded that by removing the second electron, a major change in molecular structure and/or geometry has occurred that would then seem to imply electrochemical irreversibility for the dication. This can be proved by both the electrochemical data (Table 3.8 and Table 3.9) and the voltammogram in Figure 3.11 and Figure 3.12. There is no remarkable

change in peak current and peak potential of first oxidation by going further to the second oxidation on the lower scan rates.

Table 3.9. Summary of cyclic voltammetry data obtained for first oxidation process of Dipp₄P₂ at GC electrode and T = 22 °C.^a

$v(\text{mVS}^{-1})$	$E_p^{a1}(\text{V})$	$E_p^{c1}(\text{V})$	${}^b E_{m1} \cong E_{f1}^o(\text{V})$	${}^c \Delta E_{p1}(\text{mV})$	${}^d I_p^{\text{ox}}/I_p^{\text{red}}(\mu\text{A})$
50	0.050	-0.049	0.0005	100	0.92
100	0.052	-0.071	-0.009	124	0.84
200	0.065	-0.061	0.002	127	0.82
400	0.065	-0.085	-0.010	150	0.90
800	0.086	-0.102	-0.008	188	0.93

Obtained in CH₂Cl₂ solution containing 0.4 M [ⁿBu₄N][PF₆] measured against Cc⁺⁰ and ^a expressed vs $E_{\text{Fc}+/0}^o$. ^b $E_m = [E_p^{a1} + E_p^{c1}]/2 \cong E_f^o$. ^c $\Delta E_p = E_p^{a1} - E_p^{c1}$. ^d limiting current ratio in μA . E_p^{a1} = first oxidative peak potential. E_p^{c1} = first reductive peak.

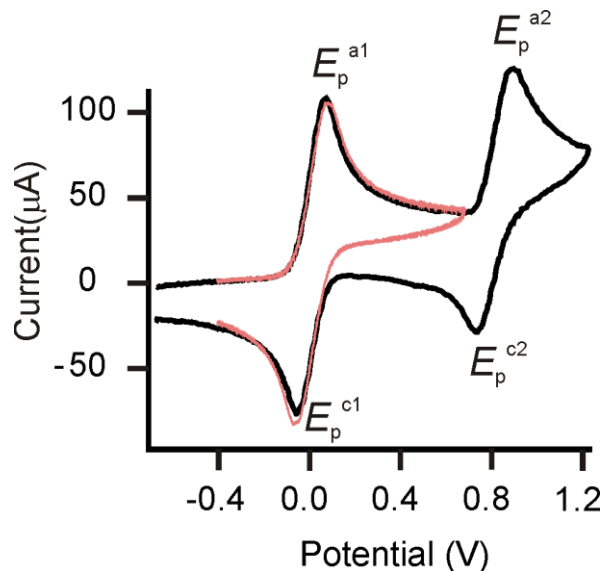


Figure 3.12. Cyclic voltammetry of Dipp₄P₂ (5 mM) in CH₂Cl₂ solution containing 0.4 M [ⁿBu₄N][PF₆] under an atmosphere of dry Ar at $v = 0.2 \text{ Vs}^{-1}$ on a GC electrode at 20 °C: (a) through the first oxidation process (pink line); (b) through the first and second oxidation processes (black line)

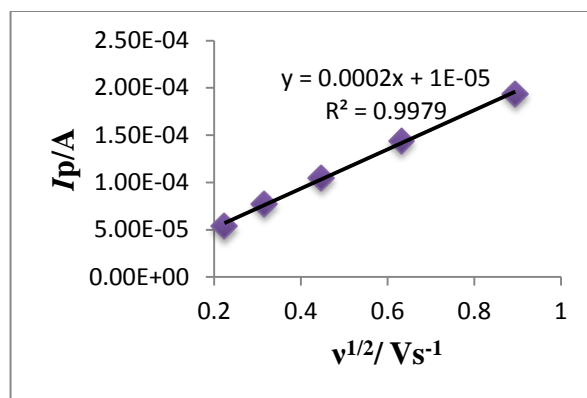


Figure 3.13. Plots of the I_p vs. $v^{1/2}$ obtained for the first Dipp₄P₂ oxidation process in CH₂Cl₂ at GC working electrodes.

The almost linear plots of the I_p vs. $v^{1/2}$ obtained for the first and second Dipp₄P₂ oxidation process in CH₂Cl₂ at GC working electrodes imply that the mass transport process at the peak potential is controlled by diffusion (Figure 3.13). From the Randles-Sevcik relationship, an estimation of the diffusion coefficient was obtained from a straight-line fit to the I_p vs. $v^{1/2}$ plots. The peak current of a CV wave under Nernstian conditions is given by Eqn.1.²⁶

$$I_p = (2.69 \times 10^5) n^3 A D^{1/2} v^{1/2} C \quad \text{Eq.1}$$

Here I_p is the peak current, n is the number of electrons and is taken to be 1.0, A the electrode area (in cm²), D the diffusion coefficient of Dipp₄P₂ (in cm²/s), and v the potential scan rate (in V/s), C is the concentration of Dipp₄P₂ in the bulk solution (in mol/cm³). Thus, $I_p \propto D^{1/2}$ and an estimate for the diffusion coefficient is $5.96 \times 10^{-6} \text{ cm}^2 \text{ s}^{-1}$ in CH₂Cl₂/[ⁿBu₄N][PF₆]. This value is in reasonable agreement with the values for D measured for dilute solutions of Dipp₄P₂ in CH₂Cl₂ by RDE. E_{rev}E_{irrev}C mechanism is the best prediction for this system since it has two electrochemical oxidation processes and one chemical reaction after removing the second electron. The chemical step could be simply a re-arrangement of the structure as will be

discussed in Section 2.7. Cyclic voltammetry of Dipp₄P₂ in CH₃CN was frustrated by the low solubility of this compound in CH₃CN even with heating the solution.

3.3.2 Results of cyclic voltammetry of ^tBu₄P₂

^tBu₄P₂ was studied by cyclic voltammetry (CV) in CH₂Cl₂ over scan rates of 0.05–0.8 Vs⁻¹ and temperatures of 20 ± 2 °C. Data for the CV responses of ^tBu₄P₂ in all scan rates are reported in Table 3.10 with potentials quoted relative to Fc⁺⁰. The cobaltocene (Cc⁺⁰) redox couple has been used as a reference potential while quoting data in different scan rates with respect to E^o_{Fc+/0}, the formal potential for the Fc/Fc⁺ as recommended by IUPAC.²⁷ Representative CVs of ^tBu₄P₂ in CH₂Cl₂ at a scan rate of 200 mV s⁻¹ are shown in Figure 3.14. One close to quasi-reversible oxidation process appears upon sweeping the potential and the second peak is probably due to oxide impurities resulting from air oxidation of ^tBu₄P₂. The I_p^{ox}/I_p^{red} ratios for the major processes are much less than unity but approach unity as the scan rate is increased.

Table 3.10. Summary of cyclic voltammetry data obtained for oxidation process of ^tBu₄P₂ at

GC electrode and T = 22 °C.^a

v(mVs ⁻¹)	E _p ^{al} (V)	E _p ^{cl} (V)	^b E _{m1} ≅ E ^o _{f1} (V)	^c ΔE _{p1} (mV)	^d I _p ^{ox} /I _p ^{red} (μA)
50	0.375	0.305	0.3400	70	0.34
100	0.380	0.310	0.3450	70	0.47
200	0.396	0.295	0.3455	101	0.47
400	0.410	0.300	0.3550	110	0.50
800	0.440	0.300	0.3700	140	0.63

Obtained in CH₂Cl₂ solution containing 0.4 M [ⁿBu₄N][PF₆] measured against Cc⁺⁰ and ^a expressed vs E^o_{Fc+/0}. ^bE_m = [E_p^{al} + E_p^{cl}]/2 ≅ E^o_f. ^cΔE_p = E_p^{al} - E_p^{cl}. ^d limiting current ratio in μA. E_p^{al} = first oxidative peak potential. E_p^{cl} = second reductive peak.

An increase in the uncompensated resistance in CH₂Cl₂ at faster scan rates (>1 V s⁻¹) resulted in a broadening of the peaks. The only data reported for CV of ^tBu₄P₂ is the paper by Niemann which has a good agreement with my data if considering their voltammogram but the data on their Table is not the same with even their own CV results.²⁸

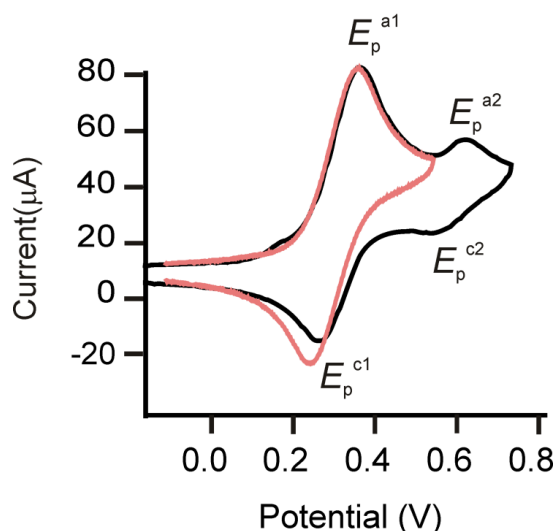


Figure 3.14. Cyclic voltammetry of ^tBu₄P₂ (5 mM) in CH₂Cl₂ solution containing 0.4 M [ⁿBu₄N][PF₆] under an atmosphere of dry Ar at $v=0.2 \text{ Vs}^{-1}$ on a GC electrode at 20 °C.

3.3.3 Determination of the diffusion coefficients for Dipp₄P₂

RDE measurements on solutions of Dipp₄P₂ in CH₂Cl₂ were undertaken in order to determine the diffusion coefficient D . CV measurements (eqn.1) provided estimates of $D = 5.956 \times 10^{-6} \text{ cm}^2 \text{ s}^{-1}$ in CH₂Cl₂/[ⁿBu₄N][PF₆]. For RDE measurements, determination of the diffusion coefficient made use of the Levich eqn.2,²⁹ using a value for the kinematic viscosity ν in CH₂Cl₂ at 20 °C of $0.003318 \text{ cm}^2 \text{ s}^{-1}$.

$$I_l = 0.620nFA C^0 D^{2/3} \nu^{-1/6} \omega^{1/2} \quad \text{Eqn.2}$$

Where C^0 = bulk solution concentration, mol cm⁻³, I_l = limiting current, A, D is the diffusion coefficient of species A (cm² s⁻¹), ν = kinematic viscosity of the fluid, cm² s⁻¹, ω = angular disk

velocity of the disk, rad s^{-1} . (Kinematic viscosity is defined as the viscosity of the solution divided by the density in $\text{cm}^2 \text{s}^{-1}$ but in practice, the viscosity of the pure solvent is often used rather than obtaining viscosity measurements on the actual solvent/analyte/electrolyte mixture).

Table 3.11. Limiting current values for solution of Dipp₄P₂ in CH₂Cl₂ in different concentrations

RPM	I_d (2.58 mM)	I_d (5.59 mM)	I_d (4.01 mM)
2250	3.4840E-04	6.6010E-04	4.4810E-04
2000	3.3070E-04	6.1499E-04	4.1620E-04
1750	2.9891E-04	5.7800E-04	3.9210E-04
1500	2.7593E-04	5.1853E-04	3.5718E-04
1250	2.4412E-04	4.5690E-04	3.2391E-04
1000	2.3585E-04	3.8613E-04	2.9189E-04

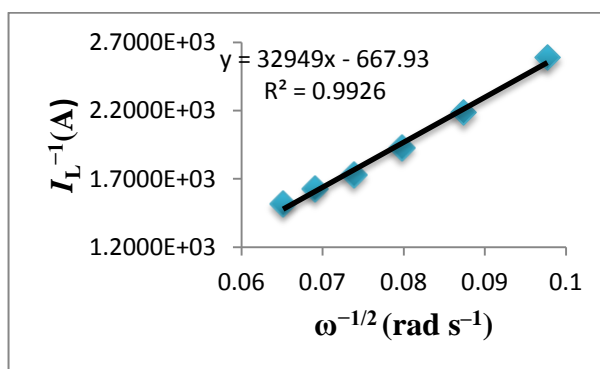


Figure 3.15. Plots of the Levich current vs the square root of the rotational velocity of 5.59 mM solution of Dipp₄P₂ in CH₂Cl₂ (0.1 M [ⁿBu₄N][PF₆]).

Rotation rates between 1000 – 2250 rpm were applied over a potential range of –0.3 to 0.8 V to 2.58 mM and over the range of –0.3 to 0.6 to 5.59 mM and over the range of –0.3 to 0.5 to 4.011 mM solutions of Dipp₄P₂ in CH₂Cl₂. Plots of the Levich current or limiting current (I_L^{-1}) vs the square root of the rotational velocity ($\omega^{-1/2}$) yielded straight lines in each case with a slope $= (0.62nFACv^{-1/6}D^{2/3})^{-1}$ (Figure 3.15).

Using eqn.2 yielded D values which were in reasonable agreement with the values obtained from CV measurements using eqn.1 and are listed in Table 3.11. Deviations in the values from the two different methods likely stem from minor inaccuracies in the electrode areas and solution concentrations. For this reason, different concentrations have been measured for RDE calculations (Table 3.12). The RDE traces show the voltammograms for 5.5 mM of $\text{Dipp}_4\text{P}_2^{++}$ at a GC electrode in CH_2Cl_2 (0.1 M $[\text{nBu}_4\text{N}][\text{PF}_6]$) at different rotation speeds (Figure 3.16). The RDE traces show the voltammograms for 5.5 mM of $\text{Dipp}_4\text{P}_2^{++}$ at a GC electrode in CH_2Cl_2 (0.1 M $[\text{nBu}_4\text{N}][\text{PF}_6]$) at different rotation speeds (Figure 3.16).

Table 3.12. Diffusion coefficient values for solution of Dipp_4P_2 in CH_2Cl_2

Concentration of Dipp_4P_2 solution (mM)	$D(10^{-6} \text{ cm}^2 \text{ s}^{-1})$
2.58	3.25
5.59	2.59
4.01	3.60

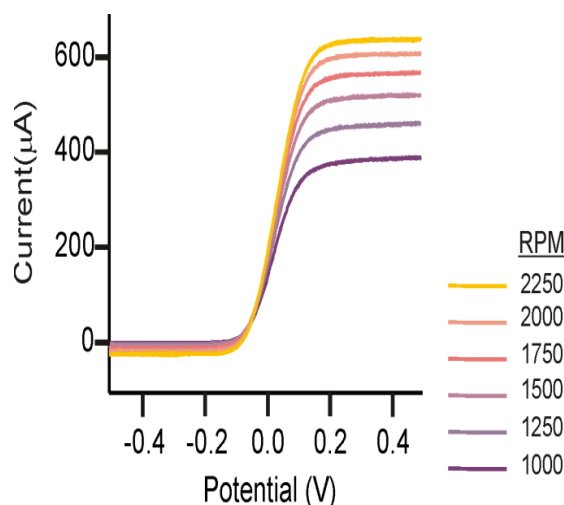


Figure 3.16. RDE curves at a GC electrode when $[\text{Dipp}_4\text{P}_2]^{++}$ is generated from 5.5 mM Dipp_4P_2 in CH_2Cl_2 (0.1 M $[\text{nBu}_4\text{N}][\text{PF}_6]$) at different rotation speeds.

3.4 EPR spectroscopy

3.4.1 SEEPR investigation of Dipp_4P_2

In situ electrochemical EPR experiments were conducted in CH_2Cl_2 for Dipp_4P_2 (temperatures were varied between 0 and 20 °C) utilizing the low-temperature SEEPR cell and a modified version of the gold-micromesh working electrode first described by Neudeck and Kress (see Section 2.3.1).³⁰ Strong solution-phase spectra were obtained with large hyperfine splitting showing four lines of approximately equal intensity as shown in Figure 3.17(a). Simulations of the spectra were undertaken with the Bruker Simfonia software that exhibit line positions that agree well with values deduced from the experimental spectra. The simulations included coupling to two phosphorus nuclei. In a first-order approximation, coupling to two equivalent phosphorus nuclei yields a three-line (1:2:1) EPR spectrum as shown in Figure 3.17(b), whereas the experimental results show apparent further splitting of the central line (integrated intensity of this doublet is still 2).

The four-line patterns in spectra of all tetraaryldiphosphines are caused by the large magnitude of the phosphorus hyperfine splitting, the so-called "higher-order-splitting" effect.³¹ Hence, the $M_I = 0$ transition appears as a doublet corresponding to $I = 0$ or 1, that is, to the singlet or the triplet state, respectively, of the two coupled phosphorus nuclei. In fact, all lines except one from the central pair have been shifted towards lower field from the first order positions (Figure 3.18). Higher-order splitting occurs whenever the energy of the hyperfine interaction approaches (within about 1% to be visible) that of the Zeeman interaction. A reasonable fit to the experimental results with their higher-order splitting pattern could be achieved using the third-order perturbation theory incorporated in Simfonia³² and the calculated values were very close to the experimental values (Figure 3.17). Such higher order perturbation theory is essential to

capture the “unusual” effect of the split central lines. The agreement is excellent but not perfect because firstly, the experimental spectrum has a field-dependent line-width effect. Simfonia unfortunately cannot simulate this when there are two coupled nuclei, although it can do this for one nucleus.

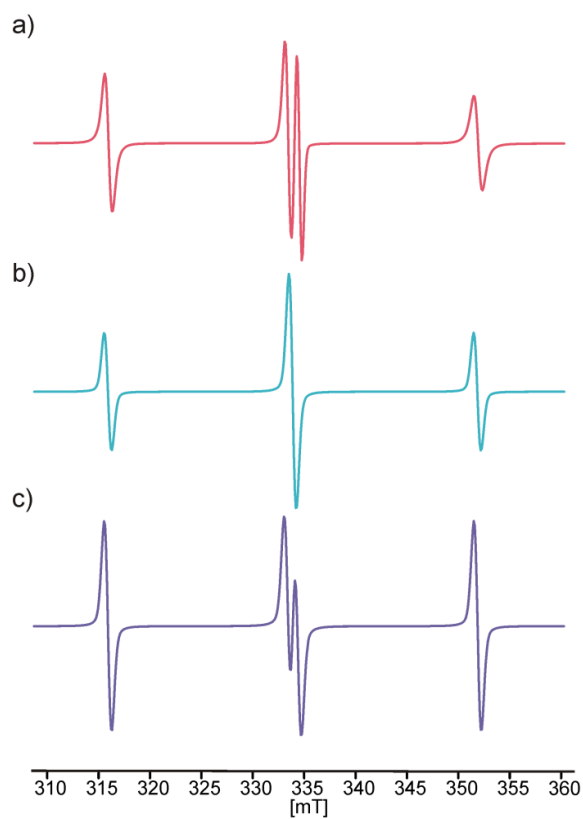


Figure 3.17. (a) Experimental EPR spectrum obtained after electrolyses of a 5 mM solution of $[\text{Dipp}_4\text{P}_2]^{++}$ at a gold mesh electrode at room temperature in CH_2Cl_2 (0.4 M $[\text{Bu}_4\text{N}][\text{PF}_6]$) and modulation frequency 100 kHz, modulation amplitude = 0.5 mT, and (b) first derivative and (c) third derivative simulations obtained using Bruker Simfonia and the parameters listed in Table 3.13.

Secondly, the simulation does not get the relative intensity of the central multiplet correct. However, there is a 1986 paper by Tordo that developed an equation to show the fact that the line

width variation in R_4P_2 radical cations are temperature dependent and also it depends on dihedral angles.³³ Thus, although it is tempting to use the dramatic difference in relative line-widths between $Dipp_4P_2^{+}$ and tetrakis(2,4,6-triethylphenyl)diphosphine radical (see Figure 1.2) as an indication that the two radical cations have quite different conformations in solution (Tordo thinks the latter is gauche), the significant differences in conditions, particular of solvent between butyronitrile and dichloromethane with quite different viscosities should also be considered.

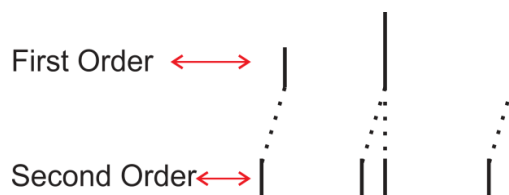


Figure 3.18. First order and second order splitting of a 1:2:1 triplet arising from two equivalent nuclei each with $I=1/2$

Table 3.13. Experimental EPR data for the $Dipp_4P_2^{+}$

g value	HFS (mT)	Temp (°C)
2.00862	17.97	0
2.00862	18.04	10
2.00861	18.13	20

In addition, the large phosphorus splitting observed for $Dipp_4P_2^{+}$ clearly indicates that the phosphorus centers are considerably pyramidal. The experimental HFS constants, line widths, and g values for experimental radicals in different temperatures are summarized in Table 3.13. The most intriguing feature of these spectra is the anomalous line width variation across the multiplet. As a result there is no distinct change in the overall shape of the spectra with temperature and the enhanced stability of the radical cation has been attributed to the superior steric shielding afforded by the large Dipp groups and this is what is evidenced in CV studies.

3.4.2 EPR investigation of Dipp₄P₂ with chemical oxidation

Chemical oxidation of Dipp₄P₂ with AgPF₆ has been carried in a T-cell in order to be able to measure the spectrum of the radical cation in frozen solution (a powder-pattern spectrum). The EPR flat cell used for the SEEPR investigation cannot be frozen. The EPR cell was filled with solutions of the [Dipp₄P₂⁺] X⁻ salts in CH₂Cl₂ (see Section 6.3.4). EPR studies started at 0 °C and the temperature was reduced by 10 degree steps for further spectra down to -100 °C which is below the freezing point of the CH₂Cl₂.

Unlike the more straightforward analysis of fluid solution EPR spectra, the interpretation of powder EPR spectra is more demanding, and often complicated by the presence of different paramagnetic active sites, distribution of *g* and *A* values, loss of spectral resolution and large line-widths. The shape of the solid-state EPR spectrum depends on the relative orientation of the applied magnetic field (*B*) with respect to the orientation of the paramagnetic species itself. The symmetry of the local site at the paramagnetic center is therefore directly reflected in the final profile of the resulting EPR spectrum. Three limiting cases are used to define the local symmetry in a paramagnetic site: 1.) Cubic or isotropic ($g_{xx} = g_{yy} = g_{zz}$ and $A_{xx} = A_{yy} = A_{zz}$) for which the properties of the system are independent of orientation in a magnetic field. 2.) Axial in which anisotropy will be observed in the EPR spectrum because the resonance field will be different when *B* is aligned along the unique axis (*Z*) compared to the observed case when *B* is aligned in the XY plane perpendicular to the applied field and rotational symmetry about a unique axis is present ($g_{xx} = g_{yy} \neq g_{zz}$ and $A_{xx} = A_{yy} \neq A_{zz}$). In this system g_{xx} , g_{yy} and A_{xx} , A_{yy} are known as the perpendicular tensor components and g_{zz} and A_{zz} as the parallel tensor components. 3.) Rhombic in which anisotropy occurs along all three directions and three unequal values of the *g* factor and *A* will occur ($g_{xx} \neq g_{yy} \neq g_{zz}$ and $A_{xx} \neq A_{yy} \neq A_{zz}$).^{34,35}

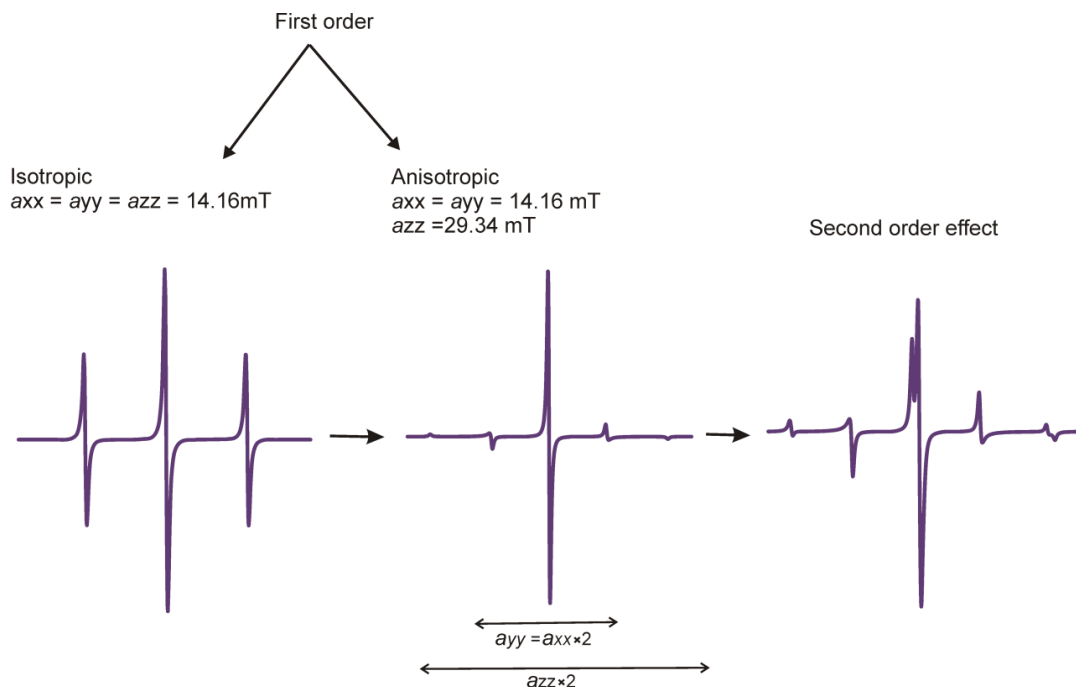


Figure 3.19. Summary of EPR Powder pattern explanation using three levels of simulation

The EPR spectrum of Dipp_4P_2 will be complicated by a variety of factors which are addressed by three simulated spectra showing contributions to the spectrum in three steps from left to right (Figure 3.19). At left is the predicted spectrum when the hyperfine tensor is isotropic (i.e. cubic field). Introducing significant A anisotropy ($A_{xx} = A_{yy} \neq A_{zz}$) causes the three lines of the isotropic spectrum to change to five lines in the axial anisotropic system (middle spectrum in Figure 3.19). The third simulation includes the “higher-order-splitting” effect which was mentioned for the solution spectra in Section 3.4.1 and which applies equally to powder spectra whenever the hyperfine splitting exceeds 10-12 mT in X-band spectra.^{31,35}

Indeed, in the frozen glass, a characteristic axially symmetric powder pattern was obtained (Figure 3.20) with parallel and perpendicular HFS tensor components of 29.34 and 14.16 mT and the expected higher-order splitting. In addition to the effects discussed above, there is also a very small asymmetry in the g tensor from axial g_{\perp} and g_{\parallel} terms. The parallel and perpendicular g tensors are, however, almost the same, so that the EPR spectrum is close to a g -

isotropic system. The small deviations cause additional splitting of the second and last lines in the experimental spectra. Figure 3.20 shows the experimental and simulated spectra of Dipp_4P_2 cation in CH_2Cl_2 in frozen solution with a very small deviation in g tensors $g_{\parallel} = 2.0085$; $g_{\perp} = 2.0045$ mT. The simulation captures most of the features of the measured spectrum.

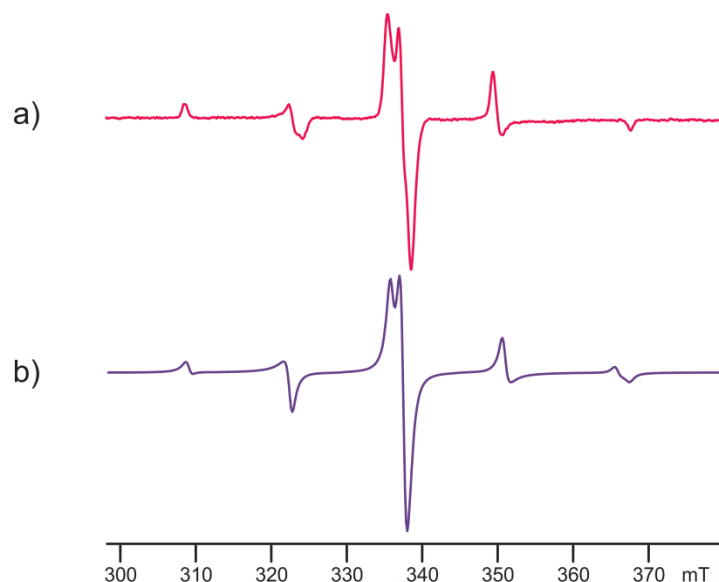


Figure 3.20. (a) Experimental and (b) simulated solid state EPR spectra of $\text{Dipp}_4\text{P}_2^{+\bullet}$

EPR spectra of dilute solutions of such chemically generated radicals are identical to those prepared by electrochemical methods. The isotropic liquid spectra show the presence of four lines with a hyperfine coupling to ^{31}P of 18.06 mT (Table 3.14). The peak-to-peak line widths (low field lines) of the spectral lines was found between 0.7 and 1 mT. As expected, line broadening happens upon decreasing the temperature and this is due to the slow tumbling effect which becomes more obvious at low temperatures and will be discussed in the next chapter since simulation of this effect in diphosphines was not possible.

Table 3.14. Effect of temperature changes on experimental EPR Data for $\text{Dipp}_4\text{P}_2^{+}$

Line width (mT) ^a	HFS (mT)	Modulation amplitude (mT)	Temp (°C)
0.68	17.98	0.5	20
0.67	18.07	0.1	0
0.71	18.06	0.2	-10
0.77	18.06	0.3	-20
0.82	18.06	0.3	-30
0.97	18.06	0.4	-40

^aPeak to peak low field line width from dispersion signal.

Two different approaches have been taken in this study: one to observe the effect of temperature changes on shape of the spectra and the other the effect of modulation amplitude at room temperature with the goal of accurate line width measurements (Table 3.15). Increasing the modulation amplitude leads eventually to an apparent increase in the line width. It is important to choose the appropriate modulation amplitude, frequency, and time constant. All three variables can distort EPR signals and make interpretation of results difficult.

Table 3.15. Effect of modulation amplitude on experimental EPR data for the $\text{Dipp}_4\text{P}_2^{+}$

Line width (mT) ^a	HFS (mT)	Modulation amplitude (G)
0.68	17.98	5
0.66	17.98	4
0.65	17.98	3
0.61	17.98	2
0.61	18.07	1
0.61	18.07	0.5
0.61	17.99	0.1

^aPeak to peak low field line width from dispersion signal.

3.4.3 SEEPR investigation of ${}^t\text{Bu}_4\text{P}_2$

Our attempts to generate a spectrum that could be conclusively attributed to $[\text{}^t\text{Bu}_4\text{P}_2]^{+\bullet}$ by chemical oxidation were unsuccessful. As an alternative route to $[\text{}^t\text{Bu}_4\text{P}_2]^{+\bullet}$, we conducted SEEPR experiments on solutions of ${}^t\text{Bu}_4\text{P}_2$ in CH_2Cl_2 containing $[\text{}^n\text{Bu}_4\text{N}][\text{PF}_6]$ as the supporting electrolyte. For SEEPR investigations, the conventional low-temperature flat cell with a gold micromesh working electrode (described in 2.3.1) was used. Oxidative electrolysis of a 5 mM solution resulted in the detection of a weak but distinguishable spectrum exhibiting three broad lines (Figure 3.21). The evidence proved that this is a very unstable radical, the radicals die faster than the time to scan between two signals. These results clearly show the power of SEEPR for highly unstable radicals. Measuring the line widths suggested that the middle line is unusually broad. Therefore, simulation with third order perturbation theory was required to get the right fit. In fact, the resulting line width of the middle peak is more than 7 Gauss and by running the simulation with smaller LW, then it is possible to see the (very small) splitting of the central line as observed for the other diphosphines. The higher order splitting effect, which has been discussed in Section 3.4.1, is smaller in this spectrum, which is consistent with the HFS to phosphorus being so much smaller in ${}^t\text{Bu}_4\text{P}_2$ than for Dipp_4P_2 . Thus, there is an unresolved second order effect, which can be detected with smaller LW. The most obvious evidence is that the height of this middle peaks is not correct for a first order triplet. The simulations have not been able to correct for slow-tumbling line shape effects; despite this the central line is 0.72 mT peak-to-trough, a clear indication along with the unexpectedly low intensity of the central branch that this spectrum displays unresolved higher order splitting. The simulation parameters are: $a(^{31}\text{P}) = 10.81\text{mT}$, $a(^{13}\text{C}) = 2.5\text{ mT}$ (from “satellite” signals seen in Figure. 3.21c,d attributed to

the ~1% abundant ^{13}C nuclei), a LW of 5.30 G and a line shape of 50% Gaussian, 50% Lorentzian, which is indicative of additional unresolved HFS.

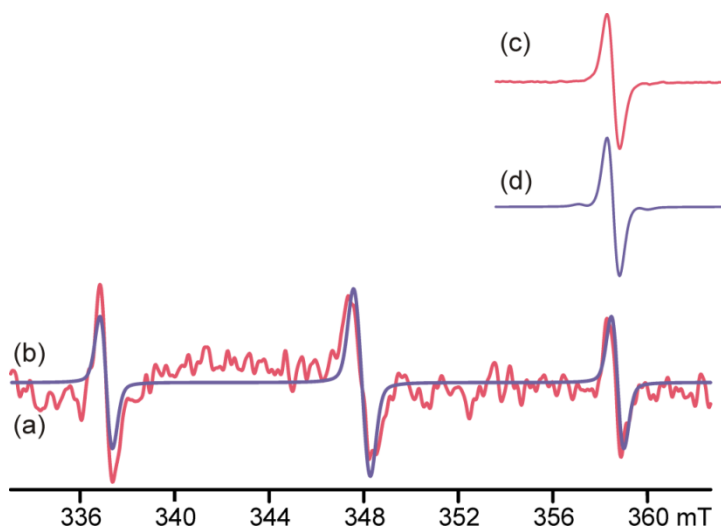


Figure 3.21. SEPR spectra collected at 0 °C in $\text{CH}_2\text{Cl}_2/0.4 \text{ M } ^n\text{Bu}_4\text{NPF}_6$ on $^t\text{Bu}_4\text{P}_2$ with electrolysis at a potential of 1.4 V. (a) Experimental rapid sweep over the full signal range; (b) simulation of this experimental spectrum (1:1 Lorentzian and Gaussian line shape components; $\text{LW} = 0.53 \text{ mT}$; $2 \times A(^{31}\text{P}) = 10.81 \text{ mT}$; $4 \times A(^{13}\text{C}) = 2.5 \text{ mT}$). (c) Experimental high field branch collected under slow passage conditions. (d) Simulation of (c) with the same parameters used in (b).

3.5 In electronic structure of R_4P_2 from DFT calculations

3.5.1 Introduction

A basic introduction to the DFT method is provided in Section 2.4. This quantum-mechanical method is suitable for use on molecules of the size and complexity that are the subject of this thesis. Furthermore, DFT methods have been extensively tested for calculating molecular properties, and here specifically their accuracy and reliability for calculating Hyper

fine splitting parameters of the kind measured in EPR spectroscopy. DFT have been used to gain understanding on the molecular and electronic structure of studied molecules and to help interpret the EPR spectra which have been measured. The approach that will be taken here is to first develop electronic structure and an understanding of bonding as a function of molecular charge state using a simplified model system. From there a discussion of the key “frontier” orbitals of Dipp_4P_2 and its oxidation products will be focused. Finally, review the calculated isotropic hyperfine splitting constants that helped to interpret the EPR spectra discussed in Section 3.4. Diphosphine, $\text{H}_2\text{P}-\text{PH}_2$, known since 1844, is the prototype of open-chain phosphorus hydrides and has been the subject of numerous experimental and theoretical studies. However, computational studies of its cation and dication, which are model systems for the one and two-electron oxidations of Dipp_4P_2 , have only been the subject of one computational study at Hartree-Fock level. Further insight into the stabilizing effects of the two-center three-electron bonding in the diphosphine radical cation is of particular importance to the oxidation of diphosphines and was therefore subjected to DFT studies.³⁶ The computational results reported here include the model system $[\text{H}_2\text{P}-\text{PH}_2]^{0/+ / 2+}$, $[\text{Dipp}_4\text{P}_2]^{0/+ / 2+}$ and $[\text{tBu}_4\text{P}_2]^{0/+ / 2+}$; the geometries including a study of various conformers were optimized by DFT methods with Becke's three-parameter hybrid functional combined with the Lee, Yang and Parr (LYP) correlation functional, which is denoted as B3LYP,³⁷ and the 6-31G(d) basis set for bulky Dipp groups and 6-311G++(3df,2p) for small H groups,³⁸ as implemented in Gaussian 03W.³⁹ For all systems, geometry optimizations were verified by frequency calculations

3.5.2 Geometry studies

The starting point for the analysis is the optimization of the R_4P_2 ($\text{R} = \text{Dipp}$, tBu and Ph) structure in three different states: neutral, cation and dication and in each case frequency

calculations were carried out to check for imaginary frequencies (negative values) to prove that the optimized geometry is at least a local minimum on the energy hypersurface. Data from frequency calculations did not show any negative numbers for Dipp_4P_2 which suggest that we can use them to compare the structures with the data obtained from crystallography and also with each other and other structures. The geometrical results are presented in Table 3.16 and show the very close agreement between the X-ray crystal (solid) and ground-state calculated (gas phase) structures determined for Dipp_4P_2 . The most significant deviations are in the P–P bond lengths, which are longer in the calculated, at 2.305 Å, compared to the experimental structure of the neutral molecule, at 2.224(1) Å, and $\sum\{\angle\text{-P-}\}$ which is 2.51° higher in the calculation. However, the calculations accurately reproduce the distortion of the P atom out of the plane of four carbon atoms of the aromatic rings. The same study with the same goal has been done for ${}^t\text{Bu}_4\text{P}_2$ (Table 3.17), with similar observations as for Dipp_4P_2 , except that the conformation adopted by the latter is a gauche conformation that is quite close to semi-eclipsed. ${}^t\text{Bu}_4\text{P}_2$ has been the subject of a very recent high-quality multi-thread structure determination combining single-crystal X-ray diffraction, gas-phase electron diffraction and *ab initio* computations.³

Table 3.16. P–P bond distances (Å) and selected angles (°) for Dipp_4P_2 from X-ray diffraction and computation

	X-Ray diffraction	B3LYP/6-31G(d)
P–P bond length(Å) ^a	2.224(1)	2.305
P2–P1–C25 (°)	104.10(6)	104.60
P2–P1–C13 (°)	110.33(6)	111.65
C25–P1–C13 (°)	105.21(8)	105.88
$\sum\{\angle\text{-P-}\}$ (°)	319.64	322.15

^a Atom numbering is that used for the diffraction study, see Figure 3.2

Table 3.17. P–P bond distances (Å) and selected angles (°) for ^tBu₄P₂ from X-ray diffraction and computation

	X-Ray diffraction	B3LYP/6-31G(d)
P–P bond length(Å) ^a	2.235(3)	2.276
P–P–C(°)	120.54(9)	120.69
P–P–C(°)	109.56(9)	100.07
C–P–C(°)	99.86(1)	109.50
Σ{∠ –P– }(°)	329.96	330.26

Next, H₄P₂ was examined as a simplified model for the electronic structure and bonding of Dipp₄P₂. In view of its small size, the study on H₄P₂ in three different electronic states: neutral, cation and dication, could be undertaken using a much larger basis set, 6-311G++(3df,2p). A thorough study of the conformational options was also undertaken and in addition, the geometries were also constrained to *D*_{2h} and *C*_{2h} symmetry to gain an understanding of the effect of these shapes on relative energies. The geometrical results of these calculations for all studied R₄P₂ have been summarized in Table 3.18.

Table 3.18. Computed geometry results for [H₄P₂]ⁿ⁺ and [Dipp₄P₂]ⁿ⁺ (*n* = 0, 1, 2)

	H ₄ P ₂	^t Bu ₄ P ₂	Dipp ₄ P ₂	H ₄ P ₂ ⁺	^t Bu ₄ P ₂ ⁺	Dipp ₄ P ₂ ⁺	H ₄ P ₂ ²⁺	^t Bu ₄ P ₂ ²⁺	Dipp ₄ P ₂ ²⁺
P–P bond length(Å)	2.253	2.276	2.305	2.149	2.222	2.205	2.012	2.080	2.063
Σ{∠ –P–}(°)	279.9	330.8	322.1	308.3	339.25	338.7	354.2	357.3	360

An interesting feature of these calculations is that, upon removal of two electrons, Dipp₄P₂²⁺ goes fully flat, probably because of steric repulsions among the Dipp peripheral groups. By contrast, H₄P₂²⁺ has the “*trans*-bent” geometry which is commonly observed for

heavier-element double bond compounds such as $R_2Si=SiR_2$ ⁴⁰. Figure 3.22 shows the flat geometry in $Dipp_4P_2^{2+}$ (a) vs. the slightly *trans*-bent structure of $H_4P_2^{2+}$ (b).

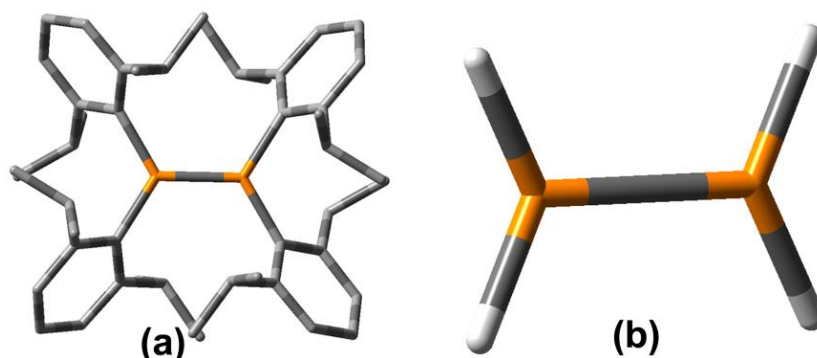


Figure 3.22. (a) $Dipp_4P_2^{2+}$ geometry calculated at B3LYP/6-31G (d) and (b) $H_4P_2^{2+}$ geometry calculated at B3LYP/6-311 G ++(3df,2p) level of theory

In separate calculations, the D_{2h} symmetry restraint was used for $H_4P_2^{+2}$ to force the molecule flat. By comparing the two results (Table 3.19), it is clear that the *trans*-bent geometry is just slightly lower in energy. While the flat molecule has some advantages for describing bonding because it is “isoelectronic” with $H_2Si=SiH_2$, i.e. it has a true or normal double bond, most 3rd-and-higher period double bonds show *trans*-bent geometries and this feature does not seem to compromise the multiple bond very much.⁴⁰ Also calculations that started flat but lifted the D_{2h} symmetry restraint were conducted. These calculations automatically went to the same *trans*-bent geometry which was originally calculated. Frequency calculations in D_{2h} symmetry have an imaginary frequency, and by animating the negative vibration, the molecule bending towards the shape that it has in the “true” *trans*-bent structure, indicating that this is the ground state for this dication. For related series, using the “isoelectronic” concept, $[H_2PPH_2]^+$ is like $[H_2SiSiH_2]^-$, while H_4P_2 is like $[H_2SiSiH_2]^{2-}$.

To determine whether *trans* (*anti*) is the ground state geometry for neutral H_4P_2 , two other calculations have been done; one in the *cis* (*syn*) conformation, the other a *gauche*

geometry (see Table 3.19). An optimization of the *cis* (*syn*) conformation kept the molecule in this geometry but a frequency calculation shows a negative coordinate which means it is not stable in this geometry but is a saddle point. A second calculation using a *gauche* conformation converged to a structure that remains *gauche* but lower in energy than the *anti* conformer (Table 3.19). However, of the three limiting geometries, the *syn* conformation lies much higher than the other two and the difference between the optimized *gauche* and the *anti* alternatives is actually very small (0.3 kJ mol⁻¹). In the subsequent discussion, the (slightly higher energy) *anti* conformation has been used for comparison as a simple bonding model for Dipp₄P₂ (Table 3.19).

Table 3.19. Calculations optimized at the B3LYP/6-311G++(3df,2p) level

H ₄ P ₂ in different conformations	Relative energies(kJ mol ⁻¹)
Trans (<i>anti</i>)	+0.36
Cis (<i>syn</i>)	+15.37
Gauche	0.00

The first step in comparing the effects of changing substituents is to compare the bond lengths of Dipp₄P₂ and H₄P₂ in neutral form. By looking at Table 3.18 the calculated P–P bond distances become longer from H₄P₂ to Dipp₄P₂ and the sums of angles around phosphorus, $\sum\{\angle\text{P}-\}$, become greater. There are two possible reasons for this pattern: (1) a steric effect of the bulky substituent, causing longer bond distances and flattening at P. (2) An electronic effect because of differences in electron donating ability of hydrogen and an aromatic hydrocarbon ring.

Secondly, for each type of substituent, the P–P bond distances become shorter and $\sum\{\angle\text{P}-\}$ around each phosphorus gets closer to 360° by removing a first and a second electron. The shortening that occurs upon oxidation (approximately 4% and 10% bond shortening for R

groups) is consistent with the onset of a double bond in the cation and dication. This is what is predicted from Lewis structures of these diphosphines (Figure 3.23). The increase in $\sum\{\angle\text{-P-}\}$ irrespective of the substituent bulkiness indicates that steric congestion is actually reduced upon oxidation as the non-bonded electrons are removed.

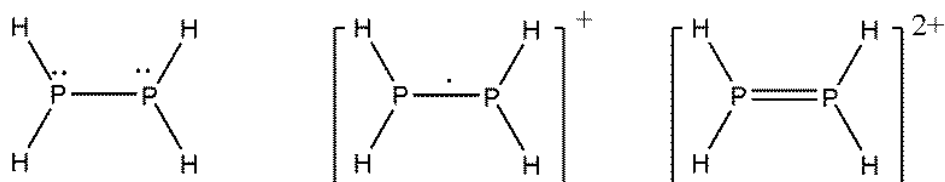


Figure 3.23. Lewis structure of diphosphine for neutral, cation and dication

3.5.3 Electronic structure include bonding

The *anti* conformer of $[\text{H}_4\text{P}_2]^{0/+2+}$ is selected for a detailed study of the electronic structure of diphosphines. After considering this highly-simplified model, the results are applied to the Dipp and ^tBu derivatives without having to work through the multitudes of orbitals of these huge molecules possess. It is interesting to see which molecular orbitals are involved in structure changes during the first and second oxidations and identifying orbitals with major contributions to changes in geometry accompanying oxidation. In the MO energy-level diagram (Figure 3.24), the orbitals are labelled for the correct C_{2h} point group (whereas both the Dipp and ^tBu derivatives only have C_2 point symmetry). Frequency calculations indicated that all three forms, neutral, cation and dication, are local minima.

Looking at the neutral state, there are seven electron pairs in the Lewis structure (Figure 3.22): five in single bonds and two in lone pairs. In the MO description, $1a_g$ and $2a_g$ correspond to the P–P σ bond as well as having P–H bond character, while $1b_u$, $1a_u$ and $1b_g$ are purely P–H σ -bond in character. Thus, in the neutral state $2b_u$ and $3a_g$ (the HOMO) describe the “non

bonding” electron pairs. These two orbitals are similar in being composed primarily from atomic p wave functions, but are not equivalent in energy as the Lewis structure would imply. From neutral to cation and then dication, all energy levels are lowered due to the increasing net atomic charges. Most significantly, as the $3a_g$ orbital is emptied, the molecular structure changes from pyramidal to close-to-planar as the $2b_u$ orbitals morphs into a good π -bonding MO. Thus the delocalized MO description can be understood to substantiate the simplistic descriptions of the Lewis diagrams. In addition, it is quite remarkable that the relative energies of the remaining MOs remain almost equal in relative energy. Thus, the contribution of the much-reorganized $2a_g$ orbital to P–P σ -bonding seems to be quite stable and independent of the geometry changes.

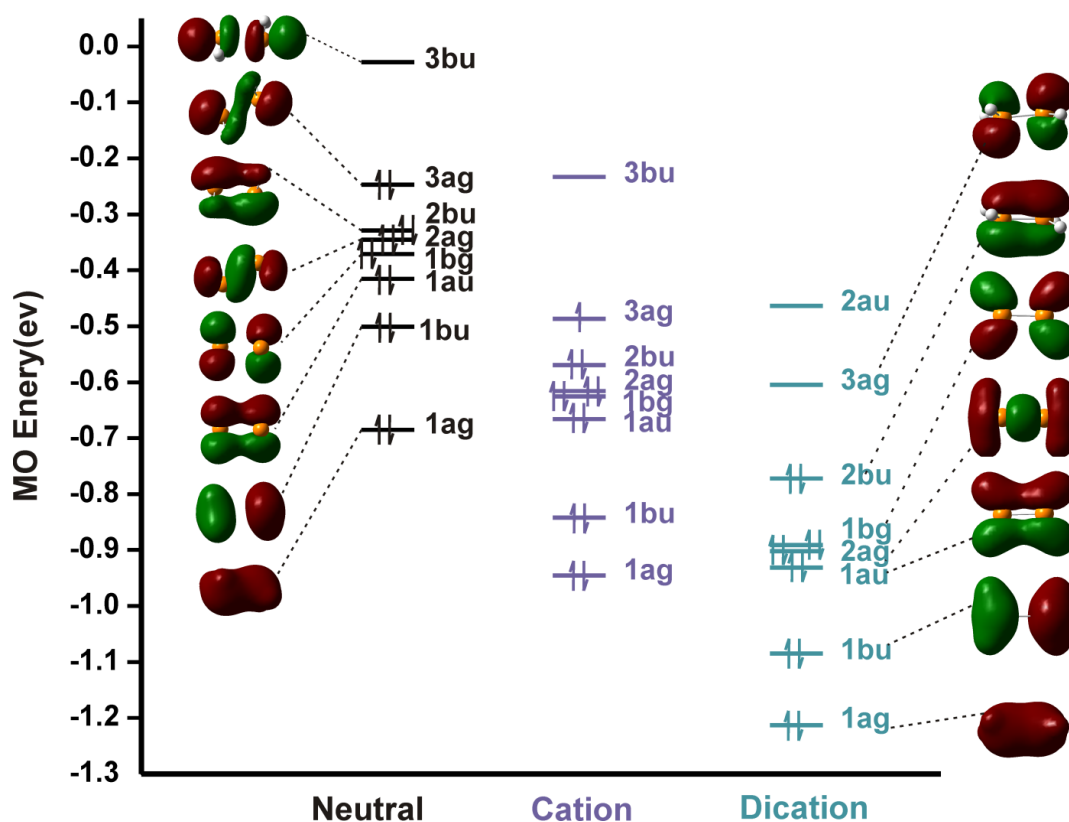


Figure 3.24. Molecular orbital energy diagram of H_4P_2 , $H_4P_2^+$ and $H_4P_2^{2+}$ calculated at the B3LYP/6-311 G ++(3df,2p) level constrained to C_{2h} symmetry

The frontier molecular orbitals in $\text{Dipp}_4\text{P}_2^{0/+2+}$ are remarkably similar to those of the highly-simplified model system, so it seems that very similar effects operate in the much larger molecule. The major difference in MO's of Dipp_4P_2 is of course the contribution of the electron-rich aromatic rings, which obviously affect the MO topologies to a certain extent. As depicted in Figure 3.25, the HOMO and HOMO-1 strongly resemble the “non-bonding electron pair” orbitals $2b_u$ and $3a_g$ of H_4P_2 .

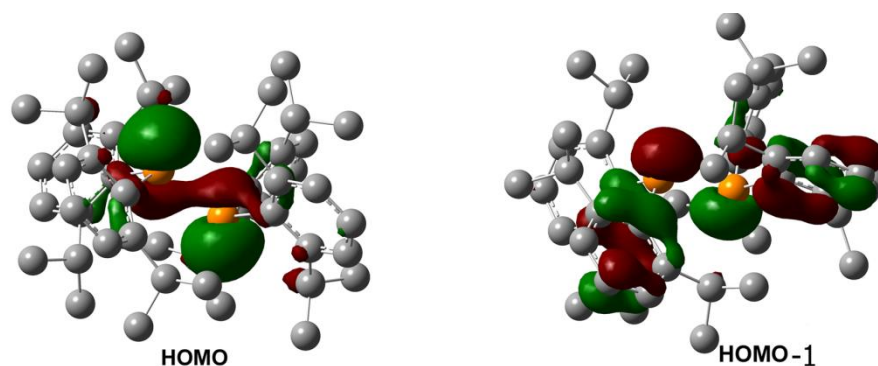


Figure 3.25. MO topologies for HOMO and HOMO-1 in neutral Dipp_4P_2

Similarly, in the dication, the LUMO has the P-P (π^*) character and strongly resembles the empty $3a_g$ function in the model dication. As shown in Figure 3.26, the HOMO for $\text{Dipp}_4\text{P}_2^{2+}$ is entirely localized on the aromatic rings. It is in fact expected that there are four such high-lying ring π^* orbitals. However, HOMO-4 actually corresponds to the π -bonding orbital of the formal double bond in $\text{Dipp}_4\text{P}_2^{2+}$ which is $2b_u$ in $\text{H}_4\text{P}_2^{2+}$. Note also that the asymmetrical and non-bonding HOMO orbital in the neutral molecule changes to the symmetrical and antibonding LUMO of the dication (Figure 3.26).

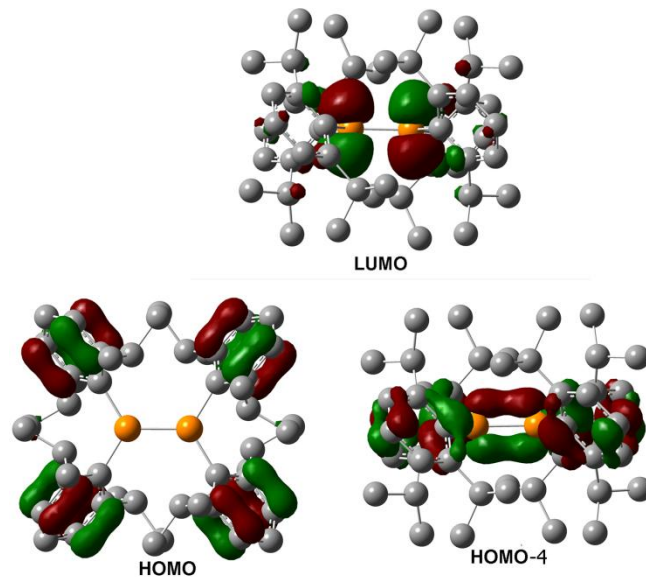


Figure 3.26. MO topology of HOMO, LUMO and HOMO-4 in $\text{Dipp}_4\text{P}_2^{2+}$

3.5.4 HFS constants from experiment and calculation

In Table 3.20 are collected some pertinent data related to the interpretation of the EPR spectroscopic data. Since the structures of the radical cations are not known, the gas-phase calculated geometries are used.³ The DFT calculations also provide calculated (isotropic) HFS values. Although the absolute agreement of calculated HFS values for 3rd period nuclei is rather poor, there is extensive evidence that the B3LYP functional gives reliable relative data.⁴³ Thus the ratio of the HFS for $\text{Dipp}_4\text{P}_2^{+\bullet}$ to ${}^t\text{Bu}_4\text{P}_2^{+\bullet}$ is about 2:1 for the calculated data, in reasonable agreement with the experimentally observed ratio of 1.7:1. This good agreement provides reasonable support for the tentative identification of the radical cation ${}^t\text{Bu}_4\text{P}_2^{+\bullet}$ from its fluid-solution EPR spectrum obtained in the SEEPR experiment. The picture of the SOMO shown in Figure 3.27 shows the geometry oriented looking down the Z-axis (the molecular C_2 rotation axis). It is easy to see from this distribution that the parallel HFS component is likely to be large and directed in the plus- and minus-z directions. There will be smaller perpendicular

contributions to the overall HFS, which is evidenced by the surrounding spin density on the Dipp rings.

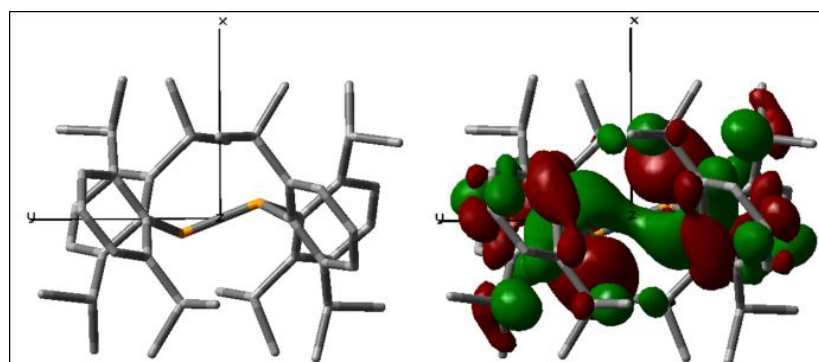


Figure 3.27. SOMO of Dipp₄P₂ radical cation down to the z-axis

Table 3.20. Summary of the DFT and EPR data for Dipp₄P₂ and ^tBu₄P₂

Species	Geometry	$\sum\{\angle\text{-P-}\}$, neutral /°	$\sum\{\angle\text{-P-}\}$, cation /°	a_{iso} , calc. DFT /mT	a_{iso} , fluid. soln. /Mt
Dipp ₄ P ₂	<i>Anti</i>	319.6	339.7	13.3	18.13
^t Bu ₄ P ₂	<i>Gauche</i>	329.1	341.4	6.4	10.81

3.6 Discussion

Further discussion will focus on the difference between Dipp₄P₂ and ^tBu₄P₂ and correlation between CV, DFT and EPR (SEEPR) studies on the Dipp₄P₂ compound. The ^tBu₄P₂ redox potential for the 0/+1 process, over the scan rate range 50 – 200 mV/s, is found to be 0.345±0.007 V more positive number than for Dipp₄P₂, from which it can be concluded that the former needs more energy for removing the first valence electron. Taking a closer look to the gas-phase DFT calculations indicates that the HOMO energy of neutral Dipp₄P₂ is –4.8 eV, while that for ^tBu₄P₂ is –5.1 eV. Thus, the difference of +0.3 volts-per-electron shows the same trend

and even agrees closely with the experimental solution-phase value from cyclic voltammetry. While this agreement may be just a good fortune, there may be more to it, insofar as the encapsulated nature of the HOMO is expected to show only small solvation/environmental effects.

In Dipp_4P_2 , there is a second oxidation peak but ${}^t\text{Bu}_4\text{P}_2$ shows just one oxidation process (ignoring the small secondary peak attributed to an oxide impurity). Cyclic voltammograms through this second process appear less “reversible” than is the case for the first process. It is certainly possible that this reflects an *EEC* mechanism due to a follow up reaction of the highly electrophilic dication with adventitious moisture or other impurities, as is commonly observed for phosphine cations.⁴⁴ However, an important diagnostic for what is occurring here is that the CV peak separations ΔE_{p2} (mV) are consistently higher than ΔE_{p1} (mV) and the difference increases with scan rate such that $\Delta E_{p2} - \Delta E_{p1}$ increases from 24 to 105 mV over scan rates of 100 to 800 mV/s.

A reasonable explanation for these changes is that the second oxidation involves more extensive geometry changes (the dication is predicted to be flat in the case of $\text{Dipp}_4\text{P}_2^{2+}$). Large geometry reorganization is related to higher activation energy for electron transfer, a common source of electrochemical irreversibility (i.e. slow rates of electron transfer from the analyte to the solid electrode surface).

Finally, it should be mentioned that in Tordo and co-workers’s⁴² reports on the closely related tetraaryldiphosphines (see Table 1.4), they explicitly claimed to have seen just one process in their CV data whereas in Dipp_4P_2 two obvious oxidation peaks have been observed. Thus, the latter is the first diphosphine for which two sequential one-electron oxidation processes have been reported, even though such behaviour is fully consistent with the electronic structure

of this class of molecules. Direct numerical comparison of the Tordo *et al.* redox data is complicated by using a very different solvent/reference system. However, a careful comparative study of some reliable example compounds, namely tris(trimesityl)phosphine, and tris(*ortho*-xylyl)phosphine, provides a conversion factor of -0.57 ± 0.03 to my conditions. By this criterion, the voltages for their compounds become approximately $+0.19 \pm 0.03$, $+0.09 \pm 0.03$ and -0.04 ± 0.03 V, respectively, for 2,6-dimethylphenyl, 2,4,6-trimethylphenyl and 2,4,6-triethylphenyl substituents.⁴² The uncertainty in the scaling method makes it futile to make direct comparison of substituent effects, but the general agreement is good.

Last but not least, the DFT calculations provide a very important aid in the interpretation of the EPR data obtained from the SEEPR investigation of the dilute solutions of ${}^t\text{Bu}_4\text{P}_2$ and Dipp_4P_2 radical cations. While both spectra are readily interpreted in terms of a single unpaired electron interacting with two equivalent ${}^{31}\text{P}$ nuclei, there is a surprising difference in the size of the isotropic hyperfine splitting constant, which is 18.1 mT for $\text{Dipp}_4\text{P}_2^{+\bullet}$ and only 10.3 mT for ${}^t\text{Bu}_4\text{P}_2^{+\bullet}$. While it is tempting to attribute this to differences in geometry, the calculated planarity for the two radical cations in terms of $\sum\{\angle\text{-P-}\}$ are in fact very close, although the ${}^t\text{Bu}$ case is flatter, consistent with the notion that a flatter pyramid involves less s orbital character in the SOMO, since s character is the only means for transmitting isotropic HFS via the Fermi contact mechanism. The resulting isotropic hyperfine coupling is related to the finite probability of the unpaired electron being at the nucleus.⁴¹ It is therefore very gratifying that the DFT-calculated HFS values, which take into account the full subtleties of the electronic structure of the wave function, fully corroborate the observed large difference in HFS values for these two radical cations. In fact, the calculated values of 13.1 and 6.4 mT, respectively, have relative differences that are quite similar (even though the absolute agreement is less than ideal to the expected ratios).

Usually, DFT methods provide excellent agreement for ^1H HFS constants in many small molecules, but for heavier nuclei the agreement is found to be only sufficiently good to allow the correct assignment of nuclei by their calculated HFS constants in comparison to experimentally determined values.⁴³

Data for $a(^{31}\text{P})$ for Dipp_4P_2 is in a reasonable agreement with data from Table 1.5 for the 2,6-dimethylphenyl, 2,4,6-trimethylphenyl and 2,4,6-triethylphenyl analogues. The uniformly smaller values from the Tordo group may reflect a difference in ground state geometry, which they claim is gauche, or may be the result of differences in spectral analysis. Indeed, the line shape/line width of the spectrum shown in Figure 1.2 (compare with Figure 3.17) is dramatically different. This may be due to such a geometrical difference, but could also be due to the considerably more viscous solvent system in Tordo's work.⁴²

References

1. Dodds, D. L.; Haddow, M. F.; Orpen, A. G.; Pringle, P. G.; Woodward, G. *Organometallics*. **2006**, *25*, 5937.
2. Hinchley, S. L.; Morrison, C. A.; Rankin, D. W. H.; Macdonald, C. L. B.; Wiacek, R. J.; Cowley, A. H.; Lappert, M. F.; Gundersen, G.; Clyburne, J. A. C.; Power, P. P. *Chem. Commun.* **2000**, 2045.
3. Hinchley, S. L.; Robertson, H. E.; Borisenko, K. B.; Turner, A. R.; Johnston, B. F.; Rankin, D. W. H.; Ahmadian, M.; Jones, J. N.; Cowley, A. H. *Dalton Trans.* **2004**, 2469.
4. Sasaki, S.; Ogawa, K.; Watanabe, M.; Yoshifuji, A. M. *Organometallics*. **2010**, *29*, 757.
5. Brady, F. J.; Cardin, C. J.; Cardin, D. J.; Wilcock, D. J. *Inorg. Chim. Acta*. **2000**, *298*, 1.
6. Wang, Y.; Sturm, T.; Steurer, M.; Arion, V. B.; Mereiter, K.; Spindler, F.; Weissensteiner, W. *Organometallics*. **2008**, *27*, 1119.
7. Stepanov, B. I.; Karpova, E. N.; Bokanova, Z. A. *Obshch. Khim.* **1969**, *39*, 1544.
8. Niebergall, H.; Langenfeld, B. *Chem. Ber.* **1962**, *95*, 64.
9. Brauer, D. J.; Bitterer, F.; Dorrenbach, F.; Hebler, G.; Stelzer, O.; Kruger, C.; Lutz, F. *Z.Naturforsch., B:Chem.Sci.* **1996**, *51b*, 1183.
10. Nifant'ev, E. E.; Trofimtsova, I. A.; Chekulaeva, L. A.; Chechegoeva, E. V.; Gavrilenko, V. V. *Zhurnal Obshchei Khimii.* **1992**, *62*, 1027.
11. Conrad, E.; Burford, N.; McDonald, R.; Ferguson, M. J. *J. Am. Chem. Soc.* **2009**, *131*, 17000.
12. Goldwhite, H.; Kaminski, J.; Millhauser, G.; Ortiz, J.; Vargas, M.; Vertal, L.; Lappert, M. F.; Smith, S. J. *J.Org. Chem.* **1986**, *310*, 21.
13. Van den Winkel, Y.; Bastiaans, M. M.; Bickelhaupt, F. J. *J. Organomet. Chem.* **1991**, *405*, 183.
14. Foss, V. L. *Zhurnal Obshchei Khimii.* **1979**, *49*, 1724.
15. Boéré, R. T.; Klassen, V.; Wolmershauser, G., *Can. J. Chem.* **2000**, *78*, 583.
16. Boéré, R. E.; Boéré, R. T.; Masuda, J.; Wolmershauser, G., *Can. J. Chem.* **2000**, *78*, 1613.
17. Boéré, R. T.; Bond, A. M.; Cronin, S.; Duffy, N. W.; Hazendonk, P.; Masuda, J. D.; Pollard, K.; Roemmele, T. L.; Tran, P.; Zhang, Y. *New J. Chem.* **2008**, *32*, 214.

18. Hinchley, S. L.; Morrison, C. A.; Rankin, D. W. H.; Macdonald, C. L. B.; Wiacek, R. J.; Cowley, A. H.; Lappert, M. F.; Gundersen, G.; Clyburne, J. A. C.; Power, P. P. *Chem. Commun.* **2000**, 2045.
19. Richter, R.; Kaiser, J.; Sieler, J.; Hartung, H.; Peter, C. *Acta Crystallogr., Sect. B.* **1977**, *33*, 1887.
20. Baxter, S. G.; Cowley, A. H.; Davis, R. E.; Riley, P. E. *J. Am. Chem. Soc.* **1981**, *103*, 1699.
21. Dashti-Mommertz, A.; Neumuller, B. *Z. Anorg. Allg. Chem.* **1999**, *625*, 954.
22. Mundt, O.; Riffel, H.; Becker, G.; Simon, A. *Z. Naturforsch. B: Chem. Sci.* **1988**, *43*, 952.
23. William, M. F.; Nicholas, H. R.; Lara, C.; Mohammed, P.; Ian, J. C. *J. Chem. Soc., Dalton Trans.* **2000**, 4453.
24. Donald, L. P.; Gary, M. L.; Kriz, G. S., Introduction to spectroscopy: a guide for students of organic chemistry,. Third ed.; Harcourt College Publishers: Bellingham, Washington, 2000; p 126.
25. Gritzner, G. K. *J. Pure Appl. Chem.* **1984**, *56*, 461.
26. Bard, A. J.; Faulkner, L. R., *Electrochemical Methods: Fundamentals and Applications*. 2nd ed.; Wiley: New York, 2001.
27. Stojanovic, R. S.; Bond, A. M. *Anal. Chem.* **1993**, *65*, 56.
28. Niemann, J.; Schoeller, W. W.; von der Gönna, V.; Niecke, E. *Chemische Berichte.* **1991**, *124*, 1563.
29. Bond, A. M., *Broadening Electrochemical Horizons*. Oxford University Press: New York, 2002.
30. Neudeck, A.; Kress, L. *J. Electroanal. Chem.* **1997**, *437*, 141.
31. Weil, J. A.; Bolton, J. R. *In Electron Paramagnetic Resonance*. Wiley-Interscience: Hoboken, NJ, 2007.
32. Weil, J. A.; Bolton, J. R., Appendix C: The Hydrogen Atom and Selected Radicals RHn. *In Electron Paramagnetic Resonance*, John Wiley & Sons, Inc.: 2006; pp 484.
33. Ayant, Y.; Kernevez, N.; Thevand, A.; Werbelow, L. G.; Culcasi, M.; Gronchi, G.; Tordo, P. *J. Magn. Reson.* **1986**, *70*, 446.
34. Marina, B; Giamello, E., *Electron Paramagnetic Resonance: A Practitioner's Toolkit*. John Wiley & Sons, Inc.: Hoboken, New Jersey, 2008.

35. Bennati, M.; Murphy, D. M., Electron Paramagnetic Resonance Spectra in the Solid State. In *Electron Paramagnetic Resonance*, John Wiley & Sons, Inc.: 2008; pp 195.
36. Mikhail, N. G.; Robert, D. B. *Chem. Phys. Lett.* **1997**, *265*, 514.
37. Becke, A. D. *J. Chem. Phys.* **1993**, *98*, 5648.
38. Ditchfield, R.; Hehre, W. J.; Pople, J. A. *J. Chem. Phys.* **1971**, *54*, 724.
39. Frisch, M. J. T.; Schlegel, H. B.; Scuseria, G. E.; Robb, M. A.; Cheeseman, J. R. Z.; Montgomery, J. J. A.; Stratmann, R. E.; Burant, J. C. D.; Millam, J. M.; Daniels, A. D.; Kudin, K. N.; Strain, M.; Farkas, O. T. J.; Barone, V.; Cossi, M.; Cammi, R.; Mennucci, B.; Pomelli, C. A. C.; Clifford, S.; Ochterski, J.; Petersson, G. A.; Ayala, P. Y.; Cui, Q. M. K.; Malick, D. K.; Rabuck, A. D.; Raghavachari, K.; Foresman, J. B.; Ortiz, J. V.; Baboul, A. G.; Stefanov, B. B.; Liu, G.; Liashenko, A.; Komaromi, I.; Gomperts, R.; Martin, R. L.; Fox, D. ; J.; Keith, T. A. L.; Peng, C. Y.; Nanayakkara, A.; Challacombe, M.; Gill, P. M. W. J.; Chen, W.; Wong, M. W.; Andres, J. L.; Gonzalez, C.; Head-Gordon, M. R.; Pople, J. A. *Gaussian 98*, Revision A.9 Gaussian, Inc: Pittsburgh, PA, 1998.
40. Protasiewicz, J. D.; Washington, M. P.; Gudimetla, V. B.; Payton, J. L.; Cather Simpson, M. *Inorg. Chim. Acta.* **2010**, *364*, 39.
41. Murphy, D. M., EPR (Electron Paramagnetic Resonance) Spectroscopy of Polycrystalline Oxide Systems. In *Metal Oxide Catalysis*, Wiley-VCH Verlag GmbH & Co. KGaA: 2009; pp 1.
42. Culcasi, M.; Gronchi, G.; Tordo, P. *J. Am. Chem. Soc.* **1985**, *107*, 7191.
43. Tuononen, H. M.; Chivers, T.; Armstrong, A.; Fedorchuk, C.; Boéré, R. T. *J. Organomet. Chem.* **2007**, *692*, 2705.
44. Merzougui, B.; Berchadsky, Y.; Tordo, P.; Gronch, G. *Electrochim. Acta.* **1997**, *42*, 2445.

Chapter 4

Electrochemical investigations of Dipp₃As and Tripp₂DippP radical cations

4.1 Introduction

As discussed in Chapter 1, series of triarylphosphines with different bulky substituents and related triarylpnictogens have been fully studied over the last few decades.^{1,2} The impact of steric shielding on the phosphorus center can be observed in the anodic behavior of these compounds, with trends in the redox potentials based on the ligand size and type. The stability of the radical cations is also reflected in their EPR behavior, based on how protected the phosphorus cation is by its substituents. In this chapter electrochemical and EPR studies of two additional compounds in this class which were synthesized in our group; Tripp₂DippP (Twyla Gietz)³ and Dipp₃As (Brock Price)⁴ will be discussed. These compounds have not previously been published in the literature.

4.2 Cyclic voltammetry results

4.2.1 Results of cyclic voltammetry of Tripp₂DippP

Tripp₂DippP was studied by CV on a GC electrode in CH₂Cl₂ with 0.4 M [ⁿBu₄N][PF₆] over scan rates of 0.05–0.8V s⁻¹ and temperatures of 21 ± 2 °C. Two oxidation processes appear upon sweeping the potential in the anodic direction from the rest potential (-0.4 V vs. Fc⁺⁰), designated as E_p^{al} and E_p^{cl} . Voltammetric results are reported in Table 4.1 and representative CVs obtained at a scan rate of 0.2 V s⁻¹ are shown in Figure 4.1. The first oxidation process displayed close to electrochemically reversible behaviour, with anodic (E_p^{al}) to cathodic (E_p^{cl}) peak-to-peak separations ΔE_{p1} in the range of 102–188 mV. A second, irreversible oxidation

process labelled E_p^{a2} in Figure 4.1 is observed at a considerably more positive potential similar to what has been observed in the cases of Dipp₃P and Tripp₃P and even upon scanning faster (up to 20 V s⁻¹) no changes in the relative size of the return wave for this process was observed. However, cycling of the potential through both redox couples serves to decrease the return wave (E_p^{c1}) for the first oxidation process.

Table 4.1. Summary of cyclic voltammetry data obtained for both oxidation process of Tripp₂DippP at a GC electrode and T = 22 °C.

$v(\text{mVS}^{-1})$	$E_p^{a1}(\text{V})$	$E_p^{c1}(\text{V})$	$E_{m1} \cong E_{fl}^{\circ}(\text{V})$	$\Delta E_{p1}(\text{mV})$	$E_p^{a2}(\text{V})$	I_p^{ox}/I_p^{red} (μA)
50	0.0550	-0.0410	0.0070	102	1.1770	0.90
100	0.0615	-0.0405	0.0105	115	1.1965	0.95
200	0.0715	-0.0495	0.0110	134	0.6785	0.95
400	0.0895	-0.0565	0.0165	157	1.2435	0.96
800	0.1145	-0.0565	0.029	188	1.2815	0.97

Obtained in CH₂Cl₂ solution containing 0.4 M [ⁿBu₄N][PF₆] measured against Cc⁺⁰ and expressed vs. $E_{Fc+/0}^{\circ}$.

The I_p^{ox}/I_p^{red} ratio approaches unity as the scan rate is increased for the E_p^{a1}/E_p^{c1} process. As is expected, the Tripp₂DippP⁺⁰ process should fall somewhere between Tripp₃P⁺⁰ and Dipp₃P⁺⁰; indeed it is found to be 0.08V more cathodic than the Dipp₃P⁺⁰ and 0.05 V less cathodic than the Tripp₃P⁺⁰. This difference is likely due to the inductive influence of the ⁱPr group in the *para* position in Tripp which is missing in Dipp, or approximately 0.05 V per ⁱPr group. Since Dipp and Tripp are expected to be isosteric, they differ only by a remote “tail” substituent that can exert no steric pressure or steric shielding. Tordo and co-workers demonstrated similar inductive influences when comparing the 2,6-dimethyl (xyl) and 2,4,6-trimethylphenyl (mes) substituents.⁵

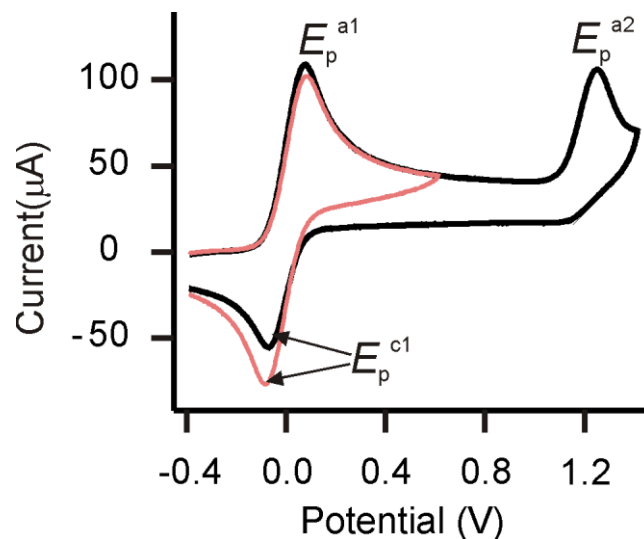


Figure 4.1. Cyclic voltammetry of Tripp₂DippP (5 mM) in CH₂Cl₂ solution containing 0.4 M [ⁿBu₄N][PF₆] under an atmosphere of dry Ar at $v = 0.2 \text{ Vs}^{-1}$ on a GC electrode at 20 °C: (a) through the first oxidation process (pink line); (b) through the first and second oxidation processes (black line)

4.2.2 Determination of the diffusion coefficients for Tripp₂DippP and Dipp₃As

RDE measurements on CH₂Cl₂ solutions of 5.009 mM Tripp₂DippP and 5.727 mM Dipp₃As were undertaken in order to determine the diffusion coefficient D . For RDE measurements, determination of the diffusion coefficient made use of the Levich equation (Eqn. 2.2), for which the kinematic viscosity (ν_k) was assigned the value of $0.003318 \text{ cm}^2\text{s}^{-1}$ in CH₂Cl₂ at 20 °C in place of a measured value for the solvent/electrolyte solution. Rotation rates between 1000 – 2250 rpm were applied over a potential range of –0.5 to 1 V for solutions of Tripp₂DippP and over the range of 0 to 1 V for solutions of Dipp₃As in CH₂Cl₂. Plots of the Levich current or limiting current (I_L^{-1}) vs the square root of the rotational velocity ($\omega^{-1/2}$) yielded straight lines in

each case with a slope = $(0.62nFACv^{-1/6}D^{2/3})^{-1}$. Solving for D , Eq.2.2 yielded values of 3.946×10^{-6} and $3.275 \times 10^{-6} \text{ cm}^2\text{s}^{-1}$ for Tripp₂DippP and Dipp₃As, respectively.

4.2.3 Results of cyclic voltammetry of Dipp₃As

CV studies were performed on CH₂Cl₂ solutions of Dipp₃As containing 0.4 M [ⁿBu₄N][PF₆] over scan rates of 0.05 – 0.8 V s⁻¹ on a GC working electrode. A quasi-reversible wave was detected at 0.41 V versus $E_{\text{Fc}+/0}^{\circ}$. However, the reversibility of this wave was compromised when scanning was continued beyond the first process, as one more irreversible oxidation process occurred at 1.44 V versus $E_{\text{Fc}+/0}^{\circ}$ (Figure 4.2). By comparing the two CVs of Dipp₃As and Tripp₂DippP it becomes obvious that, in comparison with Tripp₂DippP⁺², Dipp₃As⁺² is less stable. Considering the negative effect of the second process (black) on the first process (pink) shows more reduction in peak current in the case of Dipp₃As rather than Tripp₂DippP implies greater instability of the dication of Dipp₃As. All potentials are listed in following table. No attempts have been made to identify the nature of the second oxidation process and this will not be discussed in any further detail.

Table 4.2. Summary of cyclic voltammetry data obtained for both oxidation process of Dipp₃As at GC electrode and T = 22 °C.

$v(\text{mVS}^{-1})$	$E_p^{a1}(\text{V})$	$E_p^{c1}(\text{V})$	$E_{m1} \cong E_{f1}^{\circ}(\text{V})$	$\Delta E_{p1}(\text{mV})$	$E_p^{a2}(\text{V})$	$I_p^{\text{ox}}/I_p^{\text{red}}(\mu\text{A})$
50	0.4695	0.3505	0.4100	119	1.4015	0.96
100	0.4695	0.3505	0.4100	119	1.4015	1.10
200	0.5020	0.3540	0.4280	148	1.4470	1.07
400	0.5335	0.3295	0.4315	204	1.5135	1.00
800	0.5645	0.3115	0.438	253	1.5645	0.98

Obtained in CH₂Cl₂ solution containing 0.4 M [ⁿBu₄N][PF₆] measured against Cc⁺⁰ and expressed vs $E_{\text{Fc}+/0}^{\circ}$.

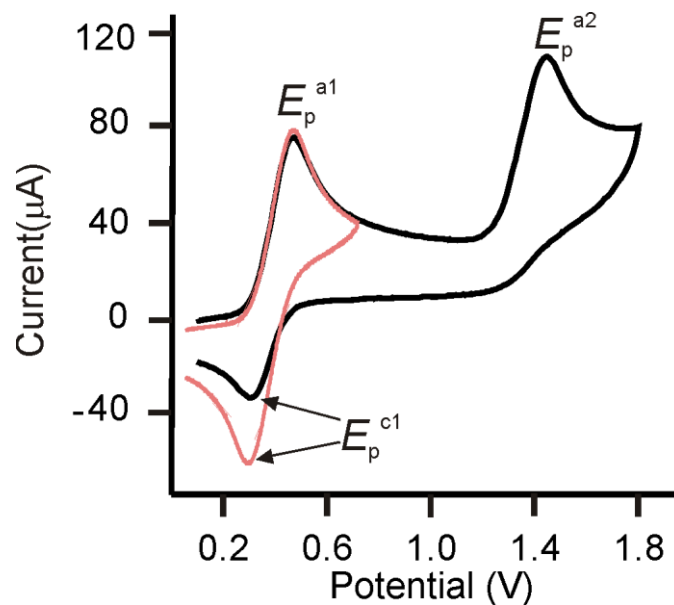


Figure 4.2. Cyclic voltammetry of Dipp_3As (5 mM) in CH_2Cl_2 solution containing 0.4 M $[\text{tBu}_4\text{N}][\text{PF}_6]$ under an atmosphere of dry Ar at $v = 0.2 \text{ Vs}^{-1}$ on a GC electrode at 20°C .

To compare the structure and properties of bulky triarylphosphines and arsines, a small selection of the many previously reported potential values from our lab and the Sasaki group is presented in Table 4.3. Serious problems are associated with the use of different reference potential scales by the two groups. For this reason, all the phosphorus compounds have been remeasured in our group by Dr. Tracey Roemmele. The data for the arsines from Sasaki *et al.* is rescaled by a similar correction factor. By taking a closer look at Table 4.3, it becomes obvious there are two major approaches that should be taken for comparisons. (1) The four arsine compounds with each other. (2) The arsines are compared with the phosphines.

First, the oxidation potentials of the triarylarisines become lower (less energy to remove an electron) as the lone pair (HOMO) is raised in energy. Two factors cause such a raising of the HOMO energy. (1) As the arsine becomes more crowded, there is enhanced planarity induced by steric congestion. This raises the HOMO by rendering it less bonding and hence more like an unhybridized p orbital. (2) As the electron donating ability of the substituents increase, there is

increased electron density on arsenic. Increased charge density (when the nuclei involved remain the same) also results in higher energy in the HOMO (electrons are less constrained by the positive charges in the nuclei). By considering the data in Table 4.3, it is clear that on moving from Ph (two *ortho* H atoms) to Mes (two *ortho* methyl groups) to Dipp/Tripp (two *ortho* isopropyl groups) the value of E_m decreases significantly, leading to a “tuning” of the first redox potential of some 0.7 V for this short series of substituents. Since it is the alkyl groups that are used to increase steric pressure and hence induce planarization, it is not directly possible to separate these two effects. However, since Tripp₃As and Dipp₃As are expected to be isosteric, the difference in values between these two substituents (0.14 V) fits very closely with obtained results for Tripp₂DippP, i.e. an inductive effect of approximately 0.05 V per isopropyl group (see Section 4.2.1).²

Secondly, all the arsenic compounds are harder to oxidize which means they have lower energy HOMOs than the phosphorus counterparts. A consideration of the last column in Table 4.3 shows that the difference between As and P is quite constant for Mes, Dipp and Tripp, but much smaller for Ph. This is almost certainly due to the irreversible processes encountered for Ph₃E; the measured potential for an irreversible process is always subject to distortions due to the thermodynamic influence of the follow-on reactions that engage the produced radical cations. On the other hand, the three bulkier substituents all have at least quasi reversible responses in CV; it is gratifying that these three show such constancy in terms of the central element effect. The lower-lying HOMO in R₃As is readily attributed to the well known fact that arsenic, despite being in a lower period, has a higher effective electronegativity than phosphorus (e.g. 2.2 vs. 2.06 for As and P on the Allred-Rochow scale).⁶ This counter-intuitive result is usually attributed to

the Scandide contraction, that is, the presence of the first filled d series, $3d^{10}$, in the electron configuration of arsenic.

Table 4.3. Summary of redox potential of triarylar sine and phosphine obtained in CH_2Cl_2 solution expressed vs $E^\bullet_{\text{Fc}^{+}/0}$.

Compound	$E_{\text{ml}} \cong E^\circ_{\text{fl}}(\text{V})$	Compound	$E_{\text{ml}} \cong E^\circ_{\text{fl}}(\text{V})$	ΔE_{ml} 's
Ph_3As^a	0.96	Ph_3P	0.88	0.08
Mes_3As^a	0.51	Mes_3P	0.19	0.32
Dipp_3As^b	0.42	Dipp_3P^c	0.09	0.33
$\text{Tripp}_3\text{As}^a$	0.28	Tripp_3P	-0.06	0.34

^aV vs Ag/Ag^+ in dichloromethane with 0.10 M $n\text{-Bu}_4\text{NClO}_4$, scan rate: 30 mVs^{-1} converted to Fc scale by subtracting 0.22 V ^{2b}0.4 M $[\text{nBu}_4\text{N}][\text{PF}_6]$ and 0.5 mM in analyte^c obtained at a Pt electrode at $v = 0.2 \text{ V s}^{-1}$, measured against $\text{Cc}^{0/+}$ and expressed versus $\text{Fc}^{0/+}$ by subtracting 1.35 V and 0.1 M $[\text{nBu}_4\text{N}][\text{PF}_6]$ and 1 mM in analyte.

4.2.4 EPR investigation of Dipp_3As by chemical oxidation

The reversible potential of the Dipp_3As redox couple is at +0.42 V vs. $\text{Fc}^{0/+}$, and no further oxidation occurs until +1.44 V vs. $\text{Fc}^{0/+}$. The list of potential chemical oxidizing agents provided by Connelly and Geiger advises that $\text{Ag}(\text{I})$ ion in CH_2Cl_2 solution should be a suitable oxidant at the $\text{Ag}^{0/+}$ redox couple of +0.65 V vs. $\text{Fc}^{0/+}$.⁷ This is an attractive reagent because the by-product is expected to precipitate as solid silver. Therefore AgPF_6 used as chemical oxidant to generate solutions of $[\text{Dipp}_3\text{As}]^{+0} \text{X}^-$ ($\text{X}^- = \text{PF}_6^-$) salts in CH_2Cl_2 .

Oxidation of Dipp_3As using AgPF_6 in CH_2Cl_2 resulted in the generation of $[\text{Dipp}_3\text{As}]^{+0}$ (Figure 4.3). What is expected is coupling of the unpaired electron to a single arsenic nucleus (^{75}As , $I = 3/2$, 100% abundant), which results in a four-line spectrum with equal spacing and intensity ratio of 1:1:1:1 as is simulated by the first order perturbation theory without considering the tumbling effect (Figure 4.3c). However, what is observed are four lines with different

intensities and different spacing. Explaining this pattern needs more background, of which a brief summary will be provided here.

In some cases, EPR studies may be performed which lie between the extremes of liquid with full averaging of dipolar HFS effects and a rigid powder pattern where no re-orientation motion exists. This intermediate region is characterized by “slow tumbling”.⁸ In such circumstances, the resulting spectral profile may produce a composite containing both isotropic and anisotropic components. Frequently one may observe distortions of the isotropic signal (i.e. inhomogeneous broadening of the lines) due to such residual dipolar effects.

It is therefore important to consider such effects in some detail. Rapid tumbling, faster than the EPR timescale, of an anisotropic paramagnetic system will cause an averaging of the g and a tensors. In the hypothetical case where the tumbling is infinitely rapid compared to the EPR timescale, a fully averaged, or isotropic, g and a value will be obtained. This rarely occurs, even under ideal conditions, and in practice evidence of g and a anisotropy can still be manifested in many solution spectra. This partial averaging of the signals can be easily accounted for by reference to the dependence of the line widths on the value of m_l . The peak-to-peak line widths ΔB_{p-p} of the first derivative signal can be expressed by the following equation:¹⁰

$$\Delta B_{p-p} = A + Bm_l + Cm_l^2 \quad \text{Eq. 4.1}$$

Where A , B and C are constants and depend linearly on the correlation time and on the anisotropic a and g tensors. Because A and C depend on the square of the anisotropies of g and a , respectively, the first and third terms in Eq. 4.1 are always positive. In contrast, the term $B m_l$ can be positive or negative, and it critically determines which line is broadened more in EPR spectra.⁹

Clearly, the line width and variation in the intensity across the spectrum depends on the value of m_I . Based on this knowledge, make a clear explanation of the $\text{Dipp}_3\text{As}^{++}$ EPR spectrum is possible. Four lines are observed (i) with different line spacing due to the second order effect (as was discussed in the previous chapter for $\text{Dipp}_4\text{P}_2^{++}$), and (ii) due to the slow tumbling effect which is discussed above, the line widths and intensities will be different. To get the best fit to the experimental spectrum, a simulation using third-order perturbation theory and also with consideration of the “slow tumbling effect” has been carried ($a_{(\text{As})} = 26.1$ mT and $g = 2.045$). The spacing from left to right is 24.126, 26.136 and 28.272 mT (Figure 4.3b). Line width parameters for slow tumbling effect have been calculated by simulation:

$$12.2 - 2.00m_I + 2.64m_I^2$$

Very similar powder patterns of Dipp_3As to Dipp_4P_2 in frozen solution have been observed. In the frozen glass, a characteristic axially symmetric powder pattern is obtained with parallel and perpendicular a tensor components of 47.9 and 19 mT, while a very small asymmetry in the g tensor is detected. The parallel and perpendicular g tensors are almost the same so the EPR spectrum is almost g -isotropic, with $g_{\perp} = 2.000$ and $g_{\parallel} = 2.025$ mT.

Table 4.4. Experimental EPR data for the $\text{Dipp}_3\text{As}^{+0}$ in solution

Line width(mT)	HFS(mT)	Temp(°C)
1.50	26.23	20
1.50	26.34	0

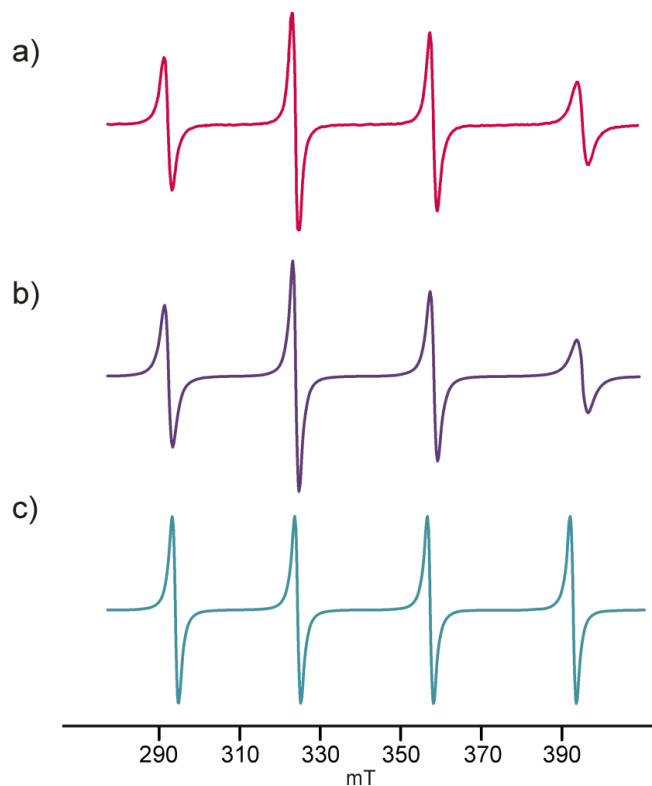


Figure 4.3. (a) Experimental fluid solution EPR spectrum of Dipp₃As obtained after chemical oxidation. (b) Best simulated spectrum (third-order perturbation theory and line-widths corrected for tumbling). (c) Simulation as in (b) without tumbling correction.

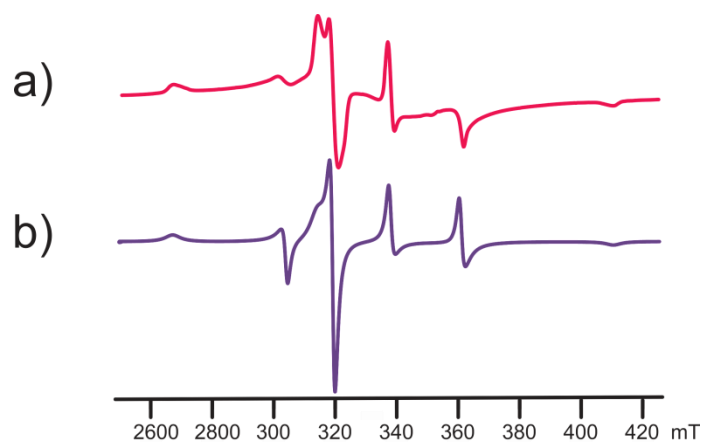


Figure 4.4. (a) Experimental frozen solution EPR spectrum of Dipp₃As obtained by chemical oxidation and (b) simulation obtained using second order perturbation theory

4.2.5 SEEPR investigations of Tripp₂DippP

The chemically quasi-reversible nature of the Tripp₂DippP⁺⁰ redox couple as evidenced by CV studies suggested that the use of SEEPR methodology for the detection of phosphorus radical cations would be very suitable. Temperatures were varied between -70 and 0 °C. For SEEPR investigations utilizing the low-temperature SEEPR cell and a modified version of the gold-micromesh working electrode first described by Neudeck and Kress (see Section 2.3.1) was used. Oxidative electrolysis at +0.5 V of a 0.5 mM solution of Tripp₂DippP in CH₂Cl₂/0.4 M [ⁿBu₄N][PF₆] resulted in the detection of a widely separated doublet due to coupling of the unpaired electron to ³¹P, with a HFS of 23.60 mT (Figure 4.5). Small peaks between the two major peaks are due to some small unidentified impurities in the sample. The peak-to-peak line width of the spectral lines was found to be between 0.68 and 2.22 mT, increasing as the temperature is lowered. Using Bruker Simfonia software, a simulation was obtained that exhibits line positions and line shapes that agree well with values deduced from the experimental spectra. All the experimental data is summarized in Table 4.5.

The phosphorus HFS constants increased slightly with increasing temperature (from 23.51 mT at -70 °C to 23.60 mT at 0 °C) and the linewidths increased significantly with decreasing temperature (from 0.68 mT to 2.22 mT) which is same as has been observed for Dipp₄P₂ and is due to the fact that the slow tumbling effect becomes more obvious at low temperatures. As a result, there is no distinct change in the overall shape of the spectra with temperature and only minor deviations in the line width, and the g value. The only major point to consider is the peak heights which should be 1 to 1 but due to the slow tumbling effect which is discussed in Section 4.2.4 is not. Linewidth parameters of slow tumbling effect have been calculated by simulation is:

$$7.0-0.8m_1$$

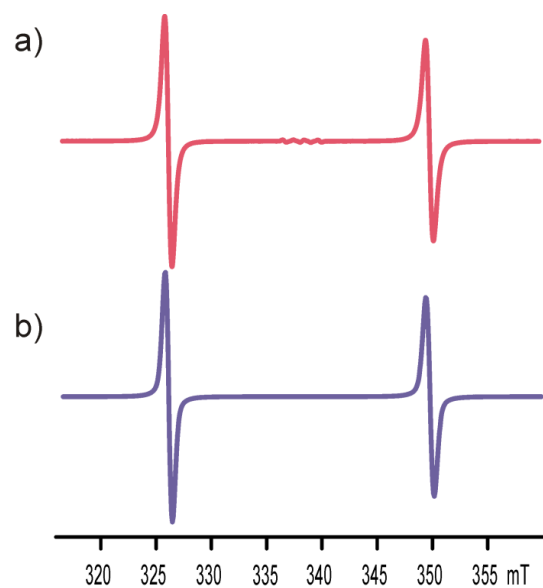


Figure 4.5. (a) Experimental fluid solution EPR spectrum of Tripp₂DippP obtained by SEEPR and (b) simulation with third order perturbation theory and corrected for slow tumbling

Table 4.5. Experimental EPR data for the Tripp₂DippP^{+/-0}

g value	Line width(mT)	HFS(mT)	Temp(°C)
2.00573	0.68	23.60	0
2.00597	0.78	23.60	-10
2.00606	0.86	23.60	-20
2.00607	0.95	23.51	-30
2.00608	1.11	23.51	-40
2.00608	1.15	23.60	-50
2.00608	1.76	23.51	-60
2.00608	2.22	23.51	-70

4.2.6 EPR investigation of Tripp₂DippP by chemical oxidation

In order to investigate the powder pattern of Tripp₂DippP⁺⁰, chemical oxidation experiment of this compound has been carried by using AgPF₆ in CH₂Cl₂ solution at 0 °C and -100 °C. Like Dipp₄P₂, in this case EPR spectra of dilute solutions of radicals are identical to those prepared by electrochemical methods. In the frozen glass, a characteristic axially symmetric powder pattern was obtained with parallel and perpendicular HFS tensor components of 42 and 13 mT, a very small asymmetry in the *g* tensor has been detected. The parallel and perpendicular *g* tensors are almost the same, so the EPR spectrum is close to being a *g*-isotropic system ($g_{\perp} = 2.009$ mT and $g_{\parallel} = 2.0055$ mT).

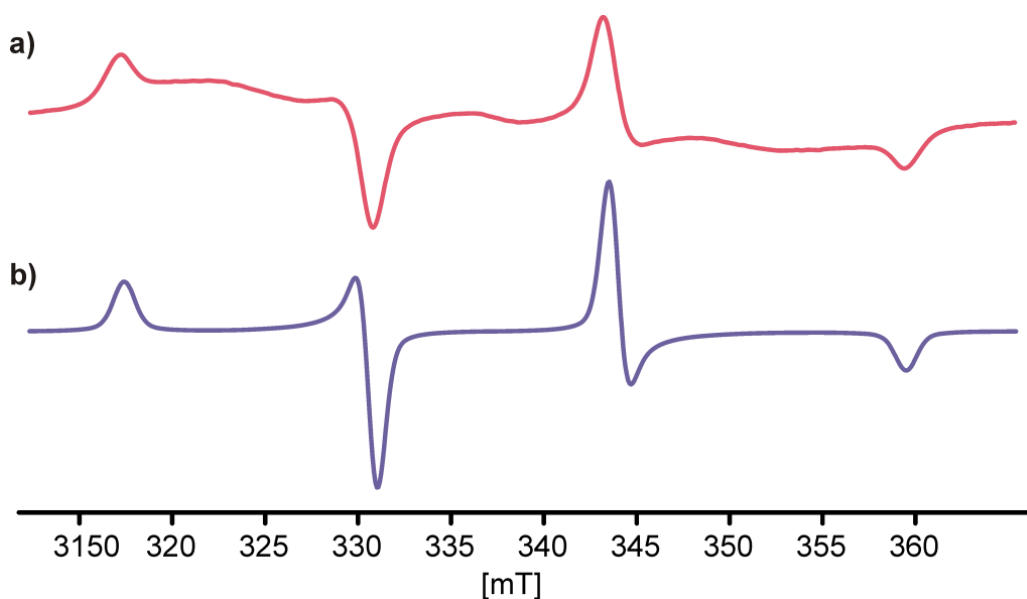


Figure 4.6. (a) Experimental frozen solution EPR spectrum of Tripp₂DippP obtained by chemical oxidation and (b) simulation using second-order perturbation theory

4.3 Application of anisotropic hyperfine coupling constant

Here two major applications of powder EPR spectra parameters will be discussed with full explanation in case of studied compounds. First, obtaining *s* component of the unpaired spin

density which is measured in solution and finding the direct relationship between the size of hyperfine and unpaired spin density which is experienced by the nuclei that the electron is coupled to. Unpaired electron density in the phosphorus and p orbitals is calculated from ratio of isotropic and anisotropic hyperfine coupling constants between the radical cation and phosphorus atom from the following equations:

$$\text{Isotropic hfc constant} = a = 1/3(a_{\parallel} + 2a_{\perp})$$

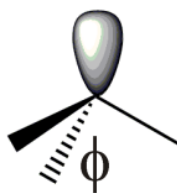
$$\text{Anisotropic hfc constant} = b = 1/3(a_{\parallel} - a_{\perp})$$

$$\rho(s) = (a/a_0) \times 100 \quad \text{Eq. 4.2}$$

$$\rho(p) = (b/b_0) \times 100 \quad \text{Eq. 4.3}$$

Where $\rho(s)$ is the percentage of s character of the unpaired electron at the nucleus and $\rho(p)$ is the percentage of p character of the unpaired electron at the nucleus, a_0 and b_0 are base values for full spin density at the nucleus which are 474.79 mT and 13.088 mT respectively for ^{31}P and 523.11 mT and 11.905 mT for ^{75}As . It should be noted that these calculated values are only approximate and will probably be increasingly erroneous at higher atomic numbers.¹⁰

A second application of anisotropic parameters of powder spectra is that hybridization of the 3s and 3p orbitals can be deduced from the ratio of unpaired electron density between the phosphorus 3s and 3p orbitals and structure of the C_{3v} radical is estimated from Coulson's equation (Eqs.4.4 and 4.5).^{1, 11}



$$\lambda^2 = \frac{\rho(p)}{\rho(s)} \quad \text{Eq.4.4}$$

$$\phi = \cos^{-1} \left[\frac{1.5}{(2\lambda^2 + 3)} - \frac{1}{2} \right] \quad \text{Eq. 4.5}$$

Using these concepts, the following results (Table 4.6) are obtained for [Tripp₂Dipp]⁺⁺, [Dipp₃As]⁺⁺ and also [Dipp₄P₂]⁺⁺. Unfortunately, to date no frozen-solution data has been obtained for [^tBu₄P₂]⁺⁺ (the lifetime of the radical is too short). There is a very good agreement between sum of the angles around phosphorus derived by calculation from the experimental EPR data in frozen solution with the results from gas-phase DFT calculations on these radical cations. Comparing this data with those tabulated in Chapter 1 (Table 1.8) shows that the introduction of more bulky aryl groups leads to enhanced *p*-character of the SOMO, and the radical cations are less pyramidalized with these substituents, similar to the structural effects they also have on the neutral phosphines (Table 1.9).

Table 4.6. EPR and structural parameters of radical cations of studied compounds

	a_{\parallel} (mT)	a_{\perp} (mT)	<i>A</i>	<i>B</i>	$\rho(s)$	$\rho(p)$	$\phi_{AVE}(^{\circ})$	$\sum\{\angle-E-\}(^{\circ})$	$\sum\{\angle-E-\}(^{\circ})$ cal
[Tripp ₂ Dipp] ⁺⁺	42	13	22.6	9.6	4.7	73.3	117.1	351.3	359.6
[Dipp ₃ As] ⁺⁺	47.9	19	28.6	9.6	5.5	80.6	116.98	350.9	357.6
[Dipp ₄ P ₂] ⁺⁺	29.34	14.16	19.22	5.06	4	38.6	115.6	346.8	347

4.4 DFT calculation results in Dipp₃As

A DFT calculation for Dipp₃As cation shows that it goes quite flat on oxidation: Sum of the angles C–As–C = 357.6° at this level of theory. This is also very similar to the Dipp₃P cation at the same level of theory ($\sum\{\angle C-P-C\} = 359.7^{\circ}$).² The P and As systems have been done at the same level of theory and show that they are very similar in being almost flat. The calculated spin densities (fraction of the single unpaired electron) on P in Dipp₃P⁺ is 0.858, on As in Dipp₃As⁺ is 0.787 (the rest of the spin density is distributed over the SOMO over the rest of the Dipp rings). The ratio of the solution phase isotropic hfc is 23.9 Dipp₃P to 26.1 Dipp₃As, or

0.916. The ratio of the “standard” A_{iso} for ^{31}P and ^{75}As is 474.79 to 523.11 (for full spin density of 1 electron in the corresponding “s” orbitals; the values from the Table in Weil & Bolton),¹⁰ which works out to 0.908. That is remarkably close, and suggest that in the amount of s-orbital spin density on Dipp_3P^+ and Dipp_3As^+ is extremely similar.

Table 4.7. Summary of DFT calculation for Dipp_3As^+

	$\sum\{\angle\text{C-E-C}\}$	Exp a_{iso}	Calc a_{iso}	Spin density
Dipp_3As^+	357.6(°)	26.1	18.7	0.787
Dipp_3P^+	359.7(°)	23.9	13.4	0.858

References

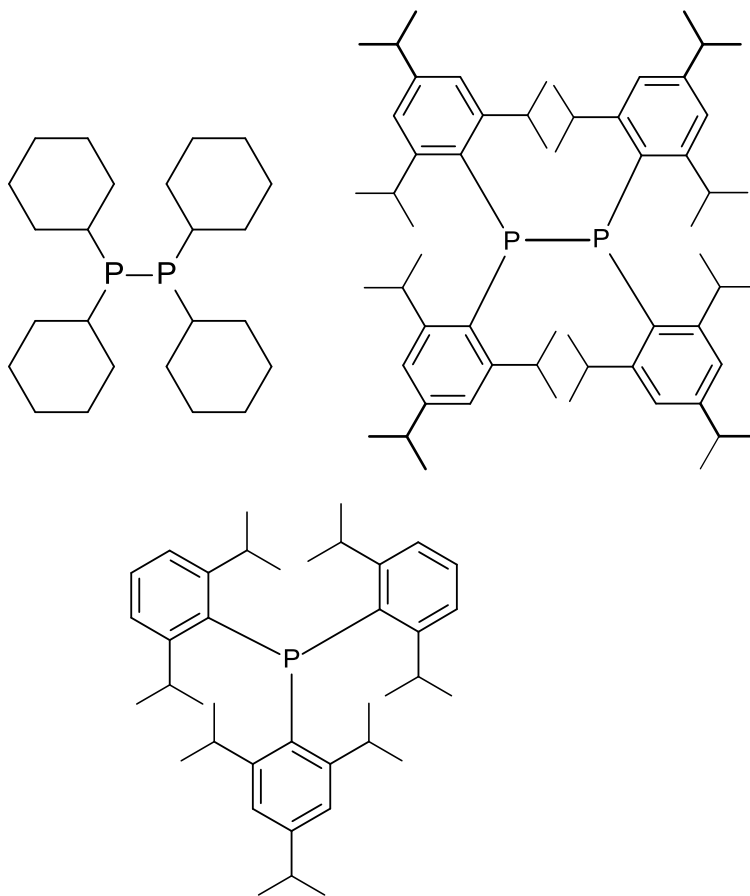
1. Sasaki, S.; Yoshifuji, M. *Curr. Org. Chem.* **2007**, *38*, 17.
2. Boéré, R. T.; Bond, A. M.; Cronin, S.; Duffy, N. W.; Hazendonk, P.; Masuda, J. D.; Pollard, K.; Roemmele, T. L.; Tran, P.; Zhang, Y. *New J. Chem.* **2008**, *32*, 214.
3. Boéré, R. T.; Gietz, T. *Unpublished results*.
4. Boéré, R. T.; Price, B. *Unpublished results*.
5. Symons, M. C. R.; Tordo, P.; Wyatt, J. *J. Org. Chem.* **1993**, *443*, C29.
6. Huheey, J. E.; Keiter, R. L. *Inorganic Chemistry*. 4th ed.; Harper Collins 1993.
7. Connelly, N. G.; Geiger, W. E. *Chem. Rev.* **1996**, *96*, 877.
8. Murphy, D. M., EPR (Electron Paramagnetic Resonance) Spectroscopy of Polycrystalline Oxide Systems. In *Metal Oxide Catalysis*, Wiley-VCH Verlag GmbH & Co. KGaA: 2009; pp 1.
9. Bennati, M.; Murphy, D. M., Electron Paramagnetic Resonance Spectra in the Solid State. In *Electron Paramagnetic Resonance*, John Wiley & Sons, Inc.: 2008; pp 195.
10. Weil, J. A.; Bolton, J. R., Appendix H: Fundamental Constants, Conversion Factors, and Key Data. In *Electron Paramagnetic Resonance*, John Wiley & Sons, Inc.: 2006; pp 577.
11. Henri, V., *Volume Commémordtif Victor Henri, Contribution à l'étude de la structure moléculaire*. 1984; p 15.

Chapter 5

Future work

5.1 Introduction

There are two tetraorganodiphosphines (Cy_4P_2 and Tripp_4P_2) and one bulky triarylphosphine ($\text{TrippDipp}_2\text{P}$) which still have to be made to complete the series that helped to explore a better understanding of electrochemical patterns.



Scheme 5.1. Molecules still needed to complete the series.

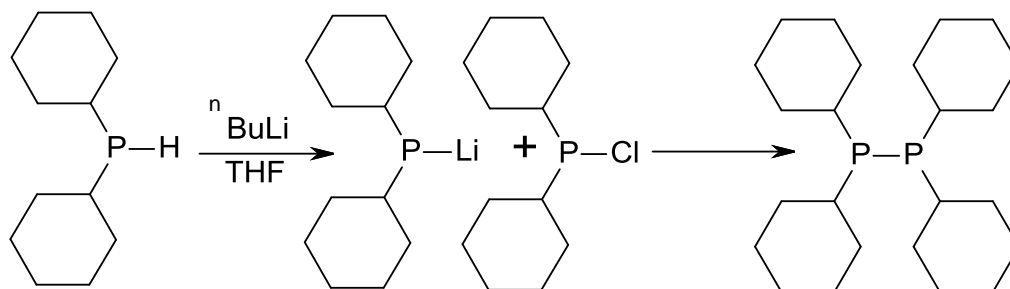
As mentioned in Chapter 3, attempts to prepare Tripp_4P_2 with different approaches did not give the desired results. Additionally, Cy_4P_2 can be a good choice as a diphosphine with less bulky group to get a better understanding of what should be seen from congested molecules to a molecule with more empty space. Finally, in chapter 4, a full electrochemical investigation on $\text{Tripp}_2\text{DippP}$ is reported. Therefore, having the $\text{TrippDipp}_2\text{P}$ can be an interesting compound to compare the results between these two and complete the full Dipp/Tripp series of triarylphosphines.

5.1.1 Future work on tetraorganodiphosphines

Several methods could be taken to synthesis Tripp_4P_2 , this bulky diphosphine as it has been fully discussed in Chapter 3. Future plan for synthesis of this compound is to follow the Brady approach¹ since this is one of the most common method to take for synthesis of tetraorganodiphosphine and also one more trial by using activated Mg as what it has been done for Dipp_4P_2 . Since these methods, all has been carried before this time, changing the condition and more care will be needed. For example, in reaction of Mg reaction using Li wire instead of dibromoethane to initiate the reaction to reduce the source of the hydrogen, which was the problem in this reaction (having more Tripp_2PH instead of Tripp_4P_2). If making this compound will be achieved, further studies by CV will expect to see the very similar two-oxidation process and even second oxidation can be more stable if no major geometry changes occurred after removing the second electron. Furthermore, solution and powder SEPR or EPR experiments will be run in addition to DFT calculation to prove the obtaining results from electrochemical studies. What has been expected to see is that in CV, $\text{Dipp}_4\text{P}_2^{+/0}$ found to be ~ 0.20 V less cathodic than the isosteric $\text{Tripp}_4\text{P}_2^{+/0}$ like what has been seen for Dipp_3P and Tripp_3P radical

cations.² The EPR parameters for both Dipp_4P_2 and Tripp_4P_2 radical cations will be expected to be similar but not identical.

In addition to the *tert*-butyl group, which favors an increase in the electron donating ability, introduction of cyclohexyl group will be interesting to compare the electrochemical data. 1,1,2,2-Tetracyclohexyldiphosphane will be prepared from Cy_2PH and Cy_2PCl using the method described in Scheme 5.2. Crystallization from methanol or propanol will be expected to give a white crystalline solid.³



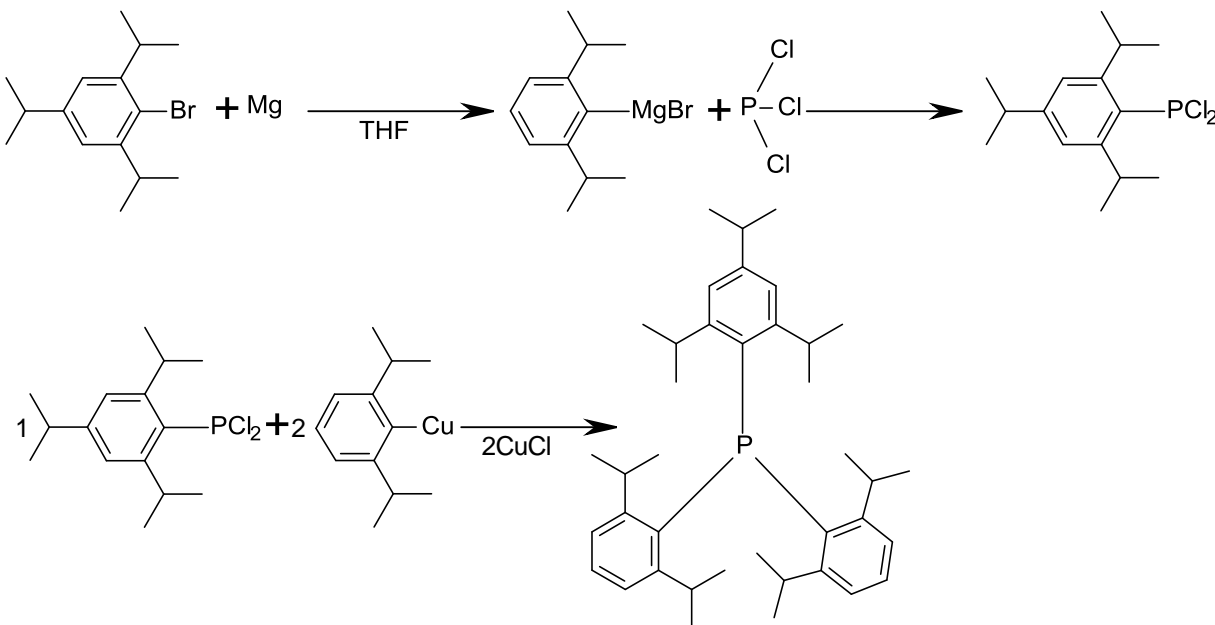
Scheme 5.2. Suggested synthesis route for Cy_4P_2

One of the interesting points in this compound is due to the different conformation, which will be expected to be *gauche*. How this geometry changes will affect the CV and EPR results could be investigated by carrying the experiment in the same condition with Dipp_4P_2 .

More interestingly, is a diphosphine with $\text{CH}(\text{SiMe}_3)_2$ as an R group. As it has been discussed in Section 1.3 this diphosphine behaves as an energy storage reservoir which P–P bond will be cleaved upon dissolution, melting or evaporation, in contrast with other diphosphines and specially my diphosphine. In case of Dipp_4P_2 , heating even above the melting point in the EPR did not break the P–P bond. The interesting study which it is worth doing, is to see what happens to the EPR signal after cleavage of the P–P bond.

5.1.2 Future work on triarylphosphines

Further work on triaryldiphosphines can be continued by synthesis of TrippDipp₂P with same approach, which was taken for Tripp₂DippP.



Scheme 5.3. Suggested method for synthesis of TrippDipp₂P

For this purpose, TrippPCl₂ could be prepared by reaction of the Grignard reagent with PCl₃ and then the final reaction with DippCu should result in the desired compound. Based on experience with this kind of reaction, the second step would not be straightforward. Sometimes it worked very well and sometimes the last-stage reflux took a couple of weeks until all the TrippPCl₂ changes to TrippDipp₂P. After having this compound on hand, crystallography and full NMR studies will be the first thing to do since this will be a new compound and then CV and EPR(SEEPR) and also DFT calculation will be followed like Tripp₂DippP. It will be very interesting to complete fully the entries in Table 4.1 and make a full comparison between these compounds and at long last confirm the pattern between oxidation potentials and EPR parameters.

5.2 Conclusion

In this project, the successful use of the electrochemical instruments has allowed for the effective investigation of a variety of compounds. For example, several phosphorus-containing compounds were investigated systematically, both by voltammetry and by SEEPR. The excellent results obtained in this work indicate that SEEPR is a promising technique for the characterization of related radical cations and the resulting trends seen in both the voltammetry and SEEPR studies explore the different behavior of the phosphorus lone pair in these compounds that is appeared with different and novel patterns in spectra. Due to the complex spectral patterns observed for the compounds reported in this thesis, some advanced concepts in EPR have been investigated. The determination of the key structural parameter (degree of pyramidalization) for several pnictogen radical cations which will be difficult or impossible to isolate is a key achievement of this work.

References

1. Brady, F. J.; Cardin, C. J.; Cardin, D. J.; Wilcock, D. J. *Inorg. Chim. Acta.* **2000**, 298, 1.
2. Boéré, R. T.; Bond, A. M.; Cronin, S.; Duffy, N. W.; Hazendonk, P.; Masuda, J. D.; Pollard, K.; Roemmele, T. L.; Tran, P.; Zhang, Y. *New J. Chem.* **2008**, 32, 214.
3. Dodds, D. L.; Haddow, M. F.; Orpen, A. G.; Pringle, P. G.; Woodward, G. *Organometallics.* **2006**, 25, 5937.

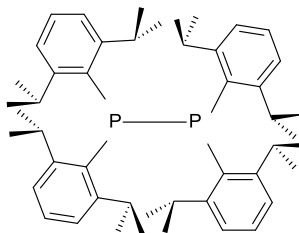
Chapter 6

Experimental

6.1 General procedures for synthesis

Unless otherwise stated, all work was carried out under a dry nitrogen atmosphere, using standard Schlenk techniques or an MBraun Glove box. 1.6M ⁿBuLi in hexanes (Aldrich) and all the phosphines (Aldrich) were used as received. Magnesium turnings (Aldrich) were stored in a glove box. Solvents for synthesis were collected from a Solvent Purification System (MBraun) or distilled under an N₂ atmosphere and degassed by the freeze-pump-thaw method. Drying agents for solvent purification included sodium/benzophenone (tetrahydrofuran), sodium (xylene), NaOH (isopropanol) and I₂/Mg (methanol). Air-sensitive liquid reagents were weighed in the glove box under protection from N₂ by using syringes whose mass was determined before and after filling. ¹H, ¹³C and ³¹P NMR spectra were recorded on a 300 MHz Bruker Avance II spectrometer (¹H 300.138 MHz, ¹³C 75.468 MHz, ³¹P 121.495 MHz) and referenced relative to 0 ppm for TMS (¹H, ¹³C) using either deuterated chloroform or deuterated benzene as secondary references, or relative to external 85% H₃PO₄ (³¹P). Elemental analyses were performed using an Elementar Americas Vario MicroCube instrument. Dipp₂PCl,¹ Tripp₂DippP¹ and Dipp₃As² have been previously prepared in this laboratory, were all characterized by single-crystal X-ray diffraction, and have their purity established by multinuclear NMR.

6.1.1 Preparation of tetrakis(2,6-diisopropylphenyl)diphosphine:



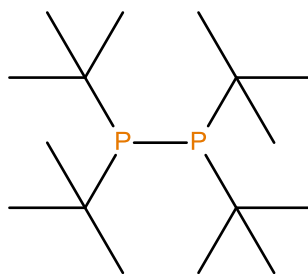
In a 250 mL side arm flask, 0.7 g (28.80 mmol, 25 times excess) of freshly ground Mg turnings (weighed in the glove box) were stirred under vacuum at 80 °C for 1 hour. 60 mL THF was added at RT. 0.9 g (2.31 mmol) *bis*(2,6-diisopropylphenyl)phosphorus chloride was added and the reaction mixture refluxed for 2 hr. Unlocked ^{31}P NMR (proton coupled and decoupled) showed two peaks at this step; singlet at -38 ppm which is belong to Dipp_4P_2 and minor doublet at $-102, -103$ ppm which belongs to the Dipp_2PH coupled to one H. filtered though celite and all solvent were removed under vacuum. The resulting yellow solid was taken up in a minimum of hot degassed isopropanol and cooled to -30 °C. Analytically pure crystals were obtained by recrystallization after one night. Filtered through the filter stick under the N_2 , solvent removed under the vacuum and crystals collected and kept under the glove box. Yield: 76% Melting Point: $165-173$ °C. ^1H NMR (C_6D_6): δ 0.36 (d, 6H), δ 0.46 (d, 6H), δ 0.70 (d, 6H), δ 0.84 (d, 6H), δ 1.38 (d, 6H), δ 1.41 (d, 6H), δ 1.46 (d, 6H), δ 1.47 (d, 6H), δ 3.93 (sept, 2H), δ 4.07 (sept, 2H), δ 4.29 (sept, 2H), δ 5.24 (d of sept, 2H), δ 7.04 -7.25 (m, 12H).

^{13}C NMR (C_6D_6): δ 24.69 s, δ 24.53 s, δ 23.51 s, δ 24.48 s, δ 26.19 s, δ 25.98 s, δ 23.14 s, δ 24.91 s, δ 33.25 t, δ 32.80 t, δ 32.17 t, δ 33.41 s, δ 126.82 s, δ 124.91 t, δ 127.21 s, δ 33.25t, δ 130.58 s, δ 129.62 s, δ 135.49 t, δ 134.72 t, δ 154.82 s, δ 154.82 s, δ 156.22 t, δ 155.36 t.

^{31}P NMR (C_6D_6): δ -38 s.

Elemental Analysis: Calc. for $\text{C}_{48}\text{H}_{68}\text{P}_2$: C, 74.97; H, 8.91. Found: C, 75.10; H, 9.33 %.

6.1.2 Preparation of 1,1-Di-*tert*-butyl-2,2-diphenyldiphosphine:



A solution of 0.5 g ${}^t\text{Bu}_2\text{PH}$ (3.41 mmol) in 20 mL THF was cooled with an ethanol/dry ice bath to approximately $-78\text{ }^\circ\text{C}$. Drop wise, 3.4 mL $n\text{-BuLi}$ (1.6 M solution in hexanes, 3.41 mmol) was added resulting in a yellow solution. After 30 min, the resulting solution was warmed to room temperature and stirred for 2 hr at RT. Unlocked $\{^{31}\text{P}\}^1\text{H}$ NMR spectrum showed one singlet peak at 39 ppm which is belong to ${}^t\text{Bu}_2\text{PLi}$. The solution was then cooled to $-78\text{ }^\circ\text{C}$, 0.61 g ${}^t\text{Bu}_2\text{PCl}$, weighted in the glove box (3.41 mmol), was added by syringe, and the solution was stirred overnight. In the morning, unlocked $\{^{31}\text{P}\}^1\text{H}$ NMR spectrum was carried on the white solution with white solids (LiCl); one major singlet peak at 38 ppm and minor doublet peak at 18 ppm.

The solvent was removed under vacuum to leave the white solid. Product extracted with degassed pentane ($3\times 20\text{ mL}$), LiCl was filtered through the celite and colorless solution was dried under the vacuum. Resulting white solids were dissolved in a minimum of hot and degassed methanol and cooled to $-30\text{ }^\circ\text{C}$. Analytically pure crystals were obtained by recrystallization after one night. Filtered through the filter stick, solvent removed under the vacuum and crystals collected and stored in the glove box for further use in electrochemistry and EPR spectroscopy. NMR data for this compound match the literature data.³

6.2 X-ray crystal structure of Dipp₄P₂

A single crystal of Dipp₄P₂, block shaped, coated in Paratone oil and mounted on a glass fiber cooled to -100 °C in order to reduce thermal motion, a particular source of disorders. Data was collected on a Bruker Apex II CCD area detector diffractometer using phi-scans. The structure was solved by using Dual-Space methods using SHELX-M, and refined using SHELX-S by standard full-matrix least squares methods. Search for higher symmetry indicates the cell is centrosymmetric which is compatible with E-statistics that favor a centrosymmetric space group and the molecule crystallized in the monoclinic space group P2₁/c (#14), with 4 molecules per unit cell which is standard for this space group (general position). The reflection intensities show good completeness (99.8 %) down to resolution of 0.77 Å⁻¹. R₁ = 0.0494, wR₂ = 0.1138 show that there is a good agreement between F_{obs} and F_{calc}, in other words, the model produced fits the data well. The R_{int} = 0.05 (5%) parameter provides a residual (fractional disagreement) between data that ought to be equivalent by symmetry. There are no intermolecular contacts less than the sum of van der Waals radii. The goodness of fit S or GOF defined as a standard deviation of an observation of unit weight has a value close to one, which means that refinement of the weighting scheme is appropriate. A final difference Fourier map was calculated and it shows no significant electron density peaks or holes.

6.3 Electrochemistry experimental

Dichloromethane (CH₂Cl₂) and acetonitrile (CH₃CN) (BDH, reagent grade) were purified by distillation (CH₃CN: over first P₂O₅, then CaH₂, CH₂Cl₂: over CaH₂). All solvents were purged with dry nitrogen or dry argon prior to use. Electrochemical grade tetra-n-butylammonium hexafluorophosphate [ⁿBu₄N][PF₆] (Fluka) was used as the supporting electrolyte and was kept in a dessicator prior to use. *Bis*(cyclopentadienyl)cobalt(III)

hexafluorophosphate (Aldrich) potential reference. All samples weighted in the pre-weighted vial in the glove box before transferring to the cell.

6.3.1 Cyclic voltammetry procedure

Cyclic voltammograms (CVs) were obtained at room temperatures mostly in CH_2Cl_2 and in case of low solubility in CH_3CN solutions containing 0.5 M $[\text{nBu}_4\text{N}][\text{PF}_6]$ as the supporting electrolyte. These solutions were purged with dry nitrogen or argon for 10 minutes directly prior to use, and argon gas purge between each scan rates through the solution to prevent of exposure to air during all experiments. The cell design utilized a conventional three electrode setup with a 3.0 mm diameter glassy carbon (GC) working electrode, a Pt wire auxiliary and a silver wire quasi-reference electrode. The reference electrode was separated from the bulk solution by a 1.0–1.6 μm porosity frit. Experiments commence with initial background scans characterized the size of the electrochemical window and provided an estimate of the likely background current which was 2(2.5) to $-2(-2.5)$ for CH_2Cl_2 for all samples. CV's were obtained over scan rates of 0.050 – 20 V s^{-1} . All potentials are reported versus the operative formal potential, $E_{\text{Fc}^{+/0}}^\circ$, for the $\text{Fc}^{+/0}$ redox couple. The $\text{Cc}^{+/0}$ (Cc = cobaltocene) redox couple is known to appear at -1.35 V in CH_2Cl_2 , have been converted to the $\text{Fc}^{+/0}$ scale by subtraction of 1.35 V.⁴ The working electrode was polished with a 0.3 micron Al_2O_3 (Buehler, 0.05 μm) slurry on a clean polishing cloth, rinsed with distilled water and acetone, and dried with tissue paper prior to use and sometimes during the experiments.

6.3.2 Rotating disk electrode (RDE) voltammetry procedure

For Dipp_4P_2 , $\text{Tripp}_2\text{DippP}$ and Dipp_3As RDE voltammetry measurements were performed with a Princeton Applied Research PARSTAT 2273 potentiostat in conjunction with a PINE

Model AFMSRXE Modulated Speed Rotator. The cell used for RDE measurements replaced the central size-10 joint with a 60×15 mm cylinder to accommodate the rotating electrode. A 5.0 mm diameter GC macrodisc electrode (area = $1.86 \times 10^{-1} \text{ cm}^2$) was employed for RDE voltammetry. Diffusion coefficients were determined from limiting current values obtained from RDE voltammetry and use of the Levich Eq. 2.2.⁵ Values for the kinematic viscosity (ν_k) at 20 °C were taken to be $0.003318 \text{ cm}^2\text{s}^{-1}$ for the pure CH_2Cl_2 solvent.⁶ Diffusion coefficient values of corresponding compounds are found in Chapter 2 and 3. Figure 6.1 shows the RDE cell after electrolysis; blue solution contains the $\text{Dipp}_4\text{P}_2^{+/0}$ and red solution contains $\text{Dipp}_3\text{As}^{+/0}$.



Figure 6.1. RDE cell containing $[\text{Dipp}_4\text{P}_2]^{+/0}$ (blue solution) and $[\text{Dipp}_3\text{As}]^{+/0}$ (red solution)

6.3.3 Variable temperature SEPR investigations

Variable temperature SEPR experiments were conducted on compounds Dipp_4P_2 and $\text{Tripp}_2\text{DippP}$ on a Bruker EMX 113 spectrometer operating at X-band frequencies (9.8 GHz). These studies employed a miniature quartz flat cell incorporating modified working, auxiliary, and reference electrodes, which are all, fed in from the top of the cell. The working electrode was either platinum or gold foil electrode, which was in contact with a thin copper foil. The auxiliary electrode was 0.5 mm platinum wire, and the reference electrode was coated silver wire, which

was Teflon-coated and allowed for exposure of the metal near to the working electrode. Solutions containing both the analyte and electrolyte were loaded into the flat cell (ca. 0.5 mL) via a modified Schlenk tube, along with the electrodes to seal the cell. These experiments in case of both compounds were a mixture of in situ and ex situ type EPR. Both compounds were oxidized upon taking to the solvent and their color changing (Figure 6.2). Background EPR spectra were obtained prior to electrolysis but with the cell inside the EPR cavity which shows a very low resolution signal of cation in both compounds. After a close to one hour, once again spectra obtained which indicated most of the radicals are gone. CV studies were then applied to determine the exact potential for the oxidation process versus the reference electrode in this cell, and controlled potential electrolysis experiments were carried on with the potential set to ~ 0.45 V for Dipp_4P_2 and 0.5 V for $\text{Tripp}_2\text{DippP}$ more positive than the peak potential for the redox couple of interest. Scans were then obtained simultaneously with electrolysis and continuing electrolysis until maximum signal intensity was obtained. The temperature of the sample can be held within close tolerances by a heating element that warms the gas to the desired temperature. Figure 6.2 illustrated the SEEPR cell for $[\text{Dipp}_4\text{P}_2]^+$ and $[\text{Tripp}_2\text{DippP}]^+$



Figure 6.2. SEEPR cell containing (a) $[\text{Dipp}_4\text{P}_2]^{++}$ and (b) $[\text{Tripp}_2\text{DippP}]^{++}$

For Dipp_4P_2 , SEEPR experiments were conducted in $\text{CH}_2\text{Cl}_2/0.4 \text{ M } [^n\text{Bu}_4\text{N}][\text{PF}_6]$ at temperatures between 0 and 20 °C and $\text{Tripp}_2\text{DippP}$ between -70 and 0 °C. Spectra were monitored in intensity-versus-field mode during electrolysis. Simulations of EPR spectra and reported parameters were obtained from complete digital line-fitting routines using Bruker Simfonia (version 1.25). Spectral parameters for Dipp_4P_2 in CH_2Cl_2 : conversion times (CT) = 81.92 ms, sweep width (SW) = 0.1 mT, modulation amplitude (MA) = 0.5 mT. Spectral parameters for $\text{Tripp}_2\text{DippP}$ in CH_2Cl_2 : conversion times (CT) = 81.92 ms, sweep width (SW) = 0.1 mT, modulation amplitude (MA) = 0.5 mT.

6.3.4 EPR experiment by chemical oxidation



Figure 6.3. “T” cell for chemical oxidation EPR experiment containing AgPF_6 and $\text{Tripp}_2\text{DippP}$

Sample prepared by the addition of an excess of AgPF_6 to Dipp_4P_2 and $\text{Tripp}_2\text{DippP}$ and AgSbF_6 to solid Dipp_3As in “T” cells (Figure 6.3) consisting of a 4 mm Pyrex EPR tube fused at a 75° angle to an 8 mm Pyrex reaction tube. Degassed CH_2Cl_2 was vacuum distilled onto the solid mixture, and the tube was flame sealed. Upon melting, an immediate colour change was observed. The EPR cell was filled and the concentration was reduced by internal distillation of the solvent so that the spectra were close to the detection limit of the instrument. In this way, the effect of concentration broadening on the EPR line widths was assumed to be eliminated. These spectra were obtained on a Bruker EMX Plus/10 instrument operating at X band starting point at 0°C . Modulation amplitude was varied between 1 to 5 G to get better signal to noise for each experiment and sweep width was varied between 700–1000 G. Low temperature experiments were conducted by attaching the cold nitrogen gas accessory (which is attached to a liquid

nitrogen Dewar) to the instrument. Spectral parameters for Dipp₄P₂ in CH₂Cl₂: conversion times (CT) = 5.12 ms, sweep width (SW) = 0.7 mT, modulation amplitude (MA) = 0.5 mT. Spectral parameters for Tripp₂DippP in CH₂Cl₂: conversion times (CT) = 5.12 ms, sweep width (SW) = 0.7 mT, modulation amplitude (MA) = 0.5 mT.

6.3.5 Calculation details

Full geometry optimizations were performed at the B3LYP/6-31G(d) (for bulky compounds) and 6-311G++(3df,2p) (for small molecules) levels of theory. Structures of the radical cations were obtained after starting from the DFT optimized neutral molecule geometries. The results of the frequency calculations were used to correct the zero-point energies of all species. Non-relativistic hyperfine splitting (HFS) constants were calculated for the radical cations using the unrestricted Kohn-Sham formalism, employing the same basis sets and density functional as for the geometry optimizations. In case of Dipp₄P₂, isotropic hyperfine splitting has been obtained by adding `op(6/82=1)` command to the calculation. This is apparently only necessary when there are more than 100 atoms.

References

1. Boéré, R. T.; Gietz, T. *Unpublished results*.
2. Boéré, R. T.; Price, B. *Unpublished results*.
3. Dodds, D. L.; Haddow, M. F.; Orpen, A. G.; Pringle, P. G.; Woodward, G. *Organometallics*. **2006**, *25*, 5937.
4. Stojanovic, R. S.; Bond, A. M. *Anal. Chem.* **1993**, *65*, 56.
5. Bard, A. J.; Faulkner, L. R. *Electrochemical Methods: Fundamentals and Applications*. 2nd ed.; Wiley: New York, 2001.
6. Nath, J.; Dixit, A. P. *J. Chem. Eng. Data*. **1984**, *29*, 317.

Appendix

Table A1. Crystal data and structure refinement for Dipp₄P₂

Empirical formula	C ₄₈ H ₆₈ P ₂	
Formula weight	706.96	
Temperature	173(2) K	
Wavelength	0.71073 Å	
Crystal system	Monoclinic	
Space group	P2 ₁ /c	
Unit cell dimensions	a = 13.3256(13) Å	α = 90.0000°
	b = 18.4854(19) Å	β = 99.2750(10)°
	c = 17.5047(18) Å	γ = 90.0000°
Volume	4255.5(7) Å ³	
Z	4	
Density (calculated)	1.103 Mg/m ³	
Absorption coefficient	0.133 mm ⁻¹	
F(000)	1544	
Crystal size	0.14 x 0.19 x 0.20 mm ³	
Theta range for data collection	1.61 to 27.50°.	
Index ranges	-17<=h<=17, -23<=k<=24, -22<=l<=22	
Reflections collected	60064	
Independent reflections	9764 [R(int) = 0.0504]	
Completeness to theta = 27.50°	99.9 %	
Refinement method	Full-matrix least-squares on F ²	
Data / restraints / parameters	9764 / 0 / 467	
Goodness-of-fit on F ²	1.032	
Final R indices [I>2sigma(I)]	R1 = 0.0494, wR2 = 0.1138	
R indices (all data)	R1 = 0.0740, wR2 = 0.1276	
Largest diff. peak and hole	0.822 and -0.384 e.Å ⁻³	

Table A2. Atomic coordinates (x 10⁴) and equiv. isotr. displ. Param. (Å² x 10³) for Dipp₄P₂ *

	x	y	z	U(eq)
P(1)	7339(1)	-111(1)	2939(1)	22(1)
P(2)	7826(1)	568(1)	2017(1)	20(1)
C(1)	9217(1)	446(1)	1991(1)	22(1)
C(2)	9499(1)	807(1)	1340(1)	28(1)
C(3)	8790(2)	1298(1)	799(1)	34(1)
C(4)	9119(2)	2085(1)	884(2)	60(1)
C(5)	8659(2)	1045(2)	-37(1)	55(1)
C(6)	10489(2)	742(1)	1185(1)	39(1)
C(7)	11198(2)	322(1)	1638(1)	44(1)
C(8)	10932(1)	-29(1)	2265(1)	37(1)
C(9)	9960(1)	20(1)	2467(1)	26(1)
C(10)	9826(1)	-386(1)	3201(1)	31(1)
C(11)	10589(2)	-136(1)	3907(1)	44(1)
C(12)	9935(2)	-1206(1)	3128(1)	42(1)
C(13)	7322(1)	-1090(1)	2659(1)	24(1)
C(14)	7496(1)	-1426(1)	1958(1)	26(1)
C(15)	7661(1)	-1047(1)	1215(1)	30(1)
C(16)	8729(2)	-1176(1)	1018(1)	38(1)
C(17)	6888(2)	-1275(1)	507(1)	44(1)
C(18)	7532(1)	-2181(1)	1930(1)	35(1)
C(19)	7424(2)	-2607(1)	2552(1)	40(1)
C(20)	7261(1)	-2285(1)	3231(1)	37(1)
C(21)	7203(1)	-1538(1)	3299(1)	28(1)
C(22)	6998(2)	-1247(1)	4075(1)	34(1)
C(23)	7844(2)	-1440(2)	4731(2)	73(1)
C(24)	5975(2)	-1488(2)	4251(2)	64(1)
C(25)	5974(1)	139(1)	2919(1)	23(1)
C(26)	5787(1)	582(1)	3547(1)	29(1)
C(27)	6607(2)	994(1)	4077(1)	36(1)
C(28)	6735(2)	715(2)	4910(1)	50(1)
C(29)	6386(2)	1804(1)	4053(1)	46(1)
C(30)	4791(2)	663(1)	3686(1)	40(1)
C(31)	3985(2)	330(1)	3230(1)	42(1)
C(32)	4158(1)	-70(1)	2601(1)	36(1)
C(33)	5135(1)	-164(1)	2426(1)	26(1)
C(34)	5215(1)	-581(1)	1692(1)	27(1)
C(35)	4913(2)	-1377(1)	1759(1)	36(1)
C(36)	4562(2)	-236(1)	983(1)	36(1)
C(37)	7699(1)	1506(1)	2384(1)	22(1)
C(38)	8433(1)	1874(1)	2917(1)	26(1)
C(39)	9321(1)	1504(1)	3415(1)	29(1)
C(40)	10333(1)	1743(1)	3179(1)	36(1)
C(41)	9339(2)	1664(1)	4277(1)	42(1)
C(42)	8352(2)	2620(1)	2997(1)	34(1)
C(43)	7567(2)	3005(1)	2582(1)	38(1)
C(44)	6821(1)	2646(1)	2093(1)	32(1)
C(45)	6863(1)	1902(1)	1988(1)	25(1)
C(46)	5979(1)	1561(1)	1449(1)	30(1)
C(47)	4976(1)	1690(1)	1749(1)	37(1)
C(48)	5916(2)	1843(1)	623(1)	45(1)

* U(eq) is defined as one third of the trace of the orthogonalized U^{ij} tensor.

Table A3. Bond lengths [\AA] and angles [$^\circ$] for Dipp_4P_2

P(1)–C(25)	1.8711(17)	C(25)–P(1)–C(13)	105.29(8)
P(1)–C(13)	1.8740(18)	C(25)–P(1)–P(2)	104.08(6)
P(1)–P(2)	2.2233(6)	C(13)–P(1)–P(2)	110.31(6)
P(2)–C(37)	1.8658(17)	C(37)–P(2)–C(1)	105.37(7)
P(2)–C(1)	1.8753(17)	C(37)–P(2)–P(1)	102.77(5)
C(1)–C(2)	1.421(2)	C(1)–P(2)–P(1)	110.83(6)
C(1)–C(9)	1.424(2)	C(2)–C(1)–C(9)	118.72(15)
C(2)–C(6)	1.395(3)	C(2)–C(1)–P(2)	110.65(13)
C(2)–C(3)	1.524(3)	C(9)–C(1)–P(2)	130.42(13)
C(3)–C(5)	1.519(3)	C(6)–C(2)–C(1)	119.70(17)
C(3)–C(4)	1.520(3)	C(6)–C(2)–C(3)	116.22(17)
C(6)–C(7)	1.373(3)	C(1)–C(2)–C(3)	124.04(16)
C(7)–C(8)	1.370(3)	C(5)–C(3)–C(4)	112.02(19)
C(8)–C(9)	1.399(2)	C(5)–C(3)–C(2)	112.26(17)
C(9)–C(10)	1.524(3)	C(4)–C(3)–C(2)	111.60(18)
C(10)–C(12)	1.530(3)	C(7)–C(6)–C(2)	121.44(19)
C(10)–C(11)	1.539(3)	C(8)–C(7)–C(6)	119.17(18)
C(13)–C(21)	1.424(3)	C(7)–C(8)–C(9)	122.78(19)
C(13)–C(14)	1.426(3)	C(8)–C(9)–C(1)	118.18(17)
C(14)–C(18)	1.397(3)	C(8)–C(9)–C(10)	114.85(16)
C(14)–C(15)	1.525(3)	C(1)–C(9)–C(10)	126.95(15)
C(15)–C(16)	1.535(3)	C(9)–C(10)–C(12)	112.99(17)
C(15)–C(17)	1.538(3)	C(9)–C(10)–C(11)	112.13(17)
C(18)–C(19)	1.371(3)	C(12)–C(10)–C(11)	107.81(16)
C(19)–C(20)	1.376(3)	C(21)–C(13)–C(14)	118.49(17)
C(20)–C(21)	1.389(3)	C(21)–C(13)–P(1)	110.72(13)
C(21)–C(22)	1.526(3)	C(14)–C(13)–P(1)	130.51(14)
C(22)–C(24)	1.513(3)	C(18)–C(14)–C(13)	118.55(17)
C(22)–C(23)	1.517(3)	C(18)–C(14)–C(15)	114.70(17)
C(25)–C(33)	1.414(2)	C(13)–C(14)–C(15)	126.74(16)
C(25)–C(26)	1.424(2)	C(14)–C(15)–C(16)	112.73(16)
C(26)–C(30)	1.395(3)	C(14)–C(15)–C(17)	113.02(16)
C(26)–C(27)	1.520(3)	C(16)–C(15)–C(17)	107.55(16)
C(27)–C(29)	1.525(3)	C(19)–C(18)–C(14)	122.40(19)
C(27)–C(28)	1.530(3)	C(18)–C(19)–C(20)	119.32(19)
C(30)–C(31)	1.376(3)	C(19)–C(20)–C(21)	121.48(19)
C(31)–C(32)	1.377(3)	C(20)–C(21)–C(13)	119.74(18)
C(32)–C(33)	1.396(2)	C(20)–C(21)–C(22)	116.62(17)
C(33)–C(34)	1.517(3)	C(13)–C(21)–C(22)	123.64(17)
C(34)–C(35)	1.535(3)	C(24)–C(22)–C(23)	111.1(2)
C(34)–C(36)	1.535(3)	C(24)–C(22)–C(21)	111.95(16)
C(37)–C(38)	1.414(2)	C(23)–C(22)–C(21)	111.89(19)
C(37)–C(45)	1.417(2)	C(33)–C(25)–C(26)	118.63(15)
C(38)–C(42)	1.392(3)	C(33)–C(25)–P(1)	125.71(13)
C(38)–C(39)	1.515(3)	C(26)–C(25)–P(1)	114.76(13)
C(39)–C(41)	1.534(3)	C(30)–C(26)–C(25)	119.11(17)
C(39)–C(40)	1.538(3)	C(30)–C(26)–C(27)	116.74(17)
C(42)–C(43)	1.373(3)	C(25)–C(26)–C(27)	124.14(16)
C(43)–C(44)	1.373(3)	C(26)–C(27)–C(29)	111.02(17)
C(44)–C(45)	1.389(3)	C(26)–C(27)–C(28)	111.86(18)
C(45)–C(46)	1.522(2)	C(29)–C(27)–C(28)	110.39(18)
C(46)–C(48)	1.527(3)	C(31)–C(30)–C(26)	121.75(19)
C(46)–C(47)	1.532(3)	C(30)–C(31)–C(32)	119.27(18)

C(31)–C(32)–C(33)	121.62(18)	C(38)–C(39)–C(41)	111.46(16)
C(32)–C(33)–C(25)	119.42(17)	C(38)–C(39)–C(40)	110.66(16)
C(32)–C(33)–C(34)	116.34(16)	C(41)–C(39)–C(40)	109.52(15)
C(25)–C(33)–C(34)	124.22(15)	C(43)–C(42)–C(38)	121.66(18)
C(33)–C(34)–C(35)	111.57(15)	C(42)–C(43)–C(44)	119.53(18)
C(33)–C(34)–C(36)	111.47(15)	C(43)–C(44)–C(45)	121.35(18)
C(35)–C(34)–C(36)	109.77(15)	C(44)–C(45)–C(37)	119.47(17)
C(38)–C(37)–C(45)	118.68(16)	C(44)–C(45)–C(46)	116.66(16)
C(38)–C(37)–P(2)	125.65(13)	C(37)–C(45)–C(46)	123.86(16)
C(45)–C(37)–P(2)	114.84(12)	C(45)–C(46)–C(48)	111.38(17)
C(42)–C(38)–C(37)	119.11(17)	C(45)–C(46)–C(47)	110.67(16)
C(42)–C(38)–C(39)	117.10(16)	C(48)–C(46)–C(47)	110.69(15)
C(37)–C(38)–C(39)	123.79(16)		

Table A4. Anisotropic displacement parameters ($\text{\AA}^2 \times 10^3$) for Dipp₄P₂ *

U ¹¹	U ²²	U ³³	U ²³	U ¹³	U ¹²
P(1)18(1)	24(1)	23(1)	1(1)	5(1)	0(1)
P(2)19(1)	20(1)	23(1)	0(1)	5(1)	0(1)
C(1)19(1)	22(1)	27(1)	-5(1)	7(1)	-2(1)
C(2)28(1)	29(1)	28(1)	-3(1)	10(1)	0(1)
C(3)36(1)	40(1)	31(1)	8(1)	15(1)	5(1)
C(4)87(2)	42(1)	54(2)	18(1)	15(1)	2(1)
C(5)56(2)	77(2)	32(1)	1(1)	7(1)	14(1)
C(6)33(1)	52(1)	37(1)	3(1)	18(1)	0(1)
C(7)26(1)	62(2)	49(1)	-1(1)	18(1)	5(1)
C(8)22(1)	44(1)	44(1)	0(1)	5(1)	8(1)
C(9)22(1)	27(1)	31(1)	-3(1)	4(1)	0(1)
C(10)23(1)	36(1)	34(1)	6(1)	3(1)	7(1)
C(11)41(1)	50(1)	38(1)	7(1)	-6(1)	6(1)
C(12)32(1)	38(1)	54(1)	11(1)	4(1)	6(1)
C(13)17(1)	22(1)	33(1)	1(1)	3(1)	0(1)
C(14)20(1)	25(1)	35(1)	-1(1)	6(1)	1(1)
C(15)34(1)	27(1)	31(1)	-4(1)	9(1)	3(1)
C(16)37(1)	42(1)	38(1)	-4(1)	16(1)	-1(1)
C(17)41(1)	54(1)	35(1)	-11(1)	4(1)	6(1)
C(18)30(1)	27(1)	49(1)	-5(1)	12(1)	1(1)
C(19)40(1)	21(1)	64(2)	0(1)	19(1)	2(1)
C(20)30(1)	31(1)	51(1)	12(1)	9(1)	-1(1)
C(21)19(1)	31(1)	33(1)	4(1)	2(1)	-3(1)
C(22)37(1)	35(1)	29(1)	5(1)	2(1)	-10(1)
C(23)67(2)	101(2)	43(1)	6(2)	-16(1)	-2(2)
C(24)55(2)	95(2)	48(1)	-22(1)	27(1)	-24(2)
C(25)19(1)	27(1)	25(1)	4(1)	9(1)	1(1)
C(26)27(1)	38(1)	26(1)	0(1)	9(1)	1(1)
C(27)29(1)	48(1)	31(1)	-9(1)	11(1)	-1(1)
C(28)49(1)	67(2)	33(1)	-6(1)	2(1)	3(1)
C(29)47(1)	50(1)	43(1)	-15(1)	16(1)	-3(1)
C(30)33(1)	56(1)	34(1)	-8(1)	15(1)	4(1)
C(31)23(1)	65(2)	43(1)	-5(1)	15(1)	1(1)
C(32)22(1)	48(1)	38(1)	-2(1)	6(1)	-2(1)
C(33)25(1)	29(1)	27(1)	4(1)	8(1)	0(1)
C(34)23(1)	31(1)	28(1)	-1(1)	4(1)	-2(1)
C(35)31(1)	35(1)	42(1)	0(1)	4(1)	-7(1)
C(36)36(1)	41(1)	32(1)	0(1)	1(1)	0(1)
C(37)22(1)	22(1)	23(1)	-1(1)	10(1)	0(1)
C(38)24(1)	28(1)	28(1)	-4(1)	11(1)	-2(1)
C(39)25(1)	35(1)	27(1)	-6(1)	4(1)	-4(1)
C(40)24(1)	42(1)	41(1)	-6(1)	3(1)	-6(1)
C(41)37(1)	58(2)	29(1)	-10(1)	4(1)	-4(1)
C(42)31(1)	31(1)	43(1)	-14(1)	11(1)	-7(1)
C(43)38(1)	22(1)	58(1)	-6(1)	18(1)	0(1)
C(44)32(1)	25(1)	42(1)	1(1)	10(1)	5(1)
C(45)26(1)	24(1)	28(1)	0(1)	9(1)	2(1)
C(46)28(1)	27(1)	34(1)	-2(1)	0(1)	8(1)
C(47)27(1)	35(1)	47(1)	3(1)	2(1)	4(1)
C(48)39(1)	60(2)	35(1)	-1(1)	2(1)	13(1)

* The anisotropic displacement factor exponent takes the form: $-2\pi^2 [h^2 a^{*2} U^{11} + \dots + 2 h k a^* b^* U^{12}]$

Table 5. Hydrogen coordinates (x 10⁴) and isotropic displacement parameters (Å²x 10³) for Dipp₄P₂

	x	y	z	U(eq)
H(3)	8106	1266	963	41
H(4A)	9794	2138	737	91
H(4B)	9145	2237	1423	91
H(4C)	8630	2387	547	91
H(5A)	9312	1077	-224	83
H(5B)	8159	1352	-356	83
H(5C)	8421	542	-69	83
H(6)	10676	993	756	47
H(7)	11866	277	1519	53
H(8)	11428	-318	2576	44
H(10)	9125	-284	3310	37
H(11A)	11279	-271	3835	66
H(11B)	10427	-367	4375	66
H(11C)	10548	391	3959	66
H(12A)	9415	-1386	2711	62
H(12B)	9849	-1438	3616	62
H(12C)	10611	-1319	3008	62
H(15)	7582	-515	1291	36
H(16A)	9240	-1049	1466	57
H(16B)	8825	-875	575	57
H(16C)	8803	-1687	889	57
H(17A)	6965	-1792	408	66
H(17B)	7008	-997	54	66
H(17C)	6197	-1181	608	66
H(18)	7636	-2407	1461	42
H(19)	7462	-3119	2516	49
H(20)	7187	-2581	3662	45
H(22)	6979	-707	4034	41
H(23A)	7885	-1967	4788	110
H(23B)	7703	-1224	5213	110
H(23C)	8492	-1255	4615	110
H(24A)	5974	-2015	4314	96
H(24B)	5441	-1349	3824	96
H(24C)	5847	-1258	4730	96
H(27)	7265	918	3884	43
H(28A)	6093	770	5109	76
H(28B)	7268	994	5234	76
H(28C)	6928	203	4922	76
H(29A)	6312	1976	3518	68
H(29B)	6949	2061	4369	68
H(29C)	5755	1896	4258	68
H(30)	4666	956	4106	48
H(31)	3317	375	3349	51
H(32)	3598	-287	2277	43
H(34)	5940	-566	1610	33
H(35A)	5343	-1597	2205	54
H(35B)	5005	-1635	1286	54
H(35C)	4199	-1406	1828	54
H(36A)	3841	-282	1029	55
H(36B)	4689	-482	513	55
H(36C)	4737	277	955	55
H(39)	9248	970	3335	35

H(40A)	10342	1605	2639	54
H(40B)	10898	1506	3514	54
H(40C)	10403	2269	3232	54
H(41A)	9468	2180	4374	62
H(41B)	9879	1380	4586	62
H(41C)	8682	1534	4422	62
H(42)	8854	2869	3347	41
H(43)	7539	3516	2633	46
H(44)	6266	2911	1820	39
H(46)	6099	1027	1441	36
H(47A)	5013	1472	2263	55
H(47B)	4417	1470	1393	55
H(47C)	4857	2212	1783	55
H(48A)	5832	2370	620	68
H(48B)	5333	1622	292	68
H(48C)	6542	1720	426	68

Table A6. Torsion angles [°] for Dipp₄P₂

C(25)–P(1)–P(2)–C(37)	63.67(8)	P(1)–C(13)–C(14)–C(18)	173.90(14)
C(13)–P(1)–P(2)–C(37)	176.18(8)	C(21)–C(13)–C(14)–C(15)	–178.82(16)
C(25)–P(1)–P(2)–C(1)	175.82(8)	P(1)–C(13)–C(14)–C(15)	–5.4(3)
C(13)–P(1)–P(2)–C(1)	–71.68(8)	C(18)–C(14)–C(15)–C(16)	–64.2(2)
C(37)–P(2)–C(1)–C(2)	–76.95(14)	C(13)–C(14)–C(15)–C(16)	115.13(19)
P(1)–P(2)–C(1)–C(2)	172.57(11)	C(18)–C(14)–C(15)–C(17)	58.0(2)
C(37)–P(2)–C(1)–C(9)	108.60(17)	C(13)–C(14)–C(15)–C(17)	–122.66(19)
P(1)–P(2)–C(1)–C(9)	–1.87(18)	C(13)–C(14)–C(18)–C(19)	–1.1(3)
C(9)–C(1)–C(2)–C(6)	–0.4(3)	C(15)–C(14)–C(18)–C(19)	178.34(18)
P(2)–C(1)–C(2)–C(6)	–175.59(15)	C(14)–C(18)–C(19)–C(20)	0.8(3)
C(9)–C(1)–C(2)–C(3)	–178.07(17)	C(18)–C(19)–C(20)–C(21)	0.0(3)
P(2)–C(1)–C(2)–C(3)	6.8(2)	C(19)–C(20)–C(21)–C(13)	–0.6(3)
C(6)–C(2)–C(3)–C(5)	59.9(2)	C(19)–C(20)–C(21)–C(22)	178.78(18)
C(1)–C(2)–C(3)–C(5)	–122.4(2)	C(14)–C(13)–C(21)–C(20)	0.3(2)
C(6)–C(2)–C(3)–C(4)	–66.8(2)	P(1)–C(13)–C(21)–C(20)	–174.35(14)
C(1)–C(2)–C(3)–C(4)	110.9(2)	C(14)–C(13)–C(21)–C(22)	–179.03(16)
C(1)–C(2)–C(6)–C(7)	1.4(3)	P(1)–C(13)–C(21)–C(22)	6.3(2)
C(3)–C(2)–C(6)–C(7)	179.2(2)	C(20)–C(21)–C(22)–C(24)	–62.9(2)
C(2)–C(6)–C(7)–C(8)	–1.1(3)	C(13)–C(21)–C(22)–C(24)	116.5(2)
C(6)–C(7)–C(8)–C(9)	0.0(3)	C(20)–C(21)–C(22)–C(23)	62.6(2)
C(7)–C(8)–C(9)–C(1)	0.9(3)	C(13)–C(21)–C(22)–C(23)	–118.0(2)
C(7)–C(8)–C(9)–C(10)	–177.6(2)	C(13)–P(1)–C(25)–C(33)	–30.95(17)
C(2)–C(1)–C(9)–C(8)	–0.7(3)	P(2)–P(1)–C(25)–C(33)	85.13(15)
P(2)–C(1)–C(9)–C(8)	173.40(15)	C(13)–P(1)–C(25)–C(26)	137.98(14)
C(2)–C(1)–C(9)–C(10)	177.67(17)	P(2)–P(1)–C(25)–C(26)	–105.94(13)
P(2)–C(1)–C(9)–C(10)	–8.3(3)	C(33)–C(25)–C(26)–C(30)	4.2(3)
C(8)–C(9)–C(10)–C(12)	–64.9(2)	P(1)–C(25)–C(26)–C(30)	–165.53(16)
C(1)–C(9)–C(10)–C(12)	116.7(2)	C(33)–C(25)–C(26)–C(27)	–174.42(17)
C(8)–C(9)–C(10)–C(11)	57.2(2)	P(1)–C(25)–C(26)–C(27)	15.8(2)
C(1)–C(9)–C(10)–C(11)	–121.2(2)	C(30)–C(26)–C(27)–C(29)	–57.6(2)
C(25)–P(1)–C(13)–C(21)	–79.39(13)	C(25)–C(26)–C(27)–C(29)	121.1(2)
P(2)–P(1)–C(13)–C(21)	168.88(10)	C(30)–C(26)–C(27)–C(28)	66.2(2)
C(25)–P(1)–C(13)–C(14)	106.81(16)	C(25)–C(26)–C(27)–C(28)	–115.1(2)
P(2)–P(1)–C(13)–C(14)	–4.92(17)	C(25)–C(26)–C(30)–C(31)	–0.4(3)
C(21)–C(13)–C(14)–C(18)	0.5(2)	C(27)–C(26)–C(30)–C(31)	178.4(2)

C(26)–C(30)–C(31)–C(32)	–2.8(4)	P(2)–C(37)–C(38)–C(39)	–15.2(2)
C(30)–C(31)–C(32)–C(33)	2.0(3)	C(42)–C(38)–C(39)–C(41)	55.7(2)
C(31)–C(32)–C(33)–C(25)	2.0(3)	C(37)–C(38)–C(39)–C(41)	–124.56(19)
C(31)–C(32)–C(33)–C(34)	–176.66(19)	C(42)–C(38)–C(39)–C(40)	–66.4(2)
C(26)–C(25)–C(33)–C(32)	–5.0(3)	C(37)–C(38)–C(39)–C(40)	113.30(19)
P(1)–C(25)–C(33)–C(32)	163.53(15)	C(37)–C(38)–C(42)–C(43)	1.3(3)
C(26)–C(25)–C(33)–C(34)	173.50(17)	C(39)–C(38)–C(42)–C(43)	–178.91(18)
P(1)–C(25)–C(33)–C(34)	–18.0(3)	C(38)–C(42)–C(43)–C(44)	2.1(3)
C(32)–C(33)–C(34)–C(35)	–67.0(2)	C(42)–C(43)–C(44)–C(45)	–2.2(3)
C(25)–C(33)–C(34)–C(35)	114.44(19)	C(43)–C(44)–C(45)–C(37)	–1.0(3)
C(32)–C(33)–C(34)–C(36)	56.1(2)	C(43)–C(44)–C(45)–C(46)	178.35(18)
C(25)–C(33)–C(34)–C(36)	–122.44(19)	C(38)–C(37)–C(45)–C(44)	4.4(2)
C(1)–P(2)–C(37)–C(38)	–32.28(17)	P(2)–C(37)–C(45)–C(44)	–165.79(14)
P(1)–P(2)–C(37)–C(38)	83.85(15)	C(38)–C(37)–C(45)–C(46)	–174.96(16)
C(1)–P(2)–C(37)–C(45)	137.09(13)	P(2)–C(37)–C(45)–C(46)	14.9(2)
P(1)–P(2)–C(37)–C(45)	–106.78(12)	C(44)–C(45)–C(46)–C(48)	63.2(2)
C(45)–C(37)–C(38)–C(42)	–4.5(2)	C(37)–C(45)–C(46)–C(48)	–117.40(19)
P(2)–C(37)–C(38)–C(42)	164.49(14)	C(44)–C(45)–C(46)–C(47)	–60.3(2)
C(45)–C(37)–C(38)–C(39)	175.75(16)	C(37)–C(45)–C(46)–C(47)	119.02(19)

Table A7. Crystal data and structure refinement for Dipp₂P(O)Cl

Empirical formula	C ₄₈ H ₆₈ ClOP ₂	
Formula weight	758.41	
Temperature	173(2) K	
Wavelength	0.71073 Å	
Crystal system	Monoclinic	
Space group	P2(1)/c	
Unit cell dimensions	a = 10.766(3) Å	α = 90.000°
	b = 14.997(5) Å	β = 108.765(4)°
	c = 15.032(5) Å	γ = 90.000°
Volume	2298.0(12) Å ³	
Z	2	
Density (calculated)	1.096 Mg/m ³	
Absorption coefficient	0.185 mm ⁻¹	
F(000)	822	
Crystal size	0.41 x 0.13 x 0.04 mm ³	
Theta range for data collection	1.97 to 27.54°.	
Index ranges	-13<=h<=14, -19<=k<=19, -19<=l<=19	
Reflections collected	32697	
Independent reflections	5297 [R(int) = 0.1574]	
Completeness to theta = 27.54°	99.9 %	
Absorption correction	None	
Max. and min. transmission	0.9919 and 0.9274	
Refinement method	Full-matrix least-squares on F ²	
Data / restraints / parameters	5297 / 0 / 252	
Goodness-of-fit on F ²	1.018	
Final R indices [I>2sigma(I)]	R1 = 0.0723, wR2 = 0.1647	
R indices (all data)	R1 = 0.1659, wR2 = 0.2073	
Largest diff. peak and hole	0.296 and -0.648 e.Å ⁻³	

**Table A8. Atomic coordinates ($\times 10^4$) and equivalent isotropic displacement parameters ($\text{\AA}^2 \times 10^3$)
for $\text{Dipp}_2\text{P(O)Cl}$ ***

	x	y	z	U(eq)
P(1)	8749(1)	1521(1)	1606(1)	27(1)
Cl(1)	7442(1)	704(1)	637(1)	47(1)
O(1)	9414(4)	2013(3)	1095(3)	81(1)
C(1)	7866(4)	2206(2)	2204(2)	24(1)
C(2)	6559(4)	2500(3)	1775(3)	30(1)
C(3)	5843(4)	2474(3)	718(3)	37(1)
C(4)	5437(5)	3404(3)	337(3)	56(1)
C(5)	4655(4)	1855(4)	475(3)	57(1)
C(6)	5913(4)	2894(3)	2344(3)	37(1)
C(7)	6539(4)	3040(3)	3285(3)	38(1)
C(8)	7854(4)	2852(3)	3675(3)	33(1)
C(9)	8551(4)	2453(2)	3145(3)	26(1)
C(10)	10032(4)	2398(3)	3583(3)	28(1)
C(11)	10480(4)	1812(3)	4458(3)	34(1)
C(12)	10606(4)	3336(3)	3824(3)	39(1)
C(13)	9576(4)	641(2)	2427(2)	24(1)
C(14)	8873(4)	104(3)	2871(3)	29(1)
C(15)	7416(4)	186(3)	2748(3)	34(1)
C(16)	6667(5)	-646(3)	2272(4)	56(1)
C(17)	7171(5)	354(3)	3678(3)	49(1)
C(18)	9543(4)	-572(3)	3463(3)	35(1)
C(19)	10848(4)	-729(3)	3613(3)	40(1)
C(20)	11522(4)	-216(3)	3174(3)	36(1)
C(21)	10915(4)	484(3)	2575(3)	28(1)
C(22)	11749(4)	1003(3)	2103(3)	36(1)
C(23)	13062(5)	1283(5)	2788(4)	81(2)
C(24)	11919(6)	473(4)	1301(4)	62(2)

* U(eq) is defined as one third of the trace of the orthogonalized U^{ij} tensor.

Table A9. Bond lengths [Å] and angles [°] for Dipp₂P(O)Cl

P(1)–O(1)	1.413(4)	C(2)–C(1)–P(1)	123.4(3)
P(1)–C(1)	1.822(4)	C(9)–C(1)–P(1)	116.9(3)
P(1)–C(13)	1.831(4)	C(6)–C(2)–C(1)	118.0(4)
P(1)–Cl(1)	2.0700(16)	C(6)–C(2)–C(3)	117.7(3)
C(1)–C(2)	1.417(5)	C(1)–C(2)–C(3)	124.2(3)
C(1)–C(9)	1.418(5)	C(4)–C(3)–C(2)	110.9(4)
C(2)–C(6)	1.396(5)	C(4)–C(3)–C(5)	110.6(4)
C(2)–C(3)	1.526(5)	C(2)–C(3)–C(5)	111.6(4)
C(3)–C(4)	1.518(6)	C(7)–C(6)–C(2)	121.5(4)
C(3)–C(5)	1.527(6)	C(6)–C(7)–C(8)	120.1(4)
C(6)–C(7)	1.374(6)	C(7)–C(8)–C(9)	120.9(4)
C(7)–C(8)	1.376(5)	C(8)–C(9)–C(1)	118.7(3)
C(8)–C(9)	1.393(5)	C(8)–C(9)–C(10)	117.3(3)
C(9)–C(10)	1.519(5)	C(1)–C(9)–C(10)	123.7(3)
C(10)–C(11)	1.526(5)	C(9)–C(10)–C(11)	113.7(3)
C(10)–C(12)	1.532(5)	C(9)–C(10)–C(12)	109.9(3)
C(13)–C(21)	1.405(5)	C(11)–C(10)–C(12)	109.4(3)
C(13)–C(14)	1.411(5)	C(21)–C(13)–C(14)	120.5(3)
C(14)–C(18)	1.389(5)	C(21)–C(13)–P(1)	118.7(3)
C(14)–C(15)	1.524(5)	C(14)–C(13)–P(1)	120.8(3)
C(15)–C(17)	1.525(6)	C(18)–C(14)–C(13)	118.2(4)
C(15)–C(16)	1.532(6)	C(18)–C(14)–C(15)	116.0(3)
C(18)–C(19)	1.369(6)	C(13)–C(14)–C(15)	125.8(4)
C(19)–C(20)	1.366(6)	C(14)–C(15)–C(17)	112.2(3)
C(20)–C(21)	1.400(5)	C(14)–C(15)–C(16)	111.0(4)
C(21)–C(22)	1.525(5)	C(17)–C(15)–C(16)	110.1(4)
C(22)–C(24)	1.504(6)	C(19)–C(18)–C(14)	121.7(4)
C(22)–C(23)	1.516(6)	C(20)–C(19)–C(18)	120.0(4)
O(1)–P(1)–C(1)	114.2(2)	C(19)–C(20)–C(21)	121.5(4)
O(1)–P(1)–C(13)	121.4(2)	C(20)–C(21)–C(13)	118.1(4)
C(1)–P(1)–C(13)	106.96(16)	C(20)–C(21)–C(22)	117.3(4)
O(1)–P(1)–Cl(1)	105.99(19)	C(13)–C(21)–C(22)	124.6(3)
C(1)–P(1)–Cl(1)	109.69(13)	C(24)–C(22)–C(23)	111.3(4)
C(13)–P(1)–Cl(1)	96.92(13)	C(24)–C(22)–C(21)	110.2(4)
C(2)–C(1)–C(9)	119.7(3)	C(23)–C(22)–C(21)	112.6(4)

Table A10. Anisotropic displacement parameters ($\text{\AA}^2 \times 10^3$) for Dipp₂P(O)Cl *

	U ¹¹	U ²²	U ³³	U ²³	U ¹³	U ¹²
P(1)31(1)	29(1)	21(1)	21(1)	2(1)	8(1)	3(1)
Cl(1)52(1)	48(1)	34(1)	34(1)	-8(1)	3(1)	1(1)
O(1)93(3)	73(3)	85(3)	85(3)	11(2)	39(3)	1(2)
C(1)30(2)	23(2)	21(2)	21(2)	5(2)	10(2)	-2(2)
C(2)25(2)	33(2)	29(2)	29(2)	1(2)	7(2)	0(2)
C(3)30(2)	47(3)	28(2)	28(2)	-3(2)	2(2)	0(2)
C(4)58(3)	63(3)	35(3)	35(3)	8(2)	-1(2)	17(3)
C(5)41(3)	75(4)	48(3)	48(3)	-13(3)	4(2)	-12(3)
C(6)23(2)	46(3)	43(3)	43(3)	0(2)	10(2)	7(2)
C(7)39(3)	47(3)	34(2)	34(2)	-2(2)	19(2)	13(2)
C(8)39(2)	34(2)	24(2)	24(2)	-1(2)	10(2)	7(2)
C(9)31(2)	22(2)	26(2)	26(2)	6(2)	9(2)	3(2)
C(10)25(2)	31(2)	25(2)	25(2)	-1(2)	5(2)	-2(2)
C(11)36(2)	33(2)	29(2)	29(2)	4(2)	3(2)	1(2)
C(12)34(2)	35(3)	41(3)	41(3)	-3(2)	3(2)	-5(2)
C(13)32(2)	21(2)	20(2)	20(2)	-1(2)	11(2)	1(2)
C(14)36(2)	26(2)	27(2)	27(2)	-3(2)	12(2)	-6(2)
C(15)31(2)	31(2)	44(3)	44(3)	1(2)	18(2)	-7(2)
C(16)44(3)	47(3)	77(4)	77(4)	-6(3)	19(3)	-21(2)
C(17)52(3)	52(3)	53(3)	53(3)	2(2)	30(3)	0(2)
C(18)44(3)	31(2)	32(2)	32(2)	5(2)	14(2)	1(2)
C(19)49(3)	34(3)	31(2)	31(2)	7(2)	4(2)	11(2)
C(20)31(2)	39(3)	35(2)	35(2)	2(2)	7(2)	9(2)
C(21)29(2)	25(2)	27(2)	27(2)	-5(2)	5(2)	-1(2)
C(22)27(2)	39(3)	44(3)	44(3)	6(2)	14(2)	-2(2)
C(23)49(3)	128(6)	61(4)	61(4)	1(4)	10(3)	-39(4)
C(24)90(4)	56(3)	59(3)	59(3)	-7(3)	49(3)	-13(3)

* The anisotropic displacement factor exponent takes the form: $-2\pi^2 [h^2 a^{*2} U^{11} + \dots + 2 h k a^* b^* U^{12}]$

Table A11. Hydrogen coordinates (x 10⁴) and isotropic displacement parameters (Å² x 10³) for Dipp₂P(O)Cl

	x	y	z	U(eq)
H(3)	6466	2236	406	44
H(4A)	4776	3636	598	84
H(4B)	5067	3380	-349	84
H(4C)	6205	3797	517	84
H(5A)	3993	2103	725	86
H(5B)	4927	1266	752	86
H(5C)	4282	1798	-209	86
H(6)	5021	3066	2075	45
H(7)	6063	3272	3667	45
H(8)	8293	2996	4315	39
H(10)	10394	2139	3105	33
H(11A)	10164	2066	4947	52
H(11B)	11440	1784	4688	52
H(11C)	10122	1210	4302	52
H(12A)	10309	3715	3265	58
H(12B)	11566	3302	4041	58
H(12C)	10310	3591	4322	58
H(15)	7063	707	2329	41
H(16A)	6793	-730	1660	84
H(16B)	5731	-570	2183	84
H(16C)	6999	-1169	2668	84
H(17A)	7485	-156	4097	74
H(17B)	6229	435	3563	74
H(17C)	7641	893	3972	74
H(18)	9084	-936	3771	42
H(19)	11283	-1195	4024	48
H(20)	12424	-336	3277	43
H(22)	11258	1558	1833	43
H(23A)	12919	1643	3291	122
H(23B)	13542	1636	2457	122
H(23C)	13573	752	3059	122
H(24A)	12405	-75	1544	93
H(24B)	12407	828	977	93
H(24C)	11055	320	859	93

Table A12. Torsion angles [°] for Dipp₂P(O)Cl

O(1)–P(1)–C(1)–C(2)	87.5(4)	C(1)–P(1)–C(13)–C(21)	–130.7(3)
C(13)–P(1)–C(1)–C(2)	–135.3(3)	Cl(1)–P(1)–C(13)–C(21)	116.2(3)
Cl(1)–P(1)–C(1)–C(2)	–31.2(3)	O(1)–P(1)–C(13)–C(14)	–174.6(3)
O(1)–P(1)–C(1)–C(9)	–91.9(3)	C(1)–P(1)–C(13)–C(14)	52.0(3)
C(13)–P(1)–C(1)–C(9)	45.3(3)	Cl(1)–P(1)–C(13)–C(14)	–61.1(3)
Cl(1)–P(1)–C(1)–C(9)	149.3(3)	C(21)–C(13)–C(14)–C(18)	0.7(5)
C(9)–C(1)–C(2)–C(6)	–10.9(6)	P(1)–C(13)–C(14)–C(18)	177.9(3)
P(1)–C(1)–C(2)–C(6)	169.7(3)	C(21)–C(13)–C(14)–C(15)	–178.1(4)
C(9)–C(1)–C(2)–C(3)	164.5(4)	P(1)–C(13)–C(14)–C(15)	–0.9(5)
P(1)–C(1)–C(2)–C(3)	–14.9(6)	C(18)–C(14)–C(15)–C(17)	59.4(5)
C(6)–C(2)–C(3)–C(4)	55.9(5)	C(13)–C(14)–C(15)–C(17)	–121.8(4)
C(1)–C(2)–C(3)–C(4)	–119.5(4)	C(18)–C(14)–C(15)–C(16)	–64.2(5)
C(6)–C(2)–C(3)–C(5)	–67.8(5)	C(13)–C(14)–C(15)–C(16)	114.6(4)
C(1)–C(2)–C(3)–C(5)	116.7(4)	C(13)–C(14)–C(18)–C(19)	–0.5(6)
C(1)–C(2)–C(6)–C(7)	3.4(6)	C(15)–C(14)–C(18)–C(19)	178.4(4)
C(3)–C(2)–C(6)–C(7)	–172.3(4)	C(14)–C(18)–C(19)–C(20)	–0.3(6)
C(2)–C(6)–C(7)–C(8)	4.4(7)	C(18)–C(19)–C(20)–C(21)	0.9(6)
C(6)–C(7)–C(8)–C(9)	–4.7(7)	C(19)–C(20)–C(21)–C(13)	–0.8(6)
C(7)–C(8)–C(9)–C(1)	–2.9(6)	C(19)–C(20)–C(21)–C(22)	–178.7(4)
C(7)–C(8)–C(9)–C(10)	170.9(4)	C(14)–C(13)–C(21)–C(20)	0.0(5)
C(2)–C(1)–C(9)–C(8)	10.7(5)	P(1)–C(13)–C(21)–C(20)	–177.3(3)
P(1)–C(1)–C(9)–C(8)	–169.9(3)	C(14)–C(13)–C(21)–C(22)	177.7(4)
C(2)–C(1)–C(9)–C(10)	–162.7(4)	P(1)–C(13)–C(21)–C(22)	0.4(5)
P(1)–C(1)–C(9)–C(10)	16.8(5)	C(20)–C(21)–C(22)–C(24)	76.7(5)
C(8)–C(9)–C(10)–C(11)	64.4(5)	C(13)–C(21)–C(22)–C(24)	–101.1(5)
C(1)–C(9)–C(10)–C(11)	–122.1(4)	C(20)–C(21)–C(22)–C(23)	–48.3(6)
C(8)–C(9)–C(10)–C(12)	–58.6(4)	C(13)–C(21)–C(22)–C(23)	134
C(1)–C(9)–C(10)–C(12)	114.8(4)		
O(1)–P(1)–C(13)–C(21)	2.7(4)		
